Torsten Mann

Fatigue assessment methods for welded structures and their application to an aluminium T-joint

Doctoral thesis
for the degree of doktor ingeniør

Trondheim, Norway, June 2006

Norwegian University of Science and Technology
Faculty of Engineering Science and Technology
Department of Engineering Design and Materials

NTNU
Norwegian University of Science and Technology

Doctoral thesis
for the degree of doktor ingeniør

Faculty of Engineering Science and Technology
Department of Engineering Design and Materials

© Torsten Mann

ISBN 82-471-8020-0 (printed ver.)
ISBN 82-471-8019-7 (electronic ver.)
ISSN 1503-8181

Doctoral thesis at NTNU, 2006:129

To
Stefanie, Emma and Nils

Preface

Fortunately, when I started to work on this thesis, I was little aware of the problems I was facing. Thinking of the crack propagation approach as the method of choice to assess the fatigue life of welded structures, I went ahead. However, soon I started to realise that fatigue is not as simple as I hoped it to be. Many fatigue phenomena are only understood as far as empirical descriptions reach. The rather non-technical terms *fatigue* or *notch sensitivity*, as well as the parallel existence of various fatigue assessment approaches are an indication of the lack of fundamental understanding. Even the more analytically based crack propagation approach is in the same situation, since the crack propagation laws are empirical. The fact that we are still using Wöhler's S-N-curve approach may either indicate the validity of the method or the lack of deeper insight – probably both. It is accepted that there is and always will be considerable scatter in fatigue data, which does not make it easy to find general rules. However this should not prohibit further effort to increase understanding, although the gains might be overshadowed by scatter. Many efforts are made to obtain a more fundamental description of the fatigue process, such as tracing cracks from the very beginning at some micro-structural feature. However, at the moment I doubt its practical applicability to predict the life of a real structure, but it is not impossible that this may happen.

Due to the design nature of the financing project, the work was aimed at the fatigue assessment of welded joints in general, rather than at some very detailed fundamental fatigue problem. The different state-of-the-art approaches to predict the fatigue life of welded joints are described, applied and compared in this work, cf. Chapters 2, 5 and 6. When applying the different approaches, it is immediately found that they often are not applicable in a straightforward, self-explanatory manner. Usually many variants exist and the designer must choose, especially if the analysis is to be more sophisticated than applying a nominal stress S-N curve. The parallel existence of different fatigue life assessment approaches is irritating and unsatisfactory, since it makes life difficult for the engineer. In the analyses carried out and reported in this thesis, I have tried to give an idea of which method is most promising and highlight some important issues. Some of

these analyses have been presented at the *15th European Conference on Fracture* (ECF15) September 2004 in Stockholm [1] and published in *Fatigue & Fracture of Engineering Materials & Structures* [2].

Because of the investigations of the influence of residual stress on the fatigue life of welded joints, which were carried out in a related project, the aspect of mean stress dependency has received wide attention. This is discussed in a separate chapter, Chapter 3. The work described in this chapter has been submitted for publication in the *International Journal of Fatigue* [3].

Since the initial defects in the welds were below 0.1 mm in size, the propagation behaviour of short cracks found its way into this work. Crack propagation tests on sub-millimetre cracks have been carried out to investigate this behaviour. They are reported and evaluated in Chapter 4. The results have been accepted for presentation at the *International Conference on Fatigue Damage of Structural Materials VI* September 2006 in Hyannis [4].

There is, as is usual, a longer story behind this thesis. One or two years ago, I had a version that was quite different from the present one in mind. In my first year of doctoral work at *NTNU*, I was fully engaged with investigations concerning the applicability of Neuber's rule to notched specimens subjected to large scale yielding. Unfortunately, all attempts to further finance this research were in vain. Nevertheless, the effort gave birth to a journal paper*, which ironically was awarded the CEGB Prize of the *Journal of Strain Analysis* in 2003. For obvious reasons, I was tempted to somehow include those results. However, since the main work was devoted to fatigue design of welded structures, it became more and more clear that they hardly fitted in here, and eventually, but reluctantly, I decided to leave them out.

Kongsberg, June 2006
Torsten Mann

*G. Härkegård, T. Mann: Neuber prediction of elastic-plastic strain concentration in notched specimens under large-scale yielding, *J Strain Anal Eng*, Vol. 38, 2003, pp. 79-94.

Acknowledgements

The work covered by this thesis has been supported by the *Research Council of Norway* and the Norwegian light metals industry through the *NorLight* project and it was carried out at the *Department of Engineering Design and Materials*, *Norwegian University of Science and Technology (NTNU)*. Both are gratefully acknowledged.

I am much obliged to my supervisor Professor Gunnar Härkegård for his efforts to finance my research as well as Professor Einar Bardal for supporting my first year's financing through the department and Professor Hans Petter Hildre for eventually providing a scholarship.

Most of all, I am indebted to Professor Gunnar Härkegård for his suggestions, numerous fruitful discussions and his consistently elaborate replies to my questions. Our discussions seldom remained on fatigue problems, but often ended on rather philosophical topics, which I enjoyed very much.

I am grateful to my co-supervisor Bård Wathne Tveiten for always generously providing data, advice and information.

Furthermore, I thank my colleagues at *NTNU* : Hans-Jörg Huth, Anders Wormsen and Arne Fjeldstad for their discussions and for making life as a doctoral candidate less lonesome

Klaus Stärk is acknowledged for the excellent job in carrying out the short crack propagation measurements, Odd Nerdahl and the staff at our laboratory for assistance during the experimental work, Stewart Clark for helping me to improve the language and Brede Thorkildsen for freeing me from three weeks of work at *FMC Technologies* to finalize this work.

Finally, I would like to express my gratitude to my parents for raising me the way they did and for guiding and making my education possible.

Abstract

Following a short introduction, the state-of-the-art fatigue life assessment methods based on the nominal stress, the structural hot spot stress and the effective notch stress, as well as the crack propagation analysis are explained and discussed.

Thereafter, the effect of mean stress on crack propagation was investigated by exemplifying crack propagation data from different aluminium alloys. In this context, Walker's equation received wide attention. In addition, a new, simple equation to express the mean stress dependency of crack propagation data has been proposed.

In order to generate crack propagation data for the 6082-T6 aluminium alloy, investigate the behaviour of short cracks and find the mean stress dependency of crack growth in this alloy, crack propagation tests of sub-millimetre cracks subjected to different stress ratios have been carried out. The crack depth was successfully monitored on-line employing a special direct current potential drop technique. The crack propagation data generated verified the long crack propagation data given in Eurocode 9 [5]. In addition, useful experience was gained to improve future tests. Some evidence was found of accelerated crack growth near the threshold. Based on the data obtained and literature data a Walker exponent $\gamma = 0.78$ has been calculated for the aluminium alloy 6082-T6.

The fatigue life of welded aluminium T-joints has been estimated using the approaches introduced in Chapter 2. The results have been compared with experimental data from T-joints subjected to 4-point bending. In addition, a series of T-joints subjected to transverse bending has been fatigue tested and the results have been compared with predictions using the same fatigue life assessment methods.

The nominal stress gave a conservative prediction in case of the 4-point bending loading. Since no applicable detail category for the transverse bending load case exists, a suitable detail category has been suggested.

The structural hot spot stress approach resulted in conservative predictions (factor 4-10 in life) for both load cases.

The predictions from the effective notch stress approach are in excellent agreement with the experimental results, where the method using a 1 mm weld toe

radius gave the best results. It has been shown that the method can be successfully applied to joints with wall thicknesses down to 3 mm.

The fatigue life predicted with the crack propagation approaches is in excellent agreement with the experimental results from the 4-point bending load when the M_{k} factor was used. Applying the local stress distribution, the predictions are conservative for both load cases.

The slopes of all predicted S-N curves, especially from the stress based methods, are steeper than the experimental curves.

Contents

Preface **i**

Acknowledgement **iii**

Abstract **iv**

Nomenclature **xi**

1 Introduction **1**
1.1 Motivation 1
1.2 Outline 2
1.2.1 Chapter 1: Introduction 2
1.2.2 Chapter 2: Fatigue life assessment methods 2
1.2.3 Chapter 3: The influence of mean stress on fatigue crack growth 3
1.2.4 Chapter 4: Short crack growth testing 3
1.2.5 Chapter 5: A welded T-joint subjected to 4-point bending 3
1.2.6 Chapter 6: A welded T-joint subjected to transverse bending 3
1.2.7 Chapter 7: Conclusions 4
1.3 Some untreated aspects 4

2 Fatigue life assessment methods **5**
2.1 Introduction 5
2.2 Relevant features of fatigue in welds 6
2.2.1 Crack-like defects 6
2.2.2 Residual stress 6
2.2.3 The heat affected zone 7
2.3 Nominal stress 7
2.4 Structural hot spot stress 8
2.4.1 Structural hot spot stress from extrapolation 8
2.4.2 Structural hot spot stress from linearisation 11

2.4.3 Further approaches 12
2.5 Effective notch stress 13
2.5.1 Local stress 13
2.5.2 Notch sensitivity 13
2.5.3 A comparison 17
2.5.4 Radaj's effective notch stress approach 17
2.5.5 Principal or equivalent stress 18
2.6 Crack propagation analysis 19
2.6.1 Linear elastic fracture mechanics 20
2.6.2 Crack propagation behaviour 20
2.6.3 Estimating fatigue life 22
2.6.4 An engineering method to treat short cracks 24
2.6.5 A crack at a weld toe 26

3 The influence of mean stress on fatigue 33
3.1 Introduction 33
3.2 Mean stress equations – a short introduction 34
3.2.1 Fatigue crack initiation 34
3.2.2 Fatigue crack propagation 35
3.3 Walker's equation 36
3.3.1 Fatigue crack initiation 36
3.3.2 Fatigue crack propagation 37
3.3.3 The Walker exponent 38
3.4 A simple physical model of mean stress dependency 41
3.4.1 Application to 7075-T6 aluminium alloy $\mathrm{d}a/\mathrm{d}N$ data . . . 42
3.4.2 Application to 5083-H321 aluminium alloy ΔK_{th} data . . . 44
3.5 A new mean stress equation 45
3.6 Remarks 48

4 Short crack growth testing 49
4.1 Test specimens and measurement technique 50
4.1.1 The test specimens 50
4.1.2 Test conditions and potential drop technique 50
4.2 Some pre-test evaluations 52
4.2.1 Fatigue limit of notched specimen 53
4.2.2 Fatigue limit of cracked specimen 53
4.3 Correlating potential drop and crack depth 54
4.3.1 Edge crack in a semi-infinite plate 54
4.3.2 Edge crack in a finite plate 55
4.4 The stress intensity factor 55
4.5 Results 56
4.5.1 Semi-infinite plate or SENT? 57
4.5.2 Crack propagation data 57
4.5.3 Mean stress dependency 59
4.6 Remarks and discussion 60

5 A welded T-joint subjected to 4-point bending 63
5.1 Background . . . 63
5.1.1 Fatigue tests . . . 63
5.1.2 Calculating the nominal stress . . . 65
5.1.3 Residual stress . . . 66
5.1.4 Material data . . . 68
5.1.5 Micro-structure . . . 69
5.2 Nominal stress . . . 69
5.3 Structural hot spot stress . . . 70
5.3.1 Structural hot spot stress concentration factor . . . 71
5.3.2 Parametric equations . . . 72
5.4 Effective notch stress . . . 73
5.4.1 Stress analysis . . . 74
5.4.2 Estimating the fatigue life . . . 77
5.5 Crack propagation analysis . . . 81
5.5.1 The characteristic crack length a^* . . . 81
5.5.2 Finite versus infinite plate thickness . . . 83
5.5.3 Tension or bending loading . . . 84
5.5.4 Crack shape, initial and final crack depth . . . 86
5.5.5 The factors F and M_{k} . . . 86
5.5.6 Results . . . 87
5.5.7 Some sensitivity studies . . . 88
5.6 Crack propagation using the local stress distribution . . . 93
5.7 A comparison . . . 95

6 A welded T-joint subjected to transverse bending 97
6.1 Fatigue testing . . . 98
6.1.1 Description . . . 98
6.1.2 Calculating the nominal stress . . . 99
6.1.3 Test results . . . 101
6.1.4 Strain measurements . . . 102
6.2 Nominal stress . . . 105
6.3 Structural hot spot stress . . . 105
6.4 Effective notch stress . . . 107
6.4.1 The effective notch stress according to Radaj . . . 110
6.5 Crack propagation analysis . . . 111
6.6 A comparison . . . 113

7 Conclusions 115
7.1 Summary . . . 115
7.2 Discussion and further work . . . 116

Bibliography 119

Appendices 127

A Walker's equation **127**
A.1 Fatigue limit 127
A.2 Crack propagation rate 127
A.3 Linear regression to find Walker exponent 128

B Geometry functions for some crack configurations **129**
B.1 Edge crack in a finite plate 129
B.2 Semi-elliptical surface crack in a finite plate 129
B.3 Semi-elliptical surface crack at a weld toe in a finite plate 130
B.4 Crack propagation with variable a/c ratio 133

C Second moment of area of the cross section of the T-joint **135**

D Welding Procedure Specification **137**

Nomenclature

A = constant in Basquin's law

a = crack depth

a^* = characteristic crack depth

a_f = final crack depth

a_i = initial crack depth

b = constant in Basquin's law

C = constant in Paris' law

$2c$ = crack length of a semi-elliptical surface crack (measured along the surface of the component)

F = geometry factor used to determine the stress intensity factor

f = factor used in different codes (e.g. [5, 6]) to account for the mean stress effect

K = stress intensity factor

ΔK = stress intensity factor range

ΔK^* = stress intensity factor range at $R = 0$, see Section 3.5

ΔK_Walker = effective stress intensity factor range proposed by Walker

ΔK_eff = effective stress intensity factor range, $\Delta K_\mathrm{eff} = K_\mathrm{max} - K_\mathrm{op}$

ΔK_th = threshold stress intensity factor range

K_Ic = fracture toughness

K_f = fatigue notch factor

K_hs = hot spot stress concentration factor, $K_\mathrm{hs} = \sigma_\mathrm{hs}/S$

K_op = stress intensity factor at which a crack becomes fully open

K_t = elastically calculated stress concentration factor

M = bending moment

M_k = factor to include the stress concentration at a weld toe when calculating the stress intensity factor

m = exponent in Paris' law
N_f = fatigue life
N_p = life spent whilst a crack is growing from a_i to a_f
n_χ = support coefficient
P = force
q = notch sensitivity
R = stress ratio, $R = \sigma_\mathrm{min}/\sigma_\mathrm{max}$
R_eff = effective stress ratio
R_m = ultimate tensile strength
R_nom = nominal stress ratio
$R_\mathrm{p0.2}$ = yield strength
S = nominal stress
t = plate thickness
W = crack coordinate running from the crack tip to the specimen surface, cf. Fig. 2.13
w, $2w$ = plate width
y = coordinate perpendicular to the beam axis (here chord or brace)
z = coordinate along the beam axis (here chord or brace)
α = relative crack depth, $\alpha = a/t$
β = relative coordinate starting at the crack tip, $\beta = x/t$
γ = Walker exponent
γ_A = Walker exponent for the fatigue limit
γ_th = Walker exponent for the threshold stress intensity factor range
η = relative crack coordinate, $\eta = W/a$, cf. Fig. 2.13
ρ = notch radius
ρ^* = micro-structural support length
ρ^0 = slip layer thickness
ρ_f = fictitious weld toe radius
ρ_o = characteristic length
$\Delta\sigma$ = stress range, $\Delta\sigma = \sigma_\mathrm{max} - \sigma_\mathrm{min}$
$\Delta\sigma_\mathrm{A}$ = fatigue limit (stress range)
$\Delta\sigma_\mathrm{C,hs}$ = fatigue strength at 2×10^6 cycles expressed in terms of hot spot stress
$\Delta\sigma_\mathrm{C}$ = fatigue strength at 2×10^6 cycles expressed in terms of nominal stress
$\Delta\sigma_\mathrm{SWT}$ = Smith, Watson and Topper effective stress range
$\Delta\sigma_\mathrm{Walker}$ = effective stress by Walker
$\Delta\sigma_\mathrm{W}$ = fatigue limit at $R = -1$ (stress range)
σ = stress, local stress
σ_A = fatigue limit (stress amplitude)

σ_{W} = fatigue limit at $R = -1$ (stress amplitude)

σ_{a} = stress amplitude

σ_{f} = fatigue effective notch stress

σ'_{f} = constant in Basquin's law

σ_{hs} = structural stress amplitude at the weld toe (hot spot stress)

σ_{max} = maximum stress

σ_{min} = minimum stress

σ_{m} = mean stress, $\sigma_{\mathrm{m}} = \frac{1}{2}\left(\sigma_{\mathrm{max}} + \sigma_{\mathrm{min}}\right)$

χ = absolute value of the relative stress gradient, $\chi = \frac{|\mathrm{d}\sigma/\mathrm{d}x|}{|\sigma_{\mathrm{max}}|}$

CHAPTER 1

Introduction

1.1 Motivation

Many frame-like structures are welded, which, from a fatigue point of view is far from optimal. Nevertheless, due to cost effectiveness and extensive welding experience in many companies [7, 8], welding is often the joining method of choice. This has been the case since the time when welding replaced riveting in most structures. Actually, in the aircraft industry, an industry with products very prone to fatigue problems, riveting is still the joining method that is very frequently used, which is not least due to the weak fatigue resistance of welds.

In recent times, hard competition has forced products to be produced more effectively, saving time, costs, material and weight [7–9]. In the automotive industry saving structural weight is crucial to keep the overall weight as low as possible to reduce fuel consumption, tyre wear, noise and to obtain a more active driving characteristic, hence better competitiveness. All these gains must be achieved without degrading the functionality or the service life of a product.

To make a component lighter inevitably increases the stresses in the component when subjected to the same load. If fatigue was not a critical failure mode in a component in the first place, slimming it may cause fatigue to become a problem. Re-design to relieve the welds from high stresses or increasing the fatigue resistance of welds, e.g., through grinding or the introduction of favourable residual stresses (peening, overload), may solve the problem [10]. Another solution may be to reduce the traditionally high fatigue safety factors. However, this can be done only if the analytical tools available are precise enough. The enormous increase in computing power and the quality of today's finite element programs facilitate very detailed stress analyses. The actual fatigue life prediction, however, is not straightforward. Several approaches exist side by side, and there is no general answer about which one should be used. Of course, having a more or less well defined crack-like defect, the crack propagation approach is the obvious

choice. In a complex machined or forged component, the effective notch stress approach will certainly be used successfully. The situation becomes worse, when a welded component is to be assessed, since the local geometry underlies some scatter and the size of defects is often unknown.

It is frequently stated that the fatigue life of a welded structure is almost exclusively covered by crack propagation due to the presence of welding defects.

If this is true, the fatigue life of a welded component must be most accurately predicted using crack propagation analysis.

Codes and standards, however, primarily recommend the use of the nominal stress, the structural hot spot stress or the effective notch stress approaches. Crack propagation analysis is usually allowed as well, but it is much less used. However, the crack propagation method is not the preferred and dominating method even though crack propagation is the governing phenomenon. Why is this so? Is it because it is too complicated or because it yields too conservative results? Are too many problems still encountered when applying the method to a real structure? Is it the uncertainty about the initial crack size, shape and location or the difficulties invoking the real stress distribution over the crack? Why are the empirical, S-N curve based methods more often used than the crack propagation approach, which actually tries to model the physics behind the fatigue process?

To date basically four deterministic fatigue life prediction methods exist side by side, the nominal stress, the structural hot spot stress, the effective notch stress and the crack propagation approaches. The latter three are found in many different variants, which makes the situation even more complicated. Do these approaches yield similar results when applied to the same problem? What are the benefits and what are the drawbacks that support the existence of the various approaches?

The main scope of this work is to find answers to the above questions, as far as it is possible answer them. To reach this goal, the different fatigue life assessment approaches have been applied to a single geometric detail, a welded T-joint, and compared with experimental results.

Two problems encountered when predicting the fatigue life of the T-joint, the mean stress dependency and the propagation of short cracks have received considerable attention and are thus represented in separate chapters.

1.2 Outline

1.2.1 Chapter 1: Introduction

Chapter 1 gives an introduction to this thesis, presents a short outline and mentions the aspects of fatigue life prediction left untreated in this work.

1.2.2 Chapter 2: Fatigue life assessment methods

This chapter describes the nominal stress, structural hot spot stress and the effective notch stress approach as well as the crack propagation approach.

1.2.3 Chapter 3: The influence of mean stress on fatigue crack growth

The dependence of fatigue, especially fatigue crack propagation on mean stress is addressed in this chapter. Although due to the high residual stresses the dependence of welded structures on the mean stress due to the applied loading is usually limited, the mean stress dependency becomes an issue when the residual stress level is manipulated to improve the fatigue performance of a weld. Since part of this thesis evaluates experimental fatigue data from specimens with manipulated residual stress level, the mean stress dependency has received more attention.

A few common mean stress equations are discussed and a comparison is made based on a large amount of crack propagation data from the literature. Walker's equation receives most attention and a modified least mean squares method is presented to fit crack propagation data to Walker's equation.

Finally, a new, empirical mean stress equation is proposed.

1.2.4 Chapter 4: Short crack growth testing

In general little crack propagation data are available for the aluminium alloy 6082-T6 and in addition these data have been generated using specimens with a long (deep) crack. The cracks propagating at the weld in the T-joint analysed in this thesis, however, are initially very short.

Chapter 4 describes the experiments performed to measure the growth of sub-millimetre cracks in aluminium specimens. The obtained data are compared to long crack data from the literature and the mean stress dependency is evaluated.

1.2.5 Chapter 5: A welded T-joint subjected to 4-point bending

In this chapter the fatigue life assessment approaches described in Chapter 2 are applied to a welded T-joint subjected to 4-point bending. The predictions are compared with experimental data from the literature for the "as welded" condition and for welds with artificially introduced compressive residual stresses. Calculating the stress ratio at the weld, the residual (mean) stress effect has been accounted for in the crack propagation analysis. The different predictions are compared with each other and with the experimental data.

1.2.6 Chapter 6: A welded T-joint subjected to transverse bending

Chapter 6 describes fatigue tests carried out with T-joints identical to those analysed in Chapter 5, but this time subjected to transverse bending, which makes the weld load carrying.

After the description of the experiments and the experimental results, Chapter 5 continues the comparison of the different fatigue life assessment approaches by applying them to the T-joint subjected to the transverse bending load case.

1.2.7 Chapter 7: Conclusions

This final chapter summarises the work described in the thesis and discusses the results. Some recommendations for future work are also given.

1.3 Some untreated aspects

A few aspects that influence the fatigue life of a component have been left untreated to keep the extent of this thesis within reasonable confines.

First, only constant amplitude loading has been considered. Variable amplitude loading is usually treated with the Palmgren-Miner rule, see for example [11]. Fatigue crack propagation under variable amplitude loading is carried out incrementally [12], i.e., the crack is extended after each load cycle, see the end of Section 2.6.3, and approaches to treat crack retardation effects are discussed for example in [13].

Second, no attention has been paid to the influence of the surface quality on the fatigue life. Due to the discontinuities at the weld and the large amount of crack propagation, the impact of the surface condition is certainly of secondary importance.

The effect of the heat affected zone has not been treated explicitly. Using nominal or structural stress, the heat affected zone (HAZ) is implicitly accounted for. Knowing the material properties, i.e., crack propagation data, the effect of the HAZ is included in a crack propagation analysis as well.

Finally, only high cycle fatigue has been considered, i.e., no large plastic deformation is allowed.

CHAPTER 2

Fatigue life assessment methods

In this chapter the most common methods to predict the fatigue life of a welded component are introduced and described. This description covers the approaches based on nominal stress, structural hot spot stress and effective notch stress as well as the crack propagation analysis.

2.1 Introduction

The most widespread fatigue assessment method is to compare design stresses with allowable stresses by means of stress-life curves (often called S-N or Wöhler curves). These curves may either be based on nominal, structural or notch stress, which will be discussed in more detail in the sections below.

If no S-N-curve for a given component or material is available, the curves provided by design codes and standards must be used. They are generally based on nominal stress, but the use of structural or notch stress is given as an option in some of them. BS 8118 [14], as well as the ECCS recommendations [15], use nominal stress only. According to Macdonald and Haagensen [16], the S-N curve for two sided butt welds may serve as an S-N curve for structural hot spot stress fatigue design. Eurocode 9 [5], which still is in a pre-standard state and widely based on BS 8118, and the IIW recommendations [6] also include structural and notch stress. In the low-cycle regime, strain-life curves may take the place of the S-N curves to account for large plastic deformations.

For metals, fatigue test data usually follow straight "lines" in a $\log S$-$\log N$ plot and those lines or S-N curves can be described with Basquin's law, which may be written as

$$\sigma_{\mathrm{a}} = \sigma'_{\mathrm{f}} \left(2N_{\mathrm{f}}\right)^{b} \ , \tag{2.1}$$

where σ'_{f} and b are constants that depend on, for example, material, surface

condition, environment and stress state. Expressing Basquin's law as

$$N_{\mathrm{f}} = A\Delta\sigma^{1/b}\,, \tag{2.2}$$

where $A = \sigma_{\mathrm{f}}'^{(-1/b)}/2^{(1+1/b)}$, is also quite common and more convenient when design standards are used, e.g., Eurocode 9 [5].

In cases where the fatigue life is covered by crack propagation, $-1/b$ is equal to the exponent m in Paris' law, see Eq. 2.23.

2.2 Relevant features of fatigue in welds

2.2.1 Crack-like defects

An inherent feature of welded joints are crack-like defects such as lack of fusion and undercuts. Therefore, assuming the fatigue life to be governed by the growth of one or more of these defects [17], the crack propagation approach based on linear elastic fracture mechanics should be suitable to estimate the fatigue life. However, size, form and position of these defects are often unknown. In addition, the defects are often so small (crack depth < 1 mm) that they may require special care when their propagation behaviour is analysed. Short cracks grow faster than long cracks, which is usually explained by less crack closure [18], i.e., short cracks open at lower stresses than long cracks. Moreover, short cracks may grow even if they are below the long crack propagation threshold.

2.2.2 Residual stress

Unless stress relieved, welded details contain considerable residual stresses. These result from the contraction of the weld material when cooling down. Residual stresses are created in all directions with a self-equilibrating stress field, i.e., there are both positive and negative residual stresses, which exhibit a rather complicated distribution. This distribution is influenced by the local geometry, global constraints and the welding sequence. Residual stresses may reach yield stress magnitude. They act as an additional mean stress, i.e., the applied stress range will not be changed, but the actual stress ratio at the weld will differ from the nominal (applied) stress ratio. The straightforward approach to take care of the residual stresses is to add the residual stress at the weld where crack propagation is expected to the applied mean stress and calculate a new (local) stress ratio. This new stress ratio must then be used when estimating the fatigue life.

For all practical circumstances, this is not simple, since finding a realistic residual stress value is extremely difficult. A rough method to estimate the residual stress level is based on prevented contraction of the weld whilst cooling down, see for example Berkovits et al. [19]. Measurement is possible but difficult. A third and probably the most accurate method would be to use an FE analysis tool, e.g., WELDSIM [20–22], to calculate residual stresses. Such analyses, however, require a profound metallurgic knowledge and much computing power.

Incorporating residual stress

In general, when assessing welded structures, no attention is paid to the stress ratio. It is assumed that high tensile residual stresses (yield stress magnitude) at the weld elevate the mean stress locally to such an extent that the effect of the applied R ratio is negligible. Therefore, welded structures are usually said to be relatively insensitive to the stress ratio [23].

However, when the fatigue properties of a welded joint are improved by introducing compressive residual stresses at the critical spots along the weld, it is of course desirable to actively use the positive effect in design.

The possibility to improve the fatigue resistance of joints such as by introducing compressive residual stresses, is mentioned in the codes. But to account for their beneficial effect is usually not allowed without experimental verification. BS 8118 [14] has no means to include the effect of compressive residual stresses. Eurocode 9 [5] and the recommendations from ECCS [15] and IIW [6] introduce a fatigue enhancement factor $f(R)$ as a function of the applied stress ratio. The factor applies to the fatigue strength at $N = 2 \times 10^6$ cycles, whereas the fatigue strength at $N = 1 \times 10^4$ cycles is not enhanced (in IIW the latter is not stated), hence the S-N curve (log-log plot) is "rotated" about the point at $N = 1 \times 10^4$ cycles. In Eurocode 9 the data given are labelled "informative" only. If one intends to actively use calculated or measured residual stresses, care must be taken, since local plastic deformation due to a compressive overload will generate tensile residual stresses, i.e., existing compressive residual stresses can be partly wiped out.

2.2.3 The heat affected zone

Due to the heat input into the base material during the welding process, there is a change in the micro-structure of the base material in a zone near the weld, the so called heat affected zone (HAZ). This change may affect the material properties and especially heat treated materials may experience a reduction in strength. Pinho da Cruz et al. [24] investigated the impact of the HAZ in single lap joints made from 6082-T6 aluminium alloy. They reported increased fatigue lives in the joints that were T6 heat treated after welding, i.e., the joints with removed HAZ had the greatest fatigue strength.

2.3 Nominal stress

In the nominal stress approach, all information concerning the local stress distribution at the expected failure site is included in the S-N curve. Thus, a nominal stress S-N curve is always connected to a certain geometry and load configuration. Therefore, using nominal stress, a detail category (detail class, fatigue resistance class) in the standard used, must be similar to the joint to be analysed. This detail category possesses an S-N curve from which the endurable life or the allowable stress is found. The detail categories are usually defined through the fatigue strength at $N = 2 \times 10^6$ cycles. Structural stress concentrations (e.g. arising from an attachment) and local stress concentrations due to the weld toe notch

are already included in the S-N curves. Nominal stress is only applicable if the joint to be assessed is geometrically simple, so that it is possible to define a nominal stress and find a reasonable detail category. The stress may be found from the basic principles of strength of materials (e.g. beam theory), an FE analysis or strain measurements away from the weld. In the presence of gross geometrical stress concentration (e.g. due to shear lag or cut outs), nominal stress must be multiplied by an elastically calculated stress concentration factor to account for those stress concentrations, if they are not included in the S-N curves.

2.4 Structural hot spot stress

The structural stress approach has been developed to enable the treatment of cases, where nominal stress cannot be defined meaningfully and reduce the number of S-N curves. It is suited to treat fatigue failure starting from weld toes but does not cover weld root failure. The terminology regarding this method is not fully settled and the terms hot spot stress, geometrical stress, structural stress and combinations thereof can be found in the literature. In NORSOK N-004 [25] a nominal stress amplified by a stress concentration due to, for example, a cut out is termed hot spot stress, which does not correspond to the usual definition. The same stress is called modified nominal stress in Eurocode 9 [5]. IIW denotes the structural stress at the "hot spot", e.g., at the weld toe, the structural hot spot stress, a convention that is followed in this work.

The structural stress is the actual stress in a structure, excluding the stress peak caused by the weld toe notch, see Fig. 2.1. It is a combination of membrane and bending stresses, i.e., it obeys a linear through-thickness distribution. Since the structural hot spot stress is a fictitious value, it must be found either by means of specially adapted parametric equations, by extrapolating structural stresses outside the reach of the weld toe notch or by through-thickness linearisation. Since the structural hot spot stress includes the stress concentrations due to joint geometry, the number of detail categories can be drastically reduced. In fact, Eurocode 9 [5] only takes the thickness of the stressed member into account, whereas IIW [6] gives a reduced number of detail categories.

2.4.1 Structural hot spot stress from extrapolation

Strain measurements

The original method of finding the structural hot spot stress is to measure strains at certain points ahead of the weld. From the measured strains the stress perpendicular to the weld toe at these points is calculated and the structural hot spot stress is found from extrapolating the stress back to the weld toe, cf. Fig. 2.1. The strains should be measured perpendicular and parallel to the weld [6, 17], since both contribute to the stress perpendicular to the weld toe. The placement of the strain gauges depends on the extrapolation method, the type of "hot spot" and even on the design code or standard used. Doerk et al. [26] distinguished between three different types of "hot spots", whereas in the IIW documents [27] and [6] the types are reduced to two. Type "a", which is a weld toe on a plate

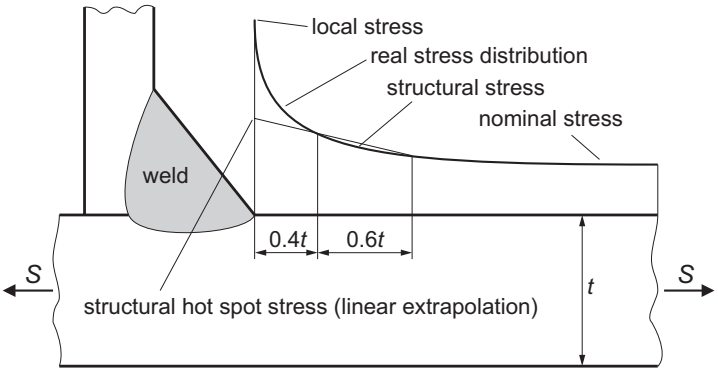

Figure 2.1: Idealised stress distribution in a welded joint and an illustration of the linear extrapolation method to calculate the structural hot spot stress.

surface, i.e., the extrapolation points can be related to the plate thickness, and type "b", which refers to a weld toe at a plate edge, i.e., the structural hot spot stress is unaffected by the plate thickness.

To find the structural hot spot stress at type "a" "hot spots", the centre of the strain gauges must be placed either $0.4t$ and $1.0t$, see Fig. 2.1, or $0.4t$, $0.9t$ and $1.4t$ away from the weld toe for linear and quadratic extrapolation, respectively. Quadratic extrapolation is recommended for details with steep stress gradients. The DNV document [28] recommends placing the extrapolation points $0.5t$ and $1.5t$ ahead of the weld toe or to use the stress value at $0.5t$ multiplied by 1.12. Extrapolation points at $0.5t$ and $1.5t$ are also specified in NORSOK N-004 [25].

For type "b" "hot spots", quadratic extrapolation with strains measured at fixed distances 4, 8 and 12 mm away from the weld toe is recommended [6, 27].

It is obvious that the physical length of the strain gauges limit the determination of the structural hot spot stress from strain measurements to rather large plate thicknesses.

Finite element analysis

Instead of finding the structural hot spot stress based on strain measurements, the stress results from a finite element analysis are often used today. The extrapolation points correspond to the positioning of the centre of the strain gauges described above. Only coarse meshes with higher order elements where a single element spans over the whole thickness in case of type "a" "hot spots" or elements being as long as 10 mm at the weld toe for a type "b" "hot spot" receive different extrapolation points. In these cases linear extrapolation from $0.5t$ and $1.5t$ (type "a") and 5 and 15 mm (type "b") is recommended [6]. Due to the fixed extrapolation points, type "b" "hot spots" are especially sensitive to the extrapolation method [29].

Tveiten [30] and Tveiten and Moan [31] suggest a new surface extrapolation method to calculate the structural hot spot stress based on the asymptotic behaviour of stress adjacent to an idealized notch. Plotting the stress distribution ahead of the weld toe obtained from a finite element analysis with a very fine

mesh, the region affected by the weld toe singularity shows a linear distribution plotting the distance from the weld toe vs stress in log-log scale. Extrapolating this linear distribution to the nominal stress the point that defines the separation between the region influenced by the weld toe and the region influenced by the structural stress is found. The region influenced by the structural stress ends where the structural stress and the nominal stress coincide. To calculate the structural hot spot stress, the stress in the region influenced by the structural stress is fitted by a second order polynomial and extrapolated to the weld toe. The applicability of this method is limited because of the very fine element mesh required.

Problems

Finding the structural hot spot stress from extrapolation involves several difficulties. Linear and quadratic extrapolation yield different structural hot spot stresses, and both the finite element mesh density and the element type will affect the result [32]. The mesh sensitivity has received considerable attention, cf. [26, 33–37], since the aim is to obtain reliable results with the usually rather coarse mesh in global finite element models. Specifications for the minimum required mesh density are given in [6] and [17] for example.

The choice of the element type has an impact on how exact the weld and its stiffness is modelled. Using solid elements the weld can be included in the model directly. Often, however, the structure adjacent to the weld is idealised by means of shell elements. Such elements model the mid-plane of a shell only and have no natural means of taking the weld geometry into account. Inclined or thickened shell elements or a combination of shell and solid elements may be used to represent the weld. Tveiten [32], for example, analysing the T-joint treated in this thesis, suggests using 20 node elements with 2 point reduced integration. The main advantage of using volume elements lies in the fact that they provide a natural means of representing the weld itself and hence its stiffness. This advantage, however, requires a great increase in meshing effort and increased computing time and in general prohibits the direct use of a global finite element model.

In membrane loading a crack will be subjected to a constant stress field, whereas a bending loading establishes a decreasing stress field. The surface stress extrapolation method, however, gives no information on the degree of membrane and bending stresses in the structure. Structural hot spot stress extrapolation procedures that are based on surface stress extrapolation do not include the stress field across the plate thickness, which will also influence the crack growth. Different details showing the same extrapolated structural stress value may show different stress fields in the plate thickness and, thus, also different crack growth lives are predicted. Due to this, a uniquely determined design S-N curve based on a structural hot spot stress derived from extrapolated surface stresses might be questioned. However, the discrepancy from a single design S-N curve for different details will likely be dependent on the failure criterion used (amount of crack growth into different stress fields for different details).

Finally, the extrapolation of surface stresses is not especially suited to be

used together with the finite element method, since the elements must be placed and sized so that the stresses are available at the extrapolation points to avoid additional interpolation.

2.4.2 Structural hot spot stress from linearisation

In the light of the difficulties mentioned above, alternative, more robust methods to calculate the structural hot spot stress are desired. If the structural hot spot stress is to be found from a finite element analysis, employing the linear through-thickness distribution of the structural stress seems to be a straightforward solution. If $\sigma(y)$ denotes the through-thickness stress distribution at the weld toe, cf. Fig. 2.2, equilibrium of forces in the x-direction yields

$$\sigma_{\mathrm{m}} = \frac{1}{t}\int_0^t \sigma_{\mathrm{x}}(y)\,\mathrm{d}y\,. \tag{2.3}$$

Equilibrium of moments with respect to $x = y = 0$ gives

$$\sigma_{\mathrm{m}}\frac{t^2}{2} + \sigma_{\mathrm{b}}\frac{t^2}{6} = \int_0^t \sigma_{\mathrm{x}}(y)y\,\mathrm{d}y\,. \tag{2.4}$$

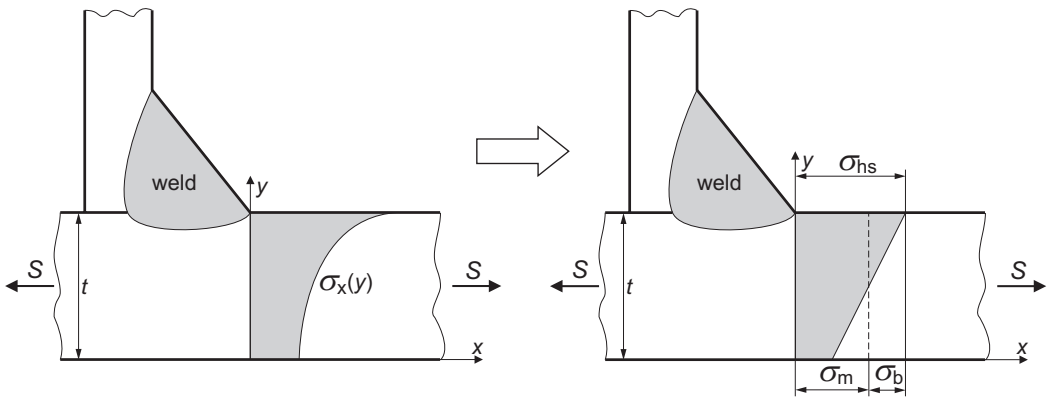

Figure 2.2: Determination to the structural hot spot stress from through-thickness linearisation.

From Eqs. 2.3 and 2.4 the membrane and bending stress components, σ_{m} and σ_{b}, respectively, are found. Adding both components the structural hot spot stress, σ_{hs}, is obtained:

$$\sigma_{\mathrm{hs}} = \sigma_{\mathrm{m}} + \sigma_{\mathrm{b}}\,. \tag{2.5}$$

Extracting both the membrane and the bending component makes it possible to account for their different impact on fatigue life, something that is not possible when extrapolating surface stresses to find the structural hot spot stress.

In case of a non-monotonic through-thickness stress distribution, e.g., in a symmetric joint, or for type "b" "hot spots" slightly modified linearisation strategies are required, see next section.

Battelle's method

When proposing his method to calculate the structural hot spot stress, Dong [33] addressed all the problems stated above. The method suggested is based on through-thickness stress linearisation. Contrary to the procedure described in the previous section, the linearisation is not carried out at the weld toe, but a distance δ away in the x-direction. This introduces the shear stress τ_{xy} into the equilibrium of moments, hence Eq. 2.4 becomes

$$\sigma_{\mathrm{m}}\frac{t^2}{2} + \sigma_{\mathrm{b}}\frac{t^2}{6} = \int_0^t \sigma_{\mathrm{x}}(y)y\,\mathrm{d}y + \delta\int_0^t \tau_{\mathrm{xy}}(y)\,\mathrm{d}y\,. \tag{2.6}$$

The distance δ may be an element length, however, no actual value is recommended as Poutiainen et al. [34] note. Evaluating the equilibrium at a distance away from the weld toe avoids the singularity at the weld toe. Based on finite element analyses of a longitudinal gusset on a plate Poutiainen et al. [34] point out that all shear stresses (τ_{xy}, τ_{zy} and τ_{zx}) must be included in the equilibrium equations if 3D models are used. Accounting for all shear stress components and choosing $\delta \leq t$, they obtain consistent results.

Type "b" "hot spots" are treated by linearising over a certain depth that corresponds to some critical crack depth. The governing equations are similar to Eqs. 2.3 and 2.6 and are found in [33].

Joints with a non-monotonic through-thickness stress distribution, e.g., symmetrical joints, are treated in a similar manner. The stress distribution is divided where τ_{xy} changes direction and then linearised from this point to the upper and lower surface.

Apart from symmetrical joints, where shell elements can not be used, both shell and solid elements are applicable.

From numerous publications, mesh sensitivity appears to be the most discussed feature of Battelle's method. Dong and co-workers [33,36,37] always claim mesh insensitivity for their method. In a large comparison of different methods to calculate the structural hot spot stress applied to different "hot spots" and loading, Healy [38] concluded that although it is not fully mesh insensitive, Battelle's method is in most cases superior to surface extrapolation. In a work by Doerk et al. [26], mesh sensitivity was found for 2D models, whereas the results from 3D models were more scattered, which is believed to be due to omitted shear stresses in the equilibrium equations in the 3D case. Poutiainen et al. [34] proved the mesh insensitivity when all shear stresses are accounted for in the 3D case.

2.4.3 Further approaches

Based on through-thickness linearisation, Poutiainen et al. [39, 40] proposed a structural hot spot stress calculation method that accounts for the relative weld size. Similar to Battelle's method for type "b" "hot spots" and symmetrical joints, the non-linear through-thickness stress distribution is transformed into a bilinear distribution using force and moment equilibrium. The two linear distributions intersect at a depth below the weld toe equal to the weld leg length. With the latter feature it is accounted for the relative weld size, i.e., the relative load fraction carried by the weld.

2.5 Effective notch stress

The nominal and structural stress approaches the effect of all or some of the stress concentrations found in a structure are included in the S-N curves. The next logical step is therefore to use the local stress at the expected failure site together with some sort of "material S-N curve". The major benefit is that whatever the geometric detail looks like, the S-N curve is the same. The effective notch stress approach described in this section is primarily applied to components, not to welds. However, the effective notch stress approach according to Radaj, cf. Section 2.5.4, which is a special variant of the general effective notch stress approach, has been proposed for welded structures. It is therefore tempting to try to apply the general to welded structures too.

2.5.1 Local stress

The local stress, σ, may be related to the nominal stress, S, through the linear relationship

$$\sigma = K_{\mathrm{t}} S \,, \tag{2.7}$$

where K_{t} is the elastically calculated stress concentration factor. Stress concentration factors for a large number of geometric details can be found in *Peterson's stress concentration factors* [41]. If K_{t} cannot be be obtained from handbooks, an experimental investigation or an FE analysis must be carried out. There are, however, some serious limitations. It might be difficult or even impossible to exactly measure the local stress peak. Employing an FE analysis, a detailed sub-model is certainly required, since global models of larger structures seldom contain all the details determining the local stress, e.g., radii and notches. Another problem arises in welded structures. The local weld geometry (angle and radii) may vary considerably along a weld seam and from weld to weld [18], hence modelling is rather difficult, especially assuming a reasonable weld toe radius.

2.5.2 Notch sensitivity

Although it seems logical to relate allowable local and nominal fatigue stresses, e.g., fatigue limit, via K_{t}, this is not generally correct and often gives too conservative results. Fatigue properties are less sensitive to stress concentration than the peak stress would suggest. Dowling [12] gives some reasons for this observation, where the two major explanations are stated below.

- Cracks that initiate at the surface will grow more slowly, if they propagate into a region with decreasing stress than in the constant stress field of a smooth fatigue specimen.
- From a statistical point of view, it is far less likely to find some sort of crack initiation feature, e.g., unfavourable grain orientation or microscopic defect, in the confined area at the notch tip than at the whole surface of a smooth fatigue specimen.

To account for the shortcomings of the stress concentration factor in fatigue design, the fatigue notch factor, K_f, relating the fatigue-effective notch stress, σ_f, to the nominal stress amplitude through

$$\sigma_\mathrm{f} = K_\mathrm{f} S \,, \tag{2.8}$$

was introduced. The fatigue notch factor is then defined as $K_\mathrm{f} = \sigma_\mathrm{A}/\sigma_\mathrm{A,notch}$, where σ_A and $\sigma_\mathrm{A,notch}$ are the fatigue limit of a smooth and a notched specimen, respectively.

A number of empirical approaches to calculate K_f have been suggested, see for example [11, 12, 42] and the most widespread are included here. It is important to note that, since all or some of the effects causing $K_\mathrm{f} \neq K_\mathrm{t}$ act simultaneously, and the real nature of the problem is not fully understood, all equations proposed to incorporate the fatigue notch effect must be regarded as estimates.

According to Thum and Buchmann [43], the relation between the fatigue notch factor and the stress concentration factor can be expressed as

$$K_\mathrm{f} = 1 + q(K_\mathrm{t} - 1) \,. \tag{2.9}$$

The parameter q is called the notch sensitivity. For $q = 1$ the maximal notch effect is obtained, hence $K_\mathrm{f} = K_\mathrm{t}$. In case of $q = 0$, $K_\mathrm{f} = 1$, which means that the notch has no effect on the fatigue properties. Two equations to estimate q will be discussed below.

Peterson's and Neuber's equations

Peterson [42] suggested estimating the notch sensitivity from

$$q = \frac{1}{1 + \rho_0/\rho} \,, \tag{2.10}$$

where ρ is the notch radius and ρ_0 a material constant with dimension length. The smaller ρ becomes, hence the more confined the highly stressed area ahead of the notch tip is, the closer to zero q becomes. A large ρ yields q close to unity, which gives $K_\mathrm{f} = K_\mathrm{t}$. Figure 2.3 demonstrates this behaviour plotting K_f and K_t as a function of the relative notch radius ρ/ρ_0. The stress concentration factor was calculated for a round bar with a circumferential semi-circular notch subjected to a tensile load. The equation to calculate K_t given in [44] was used, where the net-section radius, r, was set to 10 mm. For aluminium alloys $\rho_0 = 0.64$ mm, which represents an average value, is given in [42] and used in Fig. 2.3. Usually ρ_0 varies with the tensile strength of the material. Therefore, empirical equations to estimate ρ_0 are often based on R_m. It is certainly due to the lack of data that an average ρ_0 for aluminium is given. From Fig. 2.3 it is seen that the smaller the notch radius, and therefore the higher the stress concentration factor, the larger is the effect of q on K_f.

Neuber [45, 46] suggested using the stress averaged over the so-called micro-structural support length, ρ^*, to avoid unrealistically high theoretical stress concentration factors for sharp notches. Applying this concept to the fatigue in

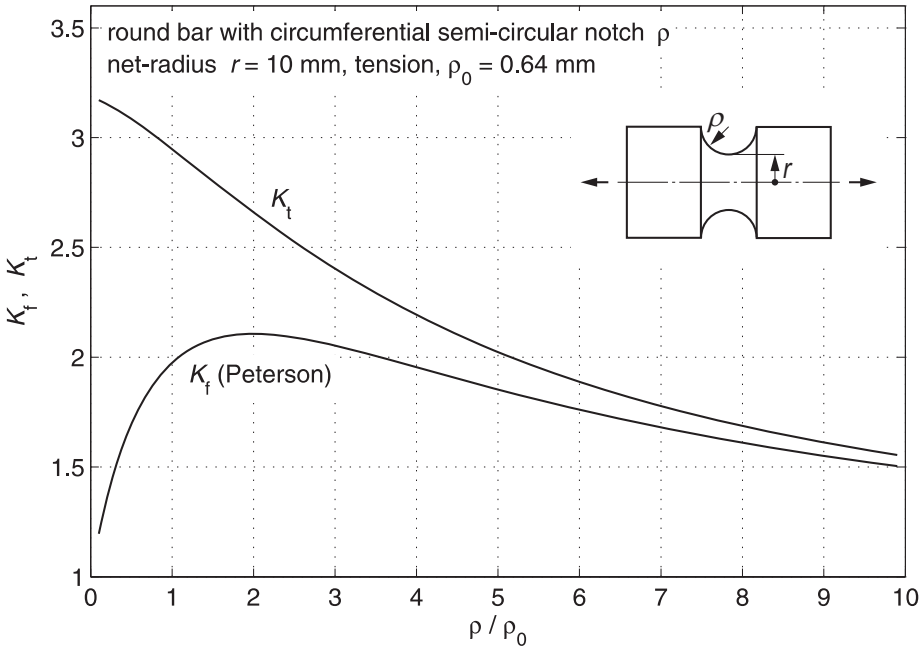

Figure 2.3: K_f and K_t as a function of the relative notch radius ρ/ρ_0 using Eqs. 2.9 and 2.10 and the K_t-equation given in [44].

notched components, see Fig. 2.4, the fatigue-effective notch stress and the micro-structural support length are related through

$$\sigma_\mathrm{f} = K_\mathrm{f} S = \frac{1}{\rho^*} \int_{x=0}^{x=\rho^*} \sigma(x) \mathrm{d}x \,. \tag{2.11}$$

Also, incorporating the micro-structural support length to estimate the notch sensitivity, Neuber proposed

$$q = \frac{1}{1 + \sqrt{2\rho^*/\rho}} \,. \tag{2.12}$$

Furthermore, Neuber suggested that the fatigue notch factor may be found directly using the fictitious notch radius

$$\rho_\mathrm{f} = \rho + s\rho^* \,, \tag{2.13}$$

where the support factor s accounts for the assumed strength hypothesis and the type of loading. Typical values for s lie between 1 and 3 and can be found for example in [11, 18, 46].

Stress gradient methods

There is an obvious problem with the methods described above. The use of K_f or K_t requires the possibility to define a nominal stress. However, this is contrary to the intention to treat problems with the effective notch stress approach where

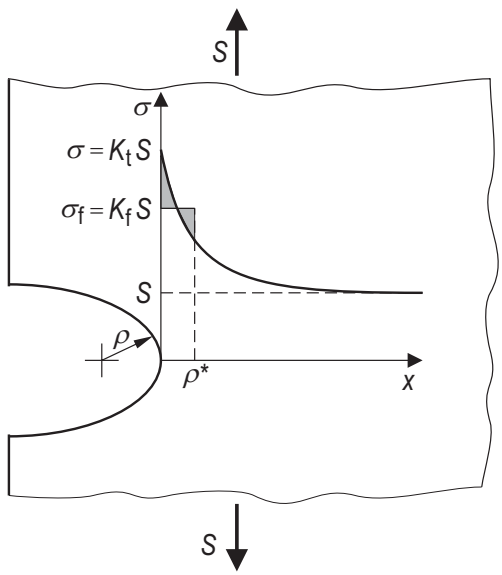

Figure 2.4: Relation between the fatigue notch factor and the micro-structural support length, ρ^*.

no nominal stress can be defined meaningfully. This problem becomes especially evident, if FE results are to be used, since an FE analysis does not give stress concentration factors but stresses. For generous notches, $K_\mathrm{f} = K_\mathrm{t}$ may be a sufficient assumption and the calculated stresses can be used directly. For sharper notches $K_\mathrm{f} < K_\mathrm{t}$, hence a method is required to reduce the calculated stresses without having K_f. Usually, such a method is based on the modulus of the relative stress gradient, χ, at the notch root perpendicular to the surface of the notch:

$$\chi = \left| \frac{1}{\sigma_\mathrm{max}} \frac{\mathrm{d}\sigma}{\mathrm{d}x} \right|_{x=0} . \tag{2.14}$$

In the case of U-notches in flat components or U-shaped circumferential notches in cylindrical parts, χ is well approximated by:

$$\chi = \chi_\mathrm{notch} + \chi_\mathrm{bending} \approx \frac{2}{\rho} + \frac{2}{d} , \tag{2.15}$$

where ρ represents the notch radius and d denotes either the diameter or the width of the component [11].

To illustrate the method, a first order approach will be developed. In its simplest form, approximating the stress distribution near the notch root, see Fig. 2.4, with a linear function, the following gradient approach may be derived:

$$\chi \approx \frac{1}{\sigma_\mathrm{max}} \frac{\sigma_\mathrm{max} - \sigma_\mathrm{f}}{\rho^*/2} . \tag{2.16}$$

Rearranging gives

$$\sigma_\mathrm{f} = \left(1 - \frac{\rho^*}{2}\chi\right) \sigma_\mathrm{max} . \tag{2.17}$$

The relative stress gradient, χ, and the local stress, σ_max, may be found from an FE analysis. With ρ^* known for the actual material, the fatigue-effective notch stress, σ_f, can be calculated.

Based on the work done by Siebel and co-workers [47–49] and included in [50], the approach is founded on the idea that the material in the highly stressed region directly ahead of the notch is "supported" by the lower stressed material deeper inside the component. Contrary to Eq. 2.9 the fatigue notch factor and the stress concentration factor are assumed to be directly proportional:

$$K_{\mathrm{f}} = \frac{K_{\mathrm{t}}}{n_{\chi}}\,, \tag{2.18}$$

which will prove the main asset of this method, since it implies that the fatigue-effective notch stress is directly proportional to the notch stress:

$$\sigma_{\mathrm{f}} = K_{\mathrm{f}} S = \frac{K_{\mathrm{t}} S}{n_{\chi}} = \frac{\sigma}{n_{\chi}}\,. \tag{2.19}$$

The proportionality factor, n_{χ}, is called support coefficient. Knowing this, the fatigue-effective notch stress can be readily found from the local stress of an FE analysis. The support coefficient may be estimated from the empirical equation

$$n_{\chi} = 1 + \sqrt{\rho^{\mathrm{o}} \chi}\,, \tag{2.20}$$

introduced by Petersen [51]. The material dependent parameter, ρ^{o}, is called the slip layer thickness.

2.5.3 A comparison

Four different approaches to express the fatigue notch effect of a component have been discussed and it must be interesting to see if they yield similar results, something they should if they are applicable. Again, a round bar with a circumferential semi-circular notch subjected to a tensile load is employed. Figgure 2.5 is obtained using the equation to calculate K_{t} given in [44] with the net-section radius set to 10 mm. For aluminium alloys the material parameters were found to $\rho_0 = 0.64$ mm [42], $\rho^* = 0.2$ mm [11] and $\rho^{\mathrm{o}} = 0.075$ mm [11].

The curves in Fig. 2.5 are relatively close to each other and more data, hence more accurate material constants, may give even better results. As is often the case, the material data are a weak point, especially in case of aluminium, where only average values are given. Even the simple approach approximating the stress distribution with a linear relationship, see Eq. 2.17, gives comparable results.

2.5.4 Radaj's effective notch stress approach

Applying Eq. 2.13 to welded joints, Radaj [18] found that $\rho_{\mathrm{f}} = 1$ mm, resulting from the assumptions $\rho^* = 0.4$ mm, $s = 2.5$ and $\rho = 0$, gives reasonable agreement for welded joints in structural steel. The conservative assumption of $\rho = 0$ effectively bypasses the problem of identifying the actual weld toe radius, which makes the method highly attractive. Both failure from the weld toe and the weld root can be treated. This increases the applicability of the method compared to the structural hot spot stress approach, which is only applicable to failures from the weld toe. This version of the effective notch stress method is implemented

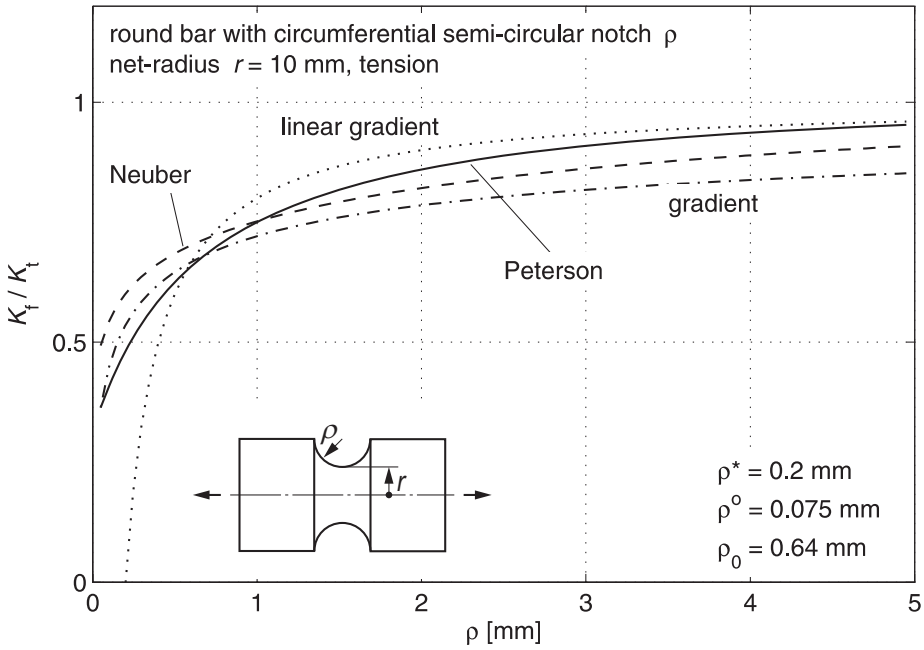

Figure 2.5: K_f/K_t as a function of the notch radius ρ comparing Peterson's and Neuber's approaches and the gradient approaches Eqs. 2.17 and 2.19. The equation to calculate K_t was taken from [44].

in various design codes, e.g., [6, 28]. The fatigue notch factors obtained using $\rho_f = 1$ mm are tabulated for a wide range of different joint geometries in [18], or can be calculated with an FE analysis. Both DNV [28] and IIW [6] recommend to use $\rho_f = 1$ mm for joints made from plates thicker than 5 mm only.

IIW recommends to use $\rho_f = 1$ mm for aluminium alloys too and suggests a design curve (FAT 75). However, since $\rho^* = 0.1 \ldots 0.2$ mm applies for aluminium alloys (2000 series) [46], strictly following Radaj's reasoning would lead to $\rho_f = 0.25 \ldots 0.5$ mm, a fact that also Sonsino et al. [52] pointed out.

2.5.5 Principal or equivalent stress

When using the effective notch stress approach, the question appears which stress, maximum principal or an equivalent stress (Tresca, von Mises), should be used. Figure 2.6 compares the Tresca, von Mises and maximum principal stress surfaces. Actually, the maximum principal stress criterion is mainly used as a fracture criterion for brittle materials, e.g., cast iron. In quadrant I, however, it is equal to the Tresca criterion. Comparing the principal and the von Mises stress criteria it is seen that in quadrant I the principal stress surface is inscribed in the von Mises ellipse, thus the principal stress criterion is the more conservative of the two. However, both criteria differ with a maximum of 15 % in quadrant I, hence, in most cases it is not important which of the two is used. In quadrants II and IV the von Mises stress is more conservative than the maximum principal stress.

Using the von Mises equivalent stress care must be taken, since the spot with the highest stress might be in compression (the negative sign is lost), i.e., it will

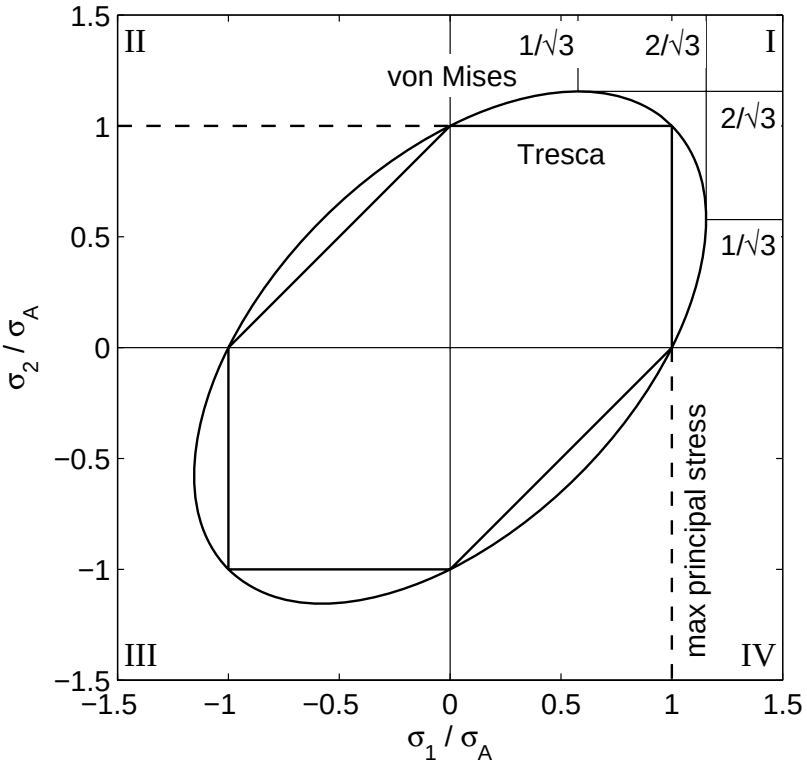

Figure 2.6: Tresca, von Mises and maximum principal stress surfaces.

not be the spot most that is critical to fatigue.

Traditionally the principal stress perpendicular to the weld is used with the structural hot spot stress approach, whereas local approaches usually apply the von Mises equivalent stress. Both conventions are followed in this work.

2.6 Crack propagation analysis

A typical application of a crack propagation analysis would be to check if a detected crack (or a crack just smaller than detectable) will grow to a critical size before the next inspection. It is obvious that an initial crack or crack-like defect is required for this method to work.

It is obvious too, that cracks may be different in shape and size and that they may either lie inside a body or on its surface and that these characteristics are important with respect to the behaviour of the crack. In the introduction to [53], Miller and de los Rios classify cracks according to their size. A crack is considered physically short when its dimensions are comparable to the size of the microstructural units in the material, e.g., grain size, hence the crack propagation behaviour cannot be described using continuum mechanics. Whether a crack can be classified as geometrically short or long depends not only on its size, but also on the loading, hence the size of the plastic zone. A crack is geometrically short, when it is larger than a couple of grains but still small compared to the plastic zone around the crack tip. Finally, a crack is called long when it is large compared

to the plastic zone at its tip. It must be noted that, if subjected to high enough loads, a long crack can behave like a geometrically short crack [53].

2.6.1 Linear elastic fracture mechanics

Linear elastic fracture mechanics (LEFM) states that the singular stress field ahead of a crack tip is completely described by the stress intensity factors K_{I}, K_{II} and K_{III}, which correspond to the three basic crack surface displacement modes. Often mode I is dominant and the contributions from modes II and III can be neglected. The stress intensity factor, denoted by K, is defined as

$$K = FS\sqrt{\pi a}\,. \tag{2.21}$$

F is a function of geometry, crack size and loading, S is the applied nominal stress and a the crack depth. Since fatigue failure is caused by variable loading, K and S in Eq. 2.21 are replaced by the stress intensity factor range, ΔK, and the stress range, ΔS, respectively:

$$\Delta K = F\Delta S\sqrt{\pi a}\,. \tag{2.22}$$

2.6.2 Crack propagation behaviour

When plotting the crack propagation rate, $\mathrm{d}a/\mathrm{d}N$, versus the stress intensity factor range, ΔK, using logarithmic scales, a plot similar to Fig. 2.7 is usually obtained for long cracks in metals. Below the threshold stress intensity factor range, ΔK_{th}, a long crack does not propagate. When ΔK exceeds ΔK_{th}, the crack will start to propagate with a low but rapidly increasing crack growth rate. Eventually the propagation rate reaches the straight part of the curve (log-log linear), which is often referred to as stable crack propagation phase or Paris' regime. During this propagation phase, the $\mathrm{d}a/\mathrm{d}N$ versus ΔK plot is given by the simple power-law suggested by Paris and Erdogan [54], Eq. 2.23. Finally, when $K_{\max}$ is getting close to the fracture toughness of the material, K_{Ic}, unstable crack propagation occurs and within relatively few cycles the component will fracture.

Crack propagation laws

A considerable number of crack propagation laws exist which aim at one or more of the above-mentioned crack propagation phases. Summaries are found for example in [55] and [56] and four crack propagation equations will be briefly discussed below.

Paris' law: The most frequently used model to describe crack propagation was suggested by Paris and Erdogan [54] and is usually referred to as Paris' law. Assuming a power-law relationship between the crack propagation rate and the stress intensity factor range of the form

$$\frac{\mathrm{d}a}{\mathrm{d}N} = C\,\Delta K^m\,, \tag{2.23}$$

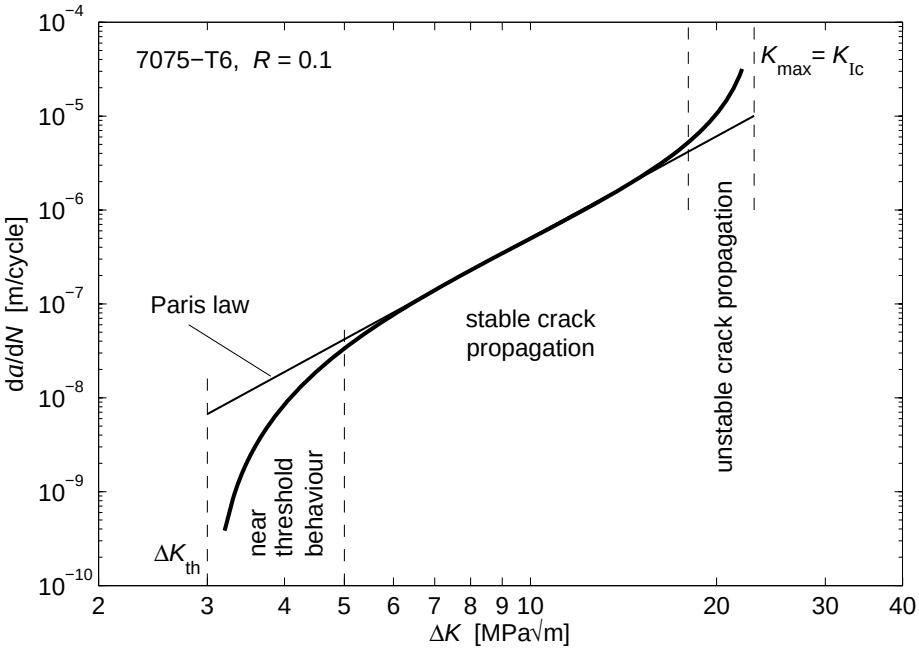

Figure 2.7: Principle propagation behaviour of a long crack and Paris' idealisation.

it accounts for the period of stable crack propagation only. Hence, when plotted to logarithmic scale, Eq. 2.23 is represented by a straight line, see Fig. 2.7. In such a diagram the exponent m is the slope of the curve and C defines its vertical position. Paris' law is dimensionally problematic since the term powered by m is not dimensionless, hence the dimension of C depends on m. Attempts have been made to solve this problem, see for example Bergner and Zouhar [57], however no alternative to Eq. 2.23 has succeeded so far. Paris' law does not describe the regions near ΔK_{th} and K_{Ic}. The effect of mean stress is handled by allowing C to be a function of R. This is discussed in detail in Chapter 3.

Klesnil and Lukáš equation: Klesnil and Lukáš [58] suggested the following equation to extend Paris' law into the near threshold region:

$$\frac{\mathrm{d}a}{\mathrm{d}N} = C\left(\Delta K^m - \Delta K_{\mathrm{th}}^m\right) . \tag{2.24}$$

This equation approaches the additional constant ΔK_{th} asymptotically. The following, slightly different form, which falls more rapidly (usually too rapid) below Paris' law when approaching ΔK_{th}, is also found in the literature:

$$\frac{\mathrm{d}a}{\mathrm{d}N} = C\left(\Delta K - \Delta K_{\mathrm{th}}\right)^m . \tag{2.25}$$

Forman equation: An attempt to extend Paris' law into the region near final fracture and to include the mean stress dependency was proposed by Forman et al. [59]. They suggested the following relation:

$$\frac{\mathrm{d}a}{\mathrm{d}N} = \frac{C_1\left(\Delta K\right)^{m_1}}{(1-R)K_{\mathrm{Ic}} - \Delta K} . \tag{2.26}$$

This equation approaches the materials fracture toughness, K_{Ic}, asymptotically and varies with mean stress, but still ignores the region near threshold. An additional constant, K_{Ic}, has been introduced and the constants C_1 and m_1 differ from those in Paris' law. Except from its ability to deal with mean stress, Forman's equation does not represent a large improvement to Paris' law when considering high cycle fatigue, since the phase of unstable crack propagation usually represents only a negligible part of the total life and is rather unwanted.

Erdogan and Ratwani equation: Erdogan and Ratwani [60] proposed the following equation to include near threshold and near final fracture behaviour and to account for the mean stress dependency:

$$\frac{\mathrm{d}a}{\mathrm{d}N} = \frac{C_2\left(\Delta K - \Delta K_{\mathrm{th}}\right)^{m_2}}{(1-R)K_{\mathrm{Ic}} - \Delta K} \,. \tag{2.27}$$

This equation approaches both K_{Ic} and ΔK_{th} asymptotically, thus it includes all three crack propagation phases and varies with mean stress. However, the dependency of ΔK_{th} on mean stress is not explicitly accounted for. Two additional constants, K_{Ic} and ΔK_{th}, are required compared to Paris' law and the constants C_2 and m_2 differ from those in Paris' law.

Discussion

A description has been given of the approach to approximate the stable crack propagation behaviour by a straight line when $\mathrm{d}a/\mathrm{d}N$ is plotted versus ΔK using logarithmic scale and three equations, which attempt to include either the near threshold or the near final fracture behaviour or both. Other, often more complicated equations exist, but they usually require even more material parameters. Not only if those data are lacking, something that is not uncommon, Paris' law is favourable because of its simplicity.

Measured crack propagation data often suggest that approximating stable crack propagation behaviour by a straight line may be quite rough. Instead, the behaviour may be modelled using Paris' law on a piecewise basis or higher order equations must be used. However, the gain is always bounded by the availability and quality of experimental data.

Applying Paris' law, starting at ΔK_{th}, will underestimate life since $\mathrm{d}a/\mathrm{d}N$ near the threshold is over-predicted. On the other hand, the real near threshold behaviour is difficult to assess and, if the cracks are geometrically small, they may propagate below the long crack propagation threshold and this in addition at high crack propagation rates. Extending Paris' law to the region of unstable crack propagation, the number of cycles spent when approaching K_{Ic} is overestimated. However, the error made is very small, since the period near final fracture contributes only a small fraction to the total life.

2.6.3 Estimating fatigue life

Introducing Eq. 2.22 into Paris' law (Eq. 2.23) gives

$$\frac{\mathrm{d}a}{\mathrm{d}N} = C\left(F\Delta S\sqrt{\pi a}\right)^m \,. \tag{2.28}$$

Integrating Eq. 2.28 from an initial crack length a_i to a crack length a_f, where for example final fracture occurs, results in the number of cycles, N_p, spent during crack propagation

$$N_\mathrm{p} = \frac{1}{C\left(\Delta S\sqrt{\pi}\right)^m} \int_{a_\mathrm{i}}^{a_\mathrm{f}} \left(F\sqrt{a}\right)^{-m} \mathrm{d}a\,. \tag{2.29}$$

For a semi-elliptical surface crack, with depth a and surface width $2c$, a dimension is added and the crack will not only propagate into the component (a-direction), but also along the surface (c-direction). In general the stress intensity factor is different in the two directions, which leads to a varying a/c ratio. This problem is briefly discussed in Appendix B. Geometry and loading make the situation usually even more complicated in a real structure, leading to a change in crack shape and out of plane crack propagation. These cases are not discussed in this work.

In general, to solve Eq. 2.29, numerical integration is required, but in cases where F can be assumed to be constant, the integral can be solved analytically leading to

$$N_\mathrm{p} = \frac{2}{(m-2)C\left(F\Delta S\sqrt{\pi}\right)^m} \left[\frac{1}{a_\mathrm{i}^{\frac{m-2}{2}}} - \frac{1}{a_\mathrm{f}^{\frac{m-2}{2}}}\right]\,. \tag{2.30}$$

In the case when $m = 2$, Eq. 2.30 becomes

$$N_\mathrm{p} = \frac{1}{\pi C\left(F\Delta S\right)^2} \ln\frac{a_\mathrm{f}}{a_\mathrm{i}}\,. \tag{2.31}$$

Summing or integrating Paris' law?

Examining Eq. 2.30, it is seen that, if the final crack depth is set to infinity and $m > 2$, the number of cycles, N_p, is proportional to $a_\mathrm{i}^{\frac{2-m}{2}}$, hence an infinitely deep crack is created within a finite number of cycles. The reason for this paradox lies in the fact that crack propagation is not a continuous process as is assumed when integrating Paris' law. Instead, idealized, a crack propagates an amount Δa in each cycle. Replacing the differential operator, d, with Δ in Eq. 2.28 the crack extension per cycle can be expressed as:

$$\Delta a = C\left(F\Delta S\sqrt{\pi a}\right)^m\,. \tag{2.32}$$

Summation gives the final crack depth as

$$a_\mathrm{f} = a_\mathrm{i} + \sum_{k=1}^{N_\mathrm{p}} \Delta a_k = a_\mathrm{i} + C\left(F\Delta S\sqrt{\pi}\right)^m \sum_{k=1}^{N_\mathrm{p}} a_k^{\frac{m}{2}}\,, \tag{2.33}$$

where the number of crack propagation increments corresponds to the number of cycles required to propagate the crack from a_i to a_f. Summation gives the expected infinite number of cycles to reach an infinitely deep crack. In Fig. 2.8, the difference between integrating and summing Paris' law is illustrated.

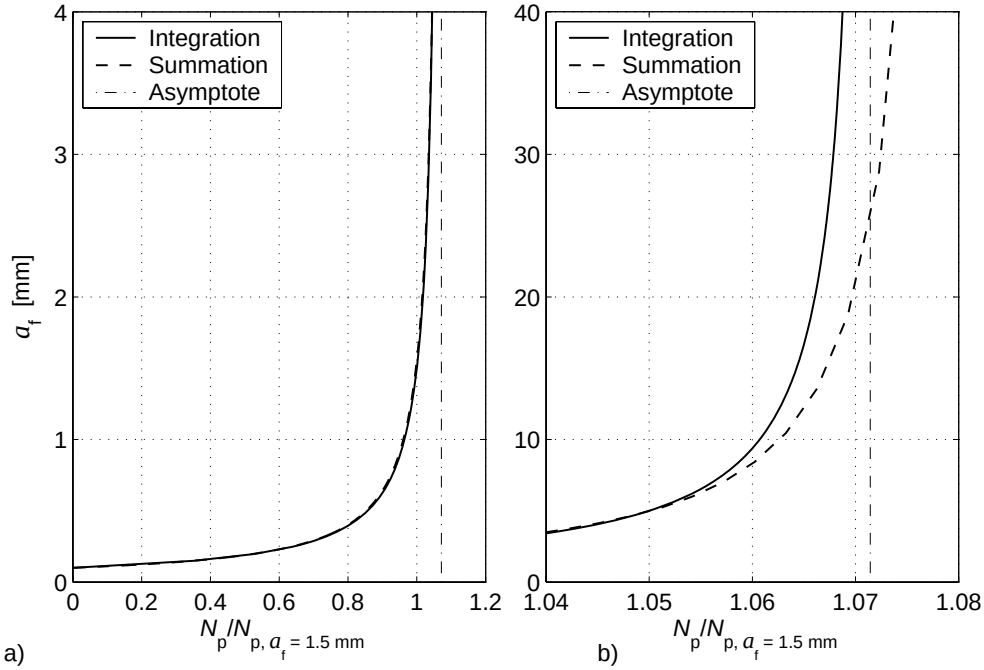

Figure 2.8: Comparison of the final crack length versus number of cycles for a crack with an initial crack depth $a_i = 0.1$ mm ($F = 1.12$, $m = 4.0$, $C = 2 \times 10^{-11}$, $\Delta S = 550$ MPa) when either integrating or summing Paris' law: (a) initial propagation, (b) near asymptotic behaviour.

It must be noted that the smaller the number of cycles to reach a certain crack depth, hence the larger ΔS or C, the greater is the difference between integrating and summing. This behaviour is due to the fact that the larger the crack propagation increments Δa become, the larger the error made when assuming them to be infinitely small ($\mathrm{d}a$). To obtain a clearly visible difference, $\Delta S = 550$ MPa was used in Fig. 2.8. Most practical cases will not suffer from the error made when integrating Paris' law, since, using Eq. 2.30 or 2.33 for realistic crack depths and loads, no considerable difference in the fatigue life is obtained. In addition, often numerical integration is required, which is nothing else than some sort of summation.

2.6.4 An engineering method to treat short cracks

Paris' law is strictly valid for the stable growth of long cracks only. To account for geometrically short cracks, an approach suggested by El Haddad et al. [61], introducing the effective ΔK definition

$$\Delta\tilde{K} = \Delta S\sqrt{\pi(a + a^*)}\,, \tag{2.34}$$

may be used. The parameter a^* is often called characteristic or intrinsic crack length. Härkegård [62] generalized this approach to surface cracks by including the geometry function F:

$$\Delta\tilde{K} = F\Delta S\sqrt{\pi(a + a^*)}\,. \tag{2.35}$$

The characteristic crack length, which marks the intersection between the behaviour of a structure containing a long crack and a non-cracked structure in the Kitagawa-Takahashi-diagram [63], see Fig. 2.9, is found from

$$a^* = \frac{1}{\pi}\left(\frac{\Delta K_{\mathrm{th}}}{F\Delta\sigma_{\mathrm{A}}}\right)^2 , \tag{2.36}$$

where $\Delta\sigma_{\mathrm{A}}$ is the fatigue limit. ΔK_{th} and $\Delta\sigma_{\mathrm{A}}$ depend on mean stress. If

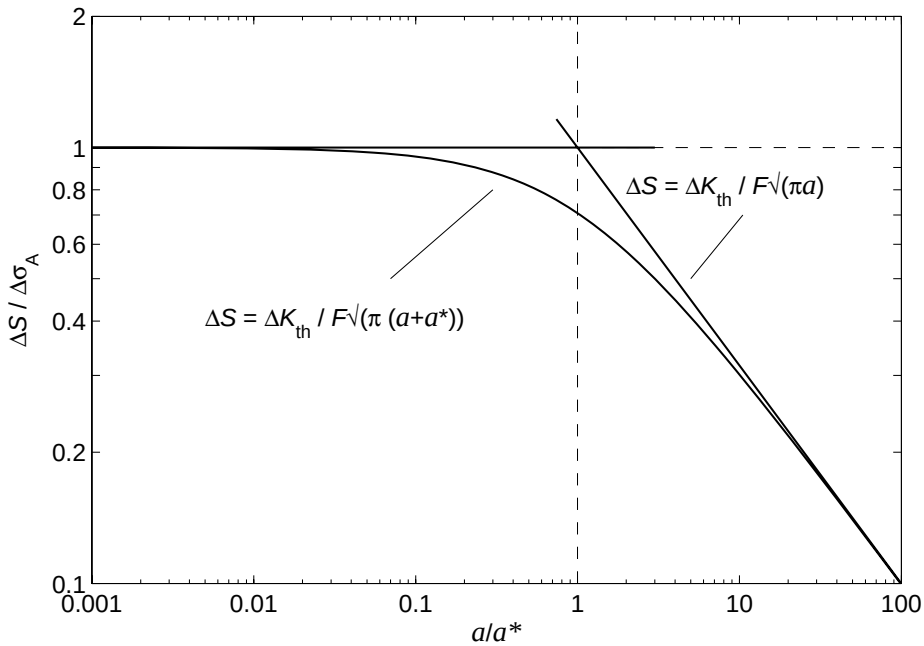

Figure 2.9: Kitagawa-Takahashi-diagram.

the mean stress dependencies can be expressed with Walker's equation, cf. Section 3.3, and $\gamma_{\mathrm{th}} = \gamma_{\mathrm{A}}$, a^* is found to be independent of mean stress. However, in general $\gamma_{\mathrm{th}} \neq \gamma_{\mathrm{A}}$.

Using Eq. 2.35 in combination with Paris' law, gives an increased crack propagation rate at stress intensity factor ranges near ΔK_{th}, which is shown in Fig. 2.10.

The curve in the Kitagawa-Takahashi-diagram, which divides between stresses that lead to fatigue failure and those that are safe,

$$\Delta\tilde{K} = F\Delta S\sqrt{\pi(a+a^*)} = \Delta K_{\mathrm{th}} , \tag{2.37}$$

depends on the crack configuration (a, F). Substituting a and a^* by

$$a = \frac{1}{\pi}\left(\frac{\Delta K}{F\Delta S}\right)^2 \quad \text{and} \quad a^* = \frac{1}{\pi}\left(\frac{\Delta K_{\mathrm{th}}}{F\Delta\sigma_{\mathrm{A}}}\right)^2 , \tag{2.38}$$

leads with some manipulation to

$$\left(\frac{\Delta K}{\Delta K_{\mathrm{th}}}\right)^2 + \left(\frac{\Delta S}{\Delta\sigma_{\mathrm{A}}}\right)^2 = 1 . \tag{2.39}$$

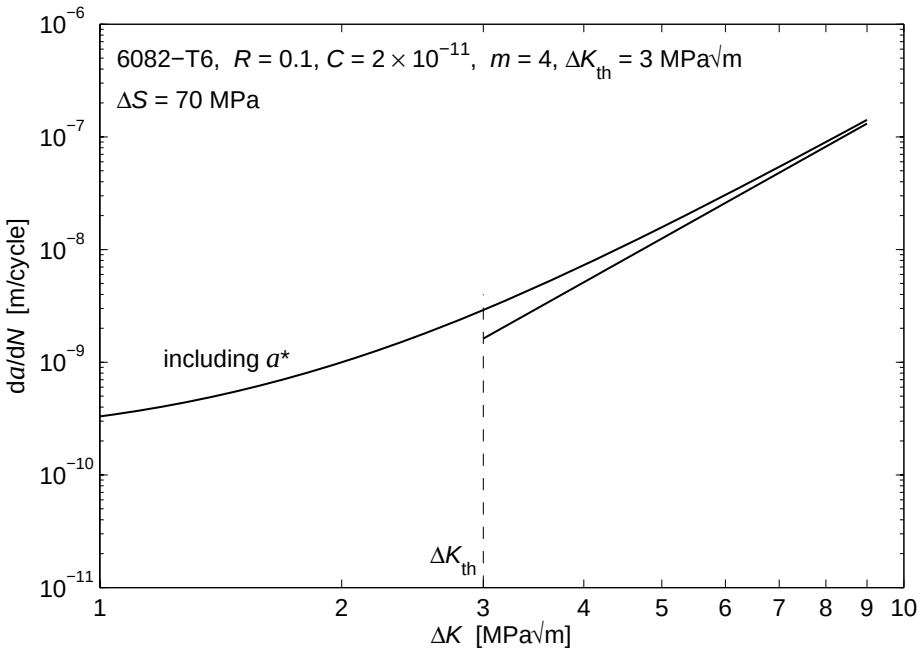

Figure 2.10: Crack propagation rate versus stress intensity factor range with and without a^*.

This equation is independent of the crack configuration [64] and can be seen as some sort of failure assessment diagram, see Fig. 2.11, which combines the fatigue assessment of cracked and non-cracked structures. The diagram offers the possibility to assess cracks which are too short to be treated with respect to ΔK_{th}, but are still too long to be assumed non-existent, hence the transition between initiation and propagation. A structure subjected to a combination of ΔS and ΔK that lies outside the quarter ellipse described by Eq. 2.39 will fail, whereas combination of ΔS and ΔK inside the quarter ellipse will have infinite life.

2.6.5 A crack at a weld toe

A crack starting at a weld toe is subjected to an inhomogeneous, rapidly decreasing stress field caused by the global and local stress concentrations. Especially if the initial crack is short, it will be subjected to the high peak stress near the component surface. The crack propagation approach described so far does not account for the effect of a stress concentration resulting from, for example, a notch. Approaches to include this effect in a crack propagation analysis are described below.

The weld toe magnification factor

The influence of several geometric features such as crack shape, component thickness and width, are accounted for by the geometry factor, F. Therefore, it seems straightforward to account for the stress raising effect of a weld by introducing an additional factor. This factor, usually called weld toe magnification factor

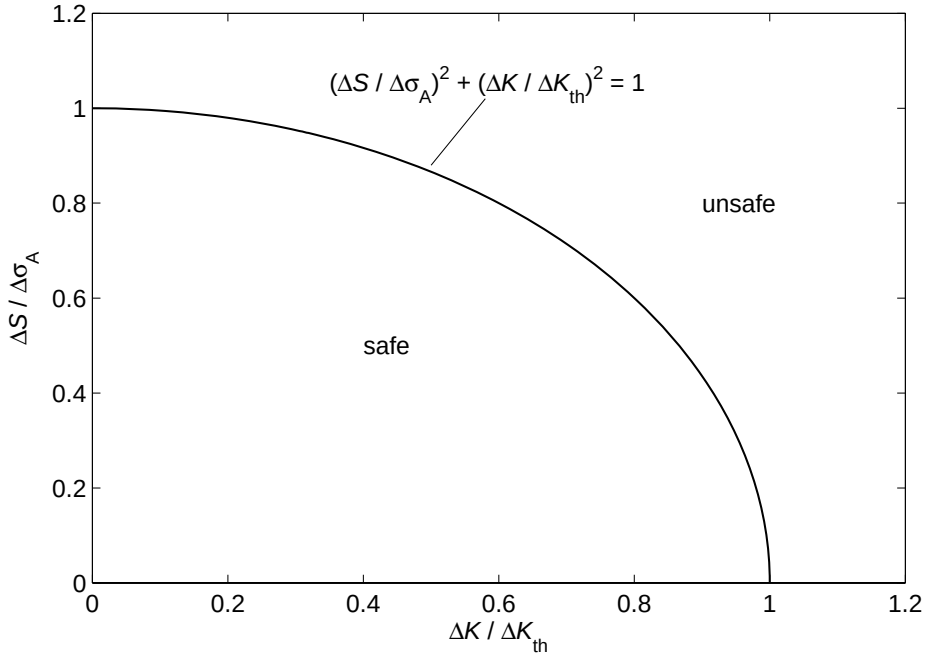

Figure 2.11: Applied Stress range as a function of stress intensity factor range.

and labelled M_{k}, is formally defined as the ratio of the stress intensity factor of a crack at the weld toe and the stress intensity factor of the same crack in a plate subjected to the same external loading:

$$M_{\mathrm{k}} = \frac{K_{(\text{plate with welded attachment})}}{K_{(\text{plate without attachment})}} \,. \tag{2.40}$$

The stress intensity factor range definition for a crack at a weld toe then becomes

$$\Delta K = M_{\mathrm{k}} F \Delta S \sqrt{\pi a} \,. \tag{2.41}$$

It is obvious that M_{k} cannot be constant, since, as the crack propagates, the influence of the stress peak decreases. M_{k} has a sharp peak at the surface that is rapidly decreasing into the material [65], see Fig. 2.12. Therefore, an equation or a set of equations is required to express the M_{k} factor as a function of crack parameters, geometry and loading. Especially in case of two dimensional cracks, these equations become very complex, see Appendix B.3.

Equations to calculate M_{k} can be found in [66,67] and an example is given in Appendix B.3.

Using the local stress distribution

This method is similar to the one described above. Instead of multiplying by a weld toe magnification factor obtained from a case geometrically similar to the one that is to be assessed, the geometry factor, F, is modified to match the local stress distribution. To follow such an idea frees the approach from the restriction to certain joint geometries for which an M_{k} factor equation is available, because

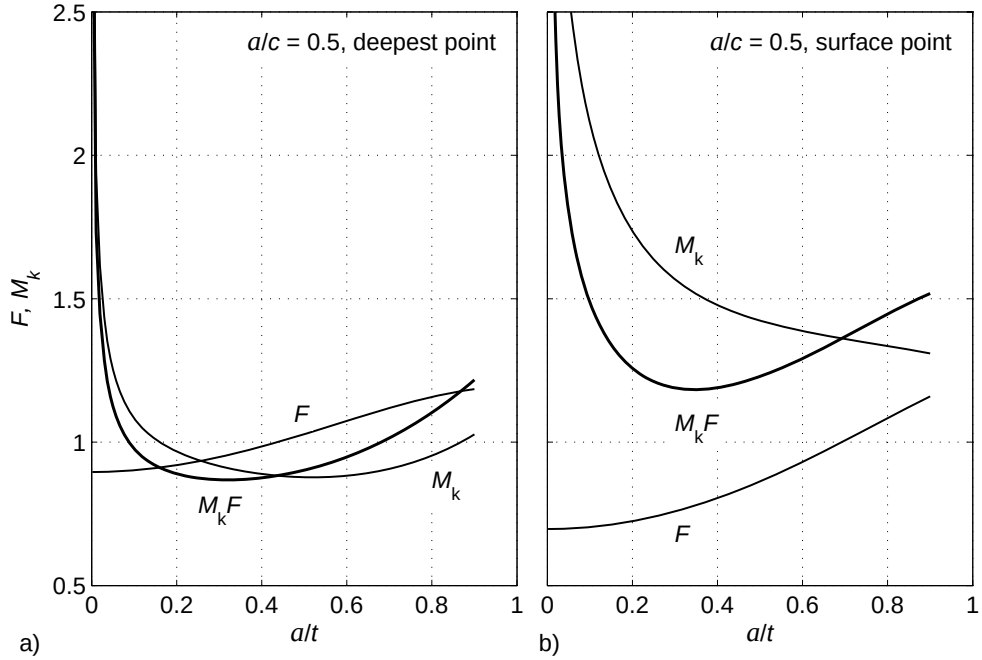

Figure 2.12: Geometry factor F at the deepest point of a semi-elliptical surface crack in a plate subjected to pure tension ($a/c = 0.5$, Newman and Raju [68]) and the weld toe magnification factor, M_k, for a similar crack at the weld toe ($a/c = 0.5$, $l/t = 1.75$, $\theta = \pi/4$, zero weld toe radius, Bowness and Lee [67]) as functions of a/t: (a) deepest point, (b) surface point.

the geometry is reflected in the local stress distribution. This requires the local stress distribution to be known, i.e., a very detailed finite element analysis is needed.

Pommier et al. [69] provided a set of equations to calculate the geometry factor of a semi-elliptical surface crack subjected to a stress field where the stress distribution along surface and depth direction is approximated by a polynomial. However, both distributions may together not exceed a cubic polynomial. Assuming, for example, the stress along the surface to vary linearly, the stress in depth direction can be approximated with a quadratic equation. If the stress along the surface is constant a cubic stress approximation in depth direction is allowed. Since, deriving the set of equations, a semi-infinite plate was assumed, Pommier's solution is only valid for a crack depth up to $a/t \approx 0.25$, where t denotes the plate thickness.

Carpinteri et al. [70] developed a method to find the geometry factor of a semi-elliptical surface crack subjected to a non-linear stress field by superposition of geometry factors from elementary unit stress distributions (constant, linear, quadratic, cubic, forth and fifth order). They obtained the elementary geometry factors, F_n, $n = 0 \ldots 5$, from finite element analyses covering $0.1 \leq a/t \leq 0.7$ and $0.1 \leq a/c \leq 1.2$. In contrast to Pommier et al. [69], F_n was not approximated by a set of equations, but collected in a large table. According to their suggestion, the local stress distribution can be approximated by any continuous function that is five times differentiable. However, since this function is then approximated by

a fifth order polynomial using a Taylor series expansion, it seems reasonable to use a fifth order polynomial, e.g.,

$$\frac{\sigma(\eta)}{S} = B_0 + B_1\eta + B_2\eta^2 + \ldots + B_5\eta^5 = \sum_{n=0}^{5} B_n\eta^n \,, \tag{2.42}$$

The rather unusual definition of the coordinate η is shown in Fig. 2.13. Having the stress distribution in terms of η, the geometry factor corresponding to the given stress distribution is directly found from:

$$F = \sum_{n=0}^{5} F_n B_n \,. \tag{2.43}$$

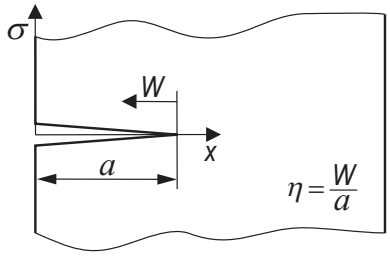

Figure 2.13: Definition of the coordinate η.

Expressing the local stress distribution as a function of η is inconvenient. It is much more practical to give it in terms of x or $\xi = x/t$, e.g.,

$$\frac{\sigma(x/t)}{S} = A_0 + A_1\xi + A_2\xi^2 + \ldots + A_5\xi^5 = \sum_{n=0}^{5} A_n\xi^n \,. \tag{2.44}$$

Thus, a method is required to extract the coefficients B_n from such an equation. Substituting $x = a - w$ and $\eta = w/a$ gives after some manipulation:

$$\begin{bmatrix} 1 & 1 & 1 & 1 & 1 & 1 \\ 0 & -1 & -2 & -3 & -4 & -5 \\ 0 & 0 & 1 & 3 & 6 & 10 \\ 0 & 0 & 0 & -1 & -4 & -10 \\ 0 & 0 & 0 & 0 & 1 & 5 \\ 0 & 0 & 0 & 0 & 0 & -1 \end{bmatrix} \begin{bmatrix} A_0 \\ A_1\alpha \\ A_2\alpha^2 \\ A_3\alpha^3 \\ A_4\alpha^4 \\ A_5\alpha^5 \end{bmatrix} = \begin{bmatrix} B_0 \\ B_1 \\ B_2 \\ B_3 \\ B_4 \\ B_5 \end{bmatrix} , \tag{2.45}$$

where $\alpha = a/t$. Equation 2.45 is equivalent to

$$B_n = \sum_{n=0}^{5} \frac{(-\xi)^n}{n!} \left. \frac{\mathrm{d}^{(n)}\sigma(\xi)/S}{\mathrm{d}(\xi)^{(n)}} \right|_{x=a} . \tag{2.46}$$

To enable the treatment of cracks shorter than $\alpha = 0.1$, Huth [71] linearly extrapolated the F_n values at $\alpha = 0.1$ and 0.2 down to $\alpha = 0.025$. Another possibility would be to use the F_n values at $\alpha = 0.1$ unchanged for shorter cracks too. This should be a good approximation, since the elementary geometry factors converge towards a constant for $\alpha \to 0$. An extrapolation to cracks deeper than $a/t = 0.7$ in a similar manner becomes insecure when approaching $\alpha = 1$. This is not a serious problem, since only a minor part of the propagation life is spend in this region.

Thoughts on using the local stress distribution

The solutions developed to find the stress intensity factor of a crack subjected to the rapidly decreasing stress field ahead of a notch are usually based on finite element calculations of a crack in an unnotched plate. Considering the notch shown in Fig. 2.14a, a crack will be subjected to

$$K = FK_{\mathrm{t}}S\sqrt{\pi a}\,, \tag{2.47}$$

as long as $a \ll d$. As a increases, K will converge towards

$$K = FS\sqrt{\pi(a+d)}\,. \tag{2.48}$$

Hence, the notch depth will act as a part of the crack, which is illustrated in Fig. 2.14b. The real behaviour is marked by the curve connecting the two asymptotes. An equation describing this curve has been proposed by Jergéus [72] and later generalised by Härkegård [62]:

$$K = 1.12S\sqrt{\pi D}\,, \tag{2.49}$$

where the "equivalent" surface crack depth D is defined as

$$D = a + d\left[1 - \exp\left(-\frac{a}{a'}\right)\right]\,. \tag{2.50}$$

The transition crack depth a' marks the crack depth at which the two asymptotic solutions coincide, i.e.,

$$a' = \frac{d}{K_{\mathrm{t}}^2 - 1}\,. \tag{2.51}$$

A more detailed discussion on using asymptotic solutions to calculate K for a crack emanating from the root of a notch is found in Wormsen et al. [73].

The situation is slightly different in case of a stress raiser similar to Fig. 2.15a. Here there is no notch depth that will "add" to the crack depth when the crack becomes deeper. Therefore, the stress intensity factor is defined as

$$K = \begin{cases} FK_{\mathrm{t}}S\sqrt{\pi a} & a \ll r \\ FS\sqrt{\pi a} & a \approx r \end{cases}\,. \tag{2.52}$$

The two asymptotes and the real behaviour are illustrated in Fig. 2.15b.

Approximating the stress intensity factor, i.e., the geometry factor, using solutions obtained from cracks in unnotched plates as described in the preceding section, the effect of the notch depth acting as a part of the crack, see Fig. 2.14, is not accounted for, which may lead to non-conservative life predictions. For cracks propagating from stress raisers similar to Fig. 2.15a, which are representative for weld-like notches, such a problem is not encountered.

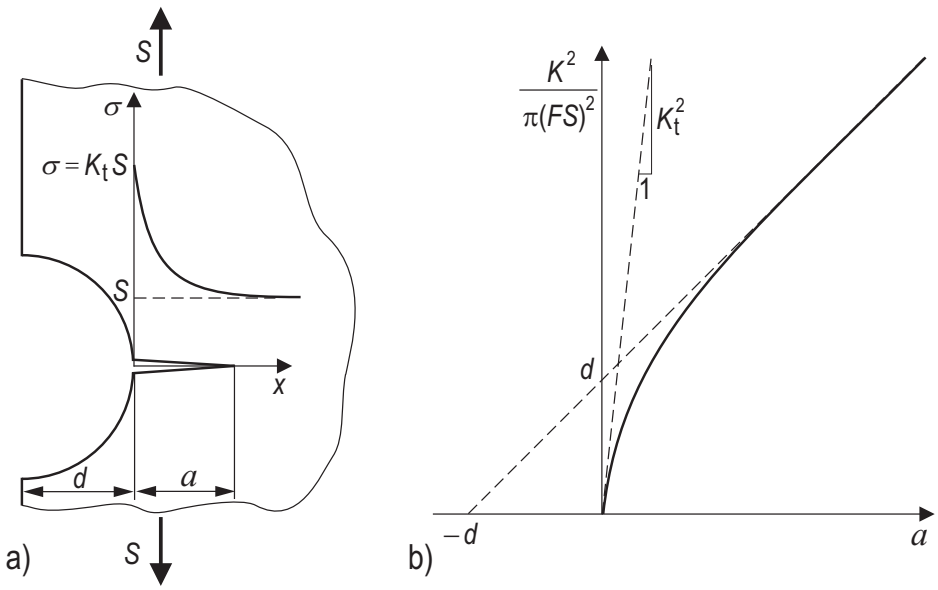

Figure 2.14: (a) Crack at the root of a notch and (b) behaviour of the stress intensity factor as a function of a.

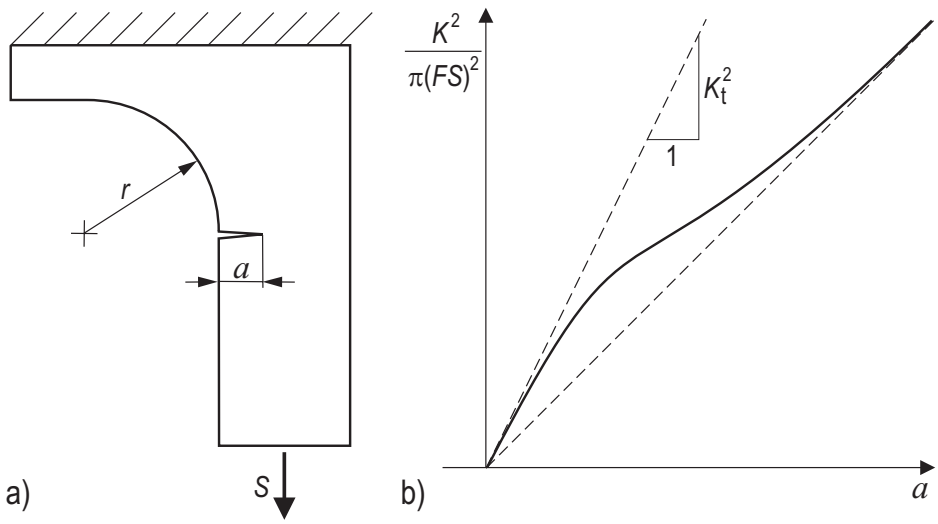

Figure 2.15: (a) Crack at the root of a shoulder fillet and (b) behaviour of the stress intensity factor as a function of a.

CHAPTER 3

The influence of mean stress on fatigue crack propagation

This chapter addresses the mean stress dependency of the fatigue process with an emphasis on fatigue crack propagation. After a short introduction Walker's equation and variations thereof are discussed. To evaluate their applicability they have been fitted to crack propagation data from several aluminium alloys. A modified least mean squares method has been derived to fit the crack propagation data to Walker's equation. Then a new mean stress equation, which covers the whole range from $-1 \leq R < 1$ with a single expression, has been proposed and evaluated.

The main focus is directed at equations that directly address the mean stress dependency of crack propagation data. Crack closure based mean stress equations are briefly mentioned only. These equations relate the closure behaviour of a crack to its growth rate. This physical basis makes the method attractive, however, as Kujawski [74–76] points out when proposing a variation of Walker's equation, relating crack growth data to crack closure data the results are not always distinct.

3.1 Introduction

Though it is the stress amplitude that drives crack initiation and propagation, a tensile mean stress accelerates and a compressive mean stress retards the fatigue process. Both must therefore be considered in analysis. The mean stress level is often, especially in association with crack propagation, characterized by the stress ratio, R, which is defined as

$$R = \frac{\sigma_{\min}}{\sigma_{\max}} = \frac{K_{\min}}{K_{\max}} \,. \tag{3.1}$$

Consequently, instead of referring to the mean stress dependency, the terms "stress ratio effect" or "stress ratio dependency" are often used.

If material data such as the fatigue limit, S-N-curves, the threshold stress intensity factor range and the crack growth rate, are available at the stress ratio prevailing in the component to be designed, those data can be used directly. However, this is often not the case and, having variable amplitude loading, the stress ratio will be a variable itself. Therefore, a relation to adjust the fatigue strength to a certain mean stress or stress ratio is generally required.

For welded joints the picture is usually slightly different. They already contain mean stresses in form of residual stresses resulting from contraction of the weld whilst cooling down. Residual stresses are self-equilibrating and vary between tension and compression. They may reach yield stress magnitude, hence the high residual stress will dominate over the applied mean stress. This results in high stress ratios at the weld that are almost independent of the applied stress ratio, which explains the relatively weak mean stress dependency of welded structures. From this point of view, it seems paradoxical that this work has a focus on embedding the mean stress dependency in analysis. However, with the introduction of extensive and well documented methods and recommendations for fatigue life enhancements suggested by IIW [10] and allowed for in, e.g., [5], and the significant improvements made in welding simulations of aluminum alloys recently made, [32, 77, 78], the importance of qualitatively coping with mean stress dependency has become much more important. Being able to introduce favourable residual stresses at the expected failure site, it is desirable to predict their positive effect in analysis, hence, to be able to use them in design.

3.2 Mean stress equations – a short introduction

3.2.1 Fatigue crack initiation

To transform the fatigue limit or an S-N curve, which is not given at the required mean stress, a Haigh-diagram (plotting σ_a versus σ_m) is often used. If such a diagram cannot be based on experimental data obtained at different mean stress levels, a number of equations to approximate the mean stress effect have been proposed, see for example [11, 12]. Common approaches are the modified Goodman equation

$$\frac{\sigma_\mathrm{a}}{\sigma_\mathrm{W}} + \frac{\sigma_\mathrm{m}}{R_\mathrm{m}} = 1\,, \tag{3.2}$$

and the equation suggested by Gerber

$$\frac{\sigma_\mathrm{a}}{\sigma_\mathrm{W}} + \frac{\sigma_\mathrm{m}^2}{R_\mathrm{m}^2} = 1\,. \tag{3.3}$$

Gerber's equation is only valid for $\sigma_\mathrm{m} > 0$. Since the modified Goodman equation is usually quite conservative at higher mean stresses, it has been modified by replacing R_m with either $\widetilde{R}_\mathrm{m}$, the true fracture strength of the material, or σ'_f, the factor from Basquin's law, Eq. 2.1, representing the S-N curve of an unnotched specimen at $\sigma_\mathrm{m} = 0$. This modification is usually ascribed to Morrow [79]. It is of little importance if either $\widetilde{R}_\mathrm{m}$ or σ'_f is chosen, since they are often approximately equal. In addition, the line described by the modified Eq. 3.2 is cut off

at $\sigma_\mathrm{m} + \sigma_\mathrm{a} = R_\mathrm{m}$, hence the part where the difference between $\widetilde{R}_\mathrm{m}$ and σ'_f would have the largest effect is not included. Fig. 3.1 illustrates both Eq. 3.2 and its modification assuming $\sigma'_\mathrm{f} = 2R_\mathrm{m}$. Another approach, which works especially well

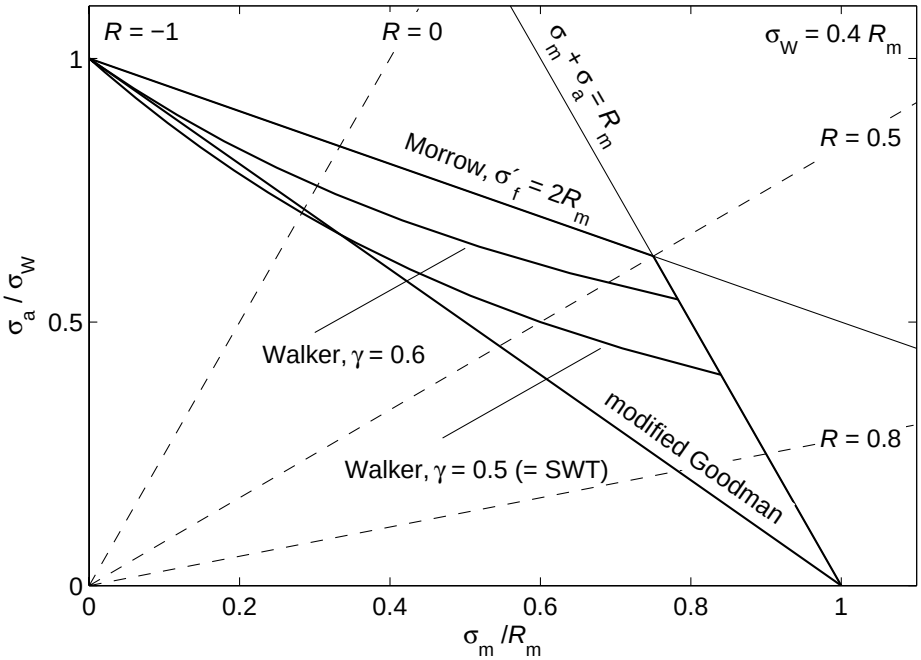

Figure 3.1: Approximated Haigh-diagram.

for aluminium alloys [12], has been proposed by Smith, Watson and Topper [80]. They define an effective stress amplitude at $\sigma_\mathrm{m} = 0$, $\sigma_\mathrm{a,SWT}$, as

$$\sigma_\mathrm{a,SWT} = \sqrt{\sigma_\mathrm{a}\sigma_\mathrm{max}}\,, \tag{3.4}$$

where linear elastic behaviour is assumed. This relation is included in Fig. 3.1 as well. The stress ratio equation suggested by Walker [81] will be described in Section 3.3.

3.2.2 Fatigue crack propagation

The main reason for the crack propagation rate to vary with R is crack closure, which was first investigated by Elber [82]. The higher the mean stress, hence the higher R at given $\Delta\sigma$, the longer a crack is open during a stress cycle, thus the larger is the part of the cycle that contributes to crack propagation. The contributing part of the cycle is usually called the effective part. For the aluminium alloy 2024-T3, Elber suggested an effective stress intensity factor range

$$\Delta K_\mathrm{eff,Elber} = K_\mathrm{max} - K_\mathrm{op} = (0.5 + 0.4R)\Delta K\,, \tag{3.5}$$

with a validity range of $-0.1 \leq R \leq 0.7$. To cover negative stress ratios, Schijve [83] modified Elber's approach to:

$$\Delta K_\mathrm{eff,Schijve} = [0.55 + (0.45 - \alpha)R + \alpha R^2]\Delta K\,. \tag{3.6}$$

Using $\alpha = 0.12$, Schijve obtained the best fit for the aluminium alloy 2024-T3 covering $-1 \leq R < 1$. From Eq. 3.5 it follows that $\Delta K(R = 0) = 2K_{\text{eff,Elber}}$. Using this relation to eliminate $K_{\text{eff,Elber}}$ in Eq. 3.5, the resulting relation is plotted in Fig. 3.2. After having eliminated $K_{\text{eff,Schijve}}$ in Eq. 3.6 in the same manner, this equation has been included in Fig. 3.2.

Both Elber's and Schijve's equations are based on crack closure data. An equation to describe the mean stress dependency of crack propagation data directly will be discussed in detail in the next section.

3.3 Walker's equation

Walker [81] proposed an effective stress range at $R = 0$, $\Delta\sigma_{\text{Walker}}$, for crack propagation and fatigue failure of non-cracked structures as a function of the maximum stress, σ_{max}, and the stress ratio, R, as

$$\Delta\sigma_{\text{Walker}} = (1 - R)^{\gamma}\, \sigma_{\text{max}} \,. \tag{3.7}$$

Expressing σ_{max} in terms of stress range and stress ratio, $\sigma_{\text{max}} = \Delta\sigma/(1 - R)$, and introducing it into Eq. 3.7 gives

$$\Delta\sigma_{\text{Walker}} = \frac{\Delta\sigma}{(1 - R)^{1-\gamma}} \,. \tag{3.8}$$

3.3.1 Fatigue crack initiation

As indicated in Section 3.2.1, the influence of mean stress on the fatigue of non-cracked structures and the fatigue limit is often given in form of a Haigh-diagram. Replacing stress range with stress amplitude in Eq. 3.8 and setting $\sigma_{\text{a}}(R = -1) = \sigma_{\text{W}}$, gives $\sigma_{\text{a,Walker}} = \sigma_{\text{W}}/2^{1-\gamma_{\text{A}}}$. Applying this relation to eliminate $\sigma_{\text{a,Walker}}$, and introducing Eq. 3.1 gives

$$\sigma_{\text{a}} = \frac{\sigma_{\text{W}}}{2^{1-\gamma_{\text{A}}}} \left(1 - \frac{\sigma_{\text{m}} - \sigma_{\text{a}}}{\sigma_{\text{m}} + \sigma_{\text{a}}}\right)^{1-\gamma_{\text{A}}} \,, \tag{3.9}$$

and after some manipulation

$$\frac{\sigma_{\text{m}}}{R_{\text{m}}} = \frac{\sigma_{\text{W}}}{R_{\text{m}}} \left[\left(\frac{\sigma_{\text{a}}}{\sigma_{\text{W}}}\right)^{\frac{1}{\gamma_{\text{A}}-1}} - 1\right] \frac{\sigma_{\text{a}}}{\sigma_{\text{W}}} \,. \tag{3.10}$$

This function, assuming $\sigma_{\text{W}} = 0.4R_{\text{m}}$, is plotted together with the modified Goodman and the Morrow line in the Haigh-diagram in Fig. 3.1. It can be seen that Walker's equation using $\gamma = 0.5$ is in good agreement with the modified Goodman line for $-1 \leq R \leq 0.5$. $\gamma = 0.6$ results in a behaviour that lies in between the modified Goodman and the Morrow line. As for Morrow's approach, the curve described by Eq. 3.10 must be cut off at $\sigma_{\text{m}} + \sigma_{\text{a}} = R_{\text{m}}$.

Setting $\gamma = 0.5$ and $R = -1$, Eq. 3.8 yields

$$\Delta\sigma(R = -1) = \sqrt{2}\, \Delta\sigma_{\text{Walker}} = \sqrt{2}\frac{\Delta\sigma}{\sqrt{1 - R}} \,. \tag{3.11}$$

With $1 - R = \Delta\sigma/\sigma_{\max}$ and $\Delta\sigma = 2\sigma_{\mathrm{a}}$ Eq. 3.11 becomes

$$\sigma_{\mathrm{a}}(R = -1) = \sqrt{\sigma_{\mathrm{a}}\sigma_{\max}} = \sigma_{\mathrm{a,SWT}}\,, \tag{3.12}$$

which is identical with the effective stress proposed by Smith, Watson and Topper [80]. Hence, the equation by Smith, Watson and Topper is seen to be a special case of Walker's equation.

3.3.2 Fatigue crack propagation

Expressed in terms of the stress intensity factor range, Walker's equation, Eq. 3.8, becomes

$$\Delta K_{\mathrm{Walker}} = \frac{\Delta K}{(1-R)^{1-\gamma}}\,. \tag{3.13}$$

At positive stress ratios the exponents usually take values between 0.3 and 0.8, where $\gamma = 0.3$ gives a strong and $\gamma = 0.8$ a weak dependency on R, cf. Fig. 3.2.

When a crack is closed, it will not propagate, hence the part of the cycle during which the crack is closed does not contribute to propagate the crack. Assuming a crack to be closed when subjected to a compressive load, only $K_{\max}$ drives the crack if $R \leq 0$. This behaviour is obtained by setting $\gamma = 0$, which gives

$$\Delta K_{\mathrm{Walker}} = \frac{\Delta K}{1-R} = K_{\max}\,. \tag{3.14}$$

A more detailed discussion about how to apply Walker's equation to relate available material data to the loading situation is given in Appendix A.

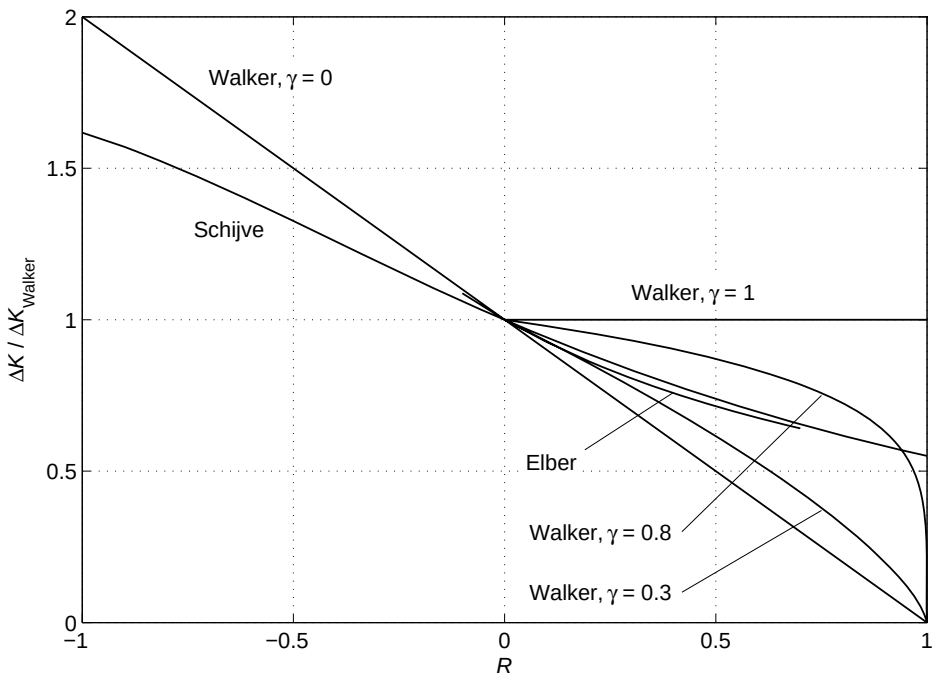

Figure 3.2: Graphical representation of Walker's equation (Eq. 3.13) for different exponents, Elber's and Schijve's equations (Eqs. 3.5 and 3.6, respectively).

3.3.3 The Walker exponent

If the mean stress dependency of crack propagation data is to be expressed by Walker's equation, the Walker exponent must be known. If crack propagation data at two different mean stress levels are available, a Walker exponent could be calculated directly. However, due to the large scatter in data, it is a rather unreliable method to base the Walker exponent on values at two stress ratios only. Having crack propagation data at more than two different mean stress levels, the Walker exponent can be found by means of linear regression.

In Table 3.1 crack propagation data for the aluminium alloys 7075-T6 and 2024-T3 obtained from [5, 12, 84–91] are given. Having data at different R values, the Walker exponent is now calculated using a modified least mean squares method (see Appendix A.3). It must be mentioned that in most sources the crack propagation data are given in form of $\mathrm{d}a/\mathrm{d}N$ versus ΔK plots. This requires a visual curve fit, which, of course, is quite a subjective process. In addition, the experimental data do not always represent the complete phase of stable crack propagation and can often only roughly be fitted by a straight line.

A Walker exponent valid throughout the phase of stable crack propagation requires that the exponent m in Paris' law is not a function of R. However, this is not the case for the crack propagation data given in Table 3.1. One possibility to overcome this problem would be to rotate all curves to match a mean slope. Choosing the pivot points in a region ($\mathrm{d}a/\mathrm{d}N$ or ΔK) characteristic for the initial crack size to be analysed would be reasonable, since most of the life is spent there. Another possibility to deal with the different exponents would be to calculate a Walker exponent at different $\mathrm{d}a/\mathrm{d}N$ levels, hence to make γ a function of $\mathrm{d}a/\mathrm{d}N$. Here, γ was calculated at $\mathrm{d}a/\mathrm{d}N = 1\times10^{-8},\ 1\times10^{-7}$ and 1×10^{-6} m/cycle. The points obtained, as well as the regression lines are plotted in Fig. 3.3 and Fig. 3.4 and the corresponding Walker exponents are given in Table 3.2. In addition, Fig. 3.3 and Fig. 3.4 contain lines described by Elber's and Schijve's equations.

It is seen rather unexpectedly, that the Walker exponents vary insignificantly between the three different $\mathrm{d}a/\mathrm{d}N$ levels. For positive stress ratios, a Walker exponent of approximately 0.64 fits the experimental data for the 7075-T6 aluminium alloy best. Walker [81] and Dowling [12] suggested $\gamma = 0.425$ and $\gamma = 0.64$, respectively. With $\gamma = 0.61$ a slightly lower value suits the data for the 2024-T3 aluminium alloy. For this alloy [81] and [12] give $\gamma = 0.5$ and $\gamma = 0.68$, respectively. It is also seen from Fig. 3.3 that taking $\gamma = 0$ for negative stress ratios is a good assumption in the case of the 7075-T6 aluminium alloy. Reliable predictions regarding the Walker exponent for the 2024-T3 aluminium alloy at negative stress ratios cannot be made due to the lack of data. However, there is a tendency towards a positive Walker exponent at negative stress ratios.

Taking the relatively large scatter in the $\mathrm{d}a/\mathrm{d}N$ data into account, a Walker exponent $\gamma(R \leq 0) = 0.6$ would be a realistic assumption for both alloys.

In Chapter 4 will be investigated if $\gamma = 0.6$ is applicable to the 6082-T6 aluminium alloy as well.

Table 3.1: Paris constants for the aluminium alloys 7075-T6 and 2024-T3.

Source	R	7075-T6 C (m/cycle, MPa$\sqrt{\text{m}}$)	7075-T6 m	2024-T3 C (m/cycle, MPa$\sqrt{\text{m}}$)	2024-T3 m
Broek and Schijve [84]	0.66	7.00×10^{-11}	4.20	2.00×10^{-10}	3.00
	0.57	1.00×10^{-10}	3.80	2.00×10^{-10}	2.80
	0.50	2.00×10^{-11}	4.30	7.00×10^{-11}	3.20
	0.38	7.00×10^{-11}	3.80	1.00×10^{-10}	2.90
	0.29	2.00×10^{-10}	3.30	2.00×10^{-10}	2.60
	0.17	8.00×10^{-11}	3.40	2.00×10^{-10}	2.60
	0.06	3.00×10^{-11}	3.70	2.00×10^{-10}	2.50
Bu and Stephens [85]	0.50	9.17×10^{-11}	3.64		
	0.05	1.25×10^{-11}	3.99		
	-1.00	2.03×10^{-12}	3.61		
Donald and Paris [86]	0.70			1.25×10^{-10}	3.36
	0.10			1.46×10^{-11}	3.92
Dowling [12]	0.00	2.71×10^{-11}	3.70		
DTDH [87]	0.70	6.95×10^{-11}	3.69	6.75×10^{-11}	3.07
	0.50			8.68×10^{-11}	3.02
	0.33	1.77×10^{-10}	3.00	7.30×10^{-11}	3.01
				8.21×10^{-11}	2.96
	0.10			5.30×10^{-11}	2.90
	0.00	4.37×10^{-11}	3.21	3.36×10^{-11}	2.94
				5.00×10^{-11}	2.93
				2.71×10^{-11}	3.27
	-0.33	1.47×10^{-11}	3.40		
	-0.60	3.89×10^{-12}	3.49		
	-1.00	4.41×10^{-12}	3.32	1.05×10^{-12}	3.71
Durán et al. [88]	0.70	1.04×10^{-10}	3.83		
	0.10	1.30×10^{-10}	3.59		
Eurocode 9 [5]	0.80			1.60×10^{-10}	3.39
	0.10	8.65×10^{-11}	3.49		
Fleck and Anderson [89]	0.75	3.60×10^{-10}	3.29	1.60×10^{-10}	3.28
	0.50	2.55×10^{-10}	3.06	1.50×10^{-10}	3.08
	0.10	1.65×10^{-10}	3.00	9.83×10^{-11}	3.00
Hudson [90]	0.80	1.32×10^{-10}	4.00		
	0.70			2.92×10^{-11}	3.86
	0.50	4.14×10^{-11}	3.88	7.86×10^{-11}	3.29
	0.33	8.30×10^{-11}	3.50	9.00×10^{-11}	3.14
	0.00	3.40×10^{-11}	3.56	1.77×10^{-11}	3.46
	-0.33	1.35×10^{-11}	3.58		
	-0.60	6.14×10^{-12}	3.58		
	-0.70	1.69×10^{-12}	3.87		
	-1.00	3.24×10^{-12}	3.59	2.31×10^{-13}	4.17
Wu et al. [91]	0.50	1.96×10^{-10}	3.40		
	0.00	3.22×10^{-11}	3.56		
	-1.00	8.03×10^{-12}	3.48		

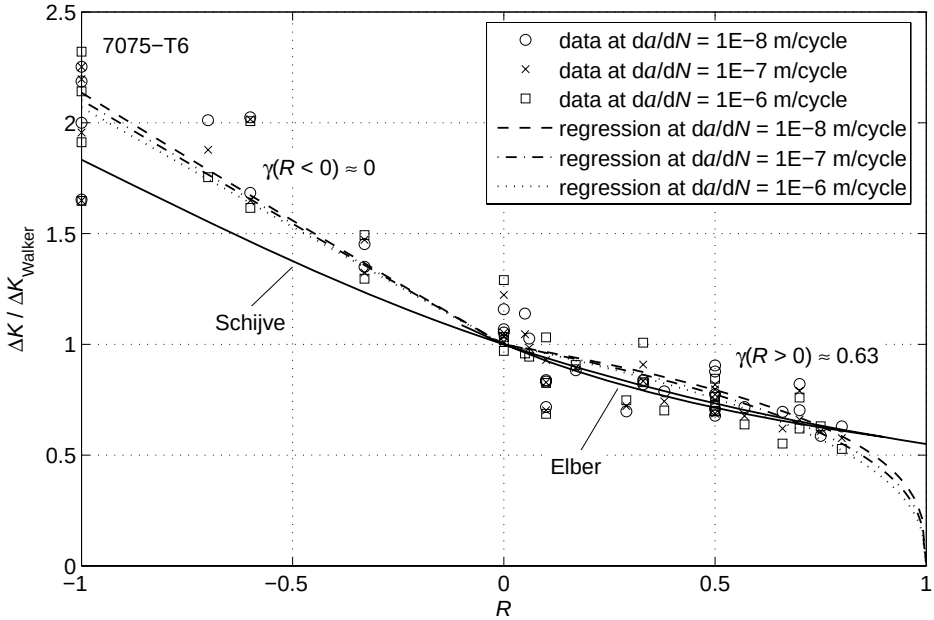

Figure 3.3: $\Delta K/\Delta K_{\text{Walker}}$ as a function of R for the 7075-T6 aluminium alloy using the data in Table 3.1, the Walker curves obtained from linear regression and Elber's and Schijve's equations (see Section 3.2.2).

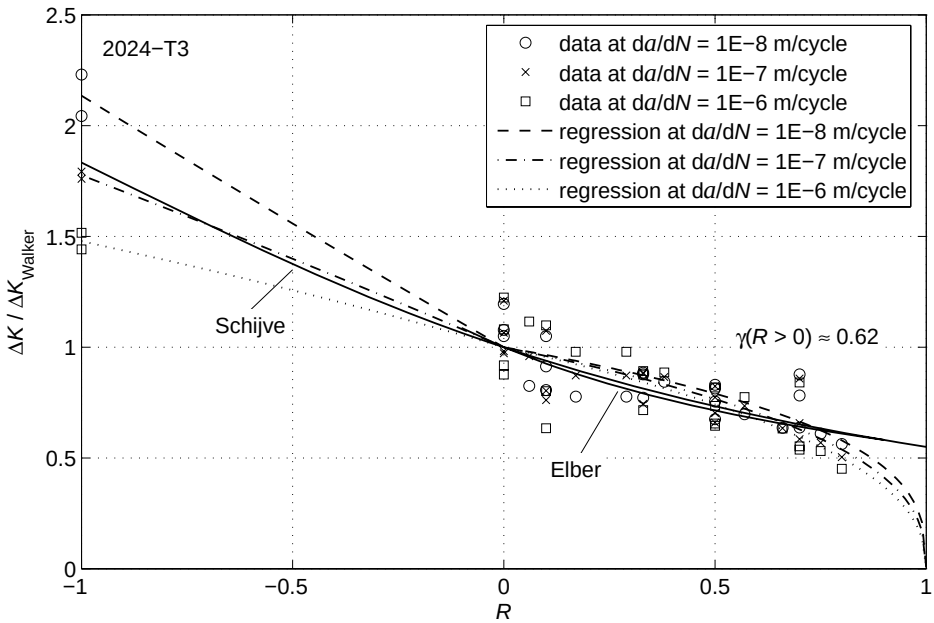

Figure 3.4: $\Delta K/\Delta K_{\text{Walker}}$ as a function of R for the 2024-T3 aluminium alloy using the data in Table 3.1, the Walker curves obtained from linear regression and Elber's and Schijve's equations (see section 3.2.2).

Table 3.2: Predicted Walker exponents for the aluminium alloys 7075-T6 and 2024-T3.

$\mathrm{d}a/\mathrm{d}N$	7075-T6		2024-T3	
[m/cycle]	$\gamma(R \leq 0)$	$\gamma(R \geq 0)$	$\gamma(R \leq 0)$	$\gamma(R \geq 0)$
1×10^{-8}	-0.07	0.66	-0.07	0.66
1×10^{-7}	-0.04	0.63	0.18	0.62
1×10^{-6}	-0.02	0.61	0.40	0.57

3.4 A simple physical model of mean stress dependency

As it has been stated before, a closed crack does not propagate. This leaves the question of when a crack is closed. Ideally this is the case during the compressive part of the load cycle, hence crack closure would occur at $R < 0$. However, the real behaviour is more complicated. Due to surface roughness (mismatch), environmental effects, e.g., oxidation, and the thickening behind the crack front caused by plastic deformation, cracks may close at $R > 0$. A common definition of an effective stress intensity factor range is

$$\Delta K_{\text{eff}} = K_{\text{max}} - K_{\text{op}} \,, \tag{3.15}$$

where K_{op} is the stress intensity factor at which the crack opens. K_{op} is usually positive, but may also be negative. The common ratio between the effective and applied stress intensity factor range is usually denoted by U and defined as

$$U = \frac{\Delta K_{\text{eff}}}{\Delta K} \,. \tag{3.16}$$

Assuming the crack to be either open throughout or closed during a part of the load cycle, ΔK_{eff} can be written as

$$\Delta K_{\text{eff}} = \begin{cases} K_{\text{max}} - K_{\text{op}} \,, & \text{if } K_{\text{min}} \leq K_{\text{op}} \\ K_{\text{max}} - K_{\text{min}} = \Delta K \,, & \text{if } K_{\text{min}} \geq K_{\text{op}} \,. \end{cases} \tag{3.17}$$

Denoting the stress ratio at which the crack starts to remain open throughout the load cycle by R_{eff}, the first line of Eq. 3.17 can be written as

$$\Delta K_{\text{eff}} = K_{\text{max}} - K_{\text{op}} = \frac{\Delta K}{1-R} - K_{\text{op}} = \frac{\Delta K_{\text{eff}}}{1-R_{\text{eff}}} - K_{\text{op}} \,, \tag{3.18}$$

leading to

$$\Delta K_{\text{eff}} = \frac{1-R_{\text{eff}}}{1-R} \Delta K \,. \tag{3.19}$$

It must be noted that the above requires K_{op} not to be a function of R, a requirement which is not fulfilled if, for example, Elber's equation applies. Including the

region with $R \geq R_{\text{eff}}$ gives

$$\Delta K_{\text{eff}} = \begin{cases} \dfrac{1 - R_{\text{eff}}}{1 - R} \Delta K\,, & \text{if } R \leq R_{\text{eff}} \\ \Delta K\,, & \text{if } R \geq R_{\text{eff}}\,, \end{cases} \tag{3.20}$$

which is similar to Walker's equation with $\gamma = 0$ and $\gamma = 1$ for $R \leq R_{\text{eff}}$ and $R \geq R_{\text{eff}}$, respectively. In contrast to Walker's original approach, γ changes not at $R = 0$, but at $R = R_{\text{eff}}$. The second line of the above equation indicates that the crack propagates independently of R if $R \geq R_{\text{eff}}$. Figure 3.5 schematically illustrates Eq. 3.20 using $R_{\text{eff}} = 0.4$ and compares it with Walker's equation.

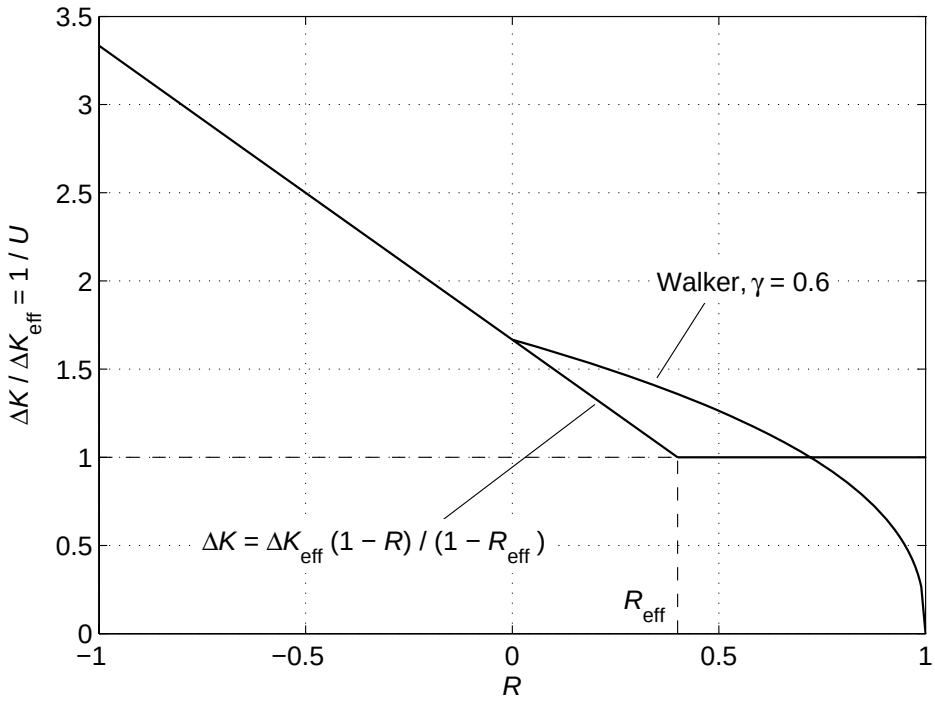

Figure 3.5: $\Delta K/\Delta K_{\text{eff}}$ as a function of R given by Eq. 3.20 ($R_{\text{eff}} = 0.4$) compared with Walker's equation.

Comparing Fig. 3.5 with Fig. 3.2 it is seen that the behaviour described by Eq. 3.20 is partly a reminder of both Elber's and Schijve's equations. As for Walker's approach, two relations are required to describe the stress ratio range from -1 to 1. In addition, R_{eff} must be known.

3.4.1 Application to 7075-T6 aluminium alloy da/dN data

In order to explore how well this model fits actual data, it has been used together with the 7075-T6 aluminium alloy crack propagation data given in Table 3.1. The results are plotted in Fig. 3.6.

It is seen that Eq. 3.20 with $R_{\text{eff}} = 0.3$ nicely fits the experimental data up to $R \approx 0.7$. At higher R ratios the model deviates from the experimental data. It must be mentioned that, although Eq. 3.20 is closely related to Walker's approach,

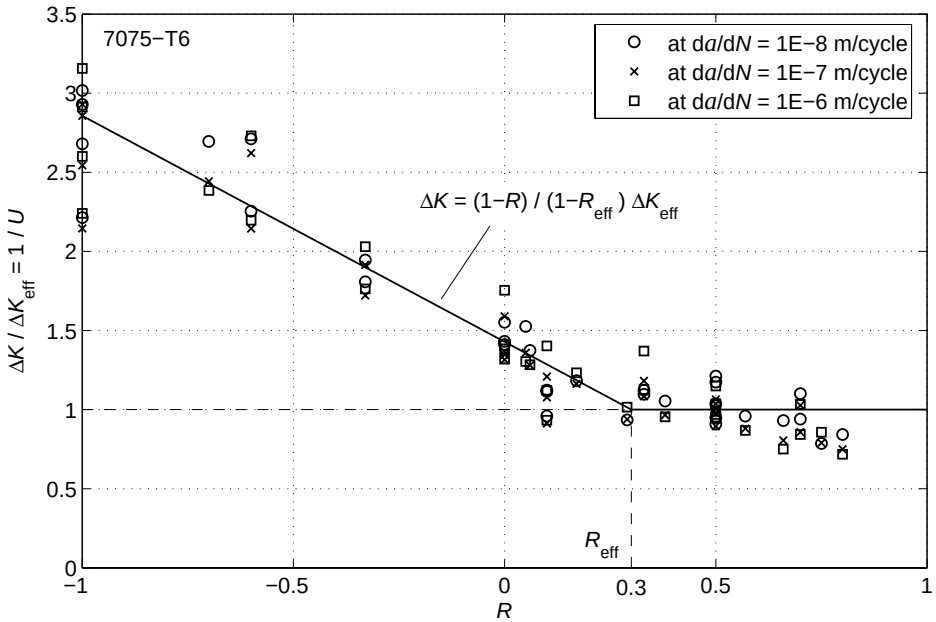

Figure 3.6: $\Delta K/\Delta K_{\text{eff}}$ as a function of R for the 7075-T6 aluminium alloy using the data in Table 3.1 and the fitted Eq. 3.20 ($R_{\text{eff}} = 0.3$, $\Delta K_{\text{eff}}(\mathrm{d}a/\mathrm{d}N = 10^{-8}$, 10^{-7} and 10^{-6} m/cycle) = 3.5, 7 and 13 MPa$\sqrt{\text{m}}$).

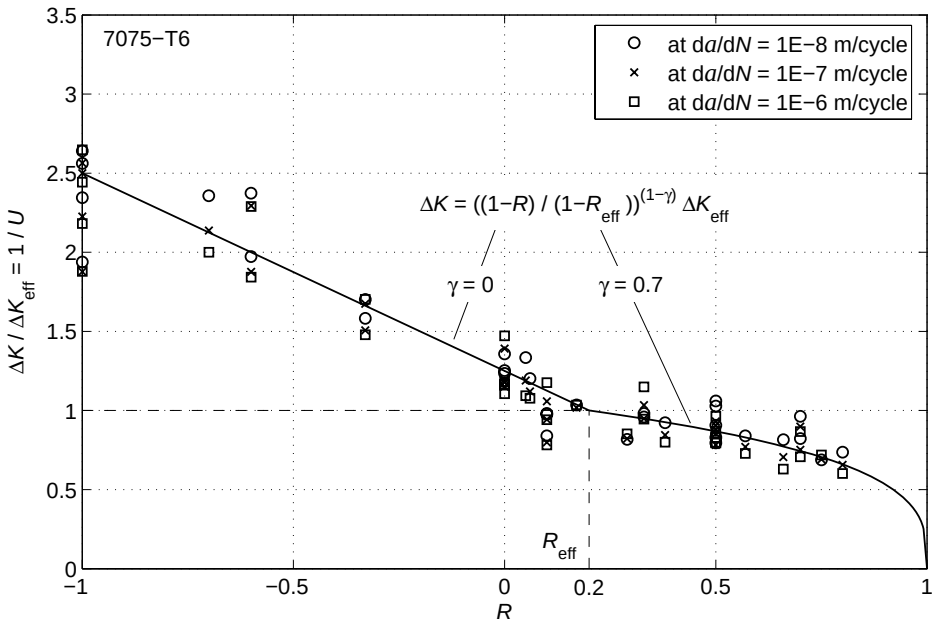

Figure 3.7: $\Delta K/\Delta K_{\text{eff}}$ as a function of R for the 7075-T6 aluminium alloy using the data in Table 3.1 and the fitted Eq. 3.21 ($R_{\text{eff}} = 0.2$, $\Delta K_{\text{eff}}(\mathrm{d}a/\mathrm{d}N = 10^{-8}$, 10^{-7} and 10^{-6} m/cycle) = 4, 8 and 15.5 MPa$\sqrt{\text{m}}$).

the curve fitting method described in Appendix A.3 does not apply. This is due to the additional unknown R_{eff}. Of course, choosing a value for R_{eff}, the two lines can simply be fitted using a slightly modified version (constant slopes, intersection at R_{eff}) of the least mean squares method given in Appendix A.3. It is certainly possible to develop an iterative approach where R_{eff} can be treated as a variable as well, which, however, was not considered in this work. $R_{\text{eff}} = 0.3$ was chosen to visually fit the data in Fig. 3.6 by normalising with $\Delta K_{\text{eff}}(\mathrm{d}a/\mathrm{d}N = 10^{-8}$, 10^{-7} and 10^{-6} m/cycle) = 3.5, 7 and 13 MPa$\sqrt{\text{m}}$.

Examining the data points at $R > R_{\text{eff}}$, they would better fit to a Walker type equation with $\gamma < 1$. This would result in the following modification to Eq. 3.20:

$$\Delta K_{\text{eff}} = \begin{cases} \dfrac{1-R_{\text{eff}}}{1-R}\Delta K\,, & \text{if } R \le R_{\text{eff}} \\ \left(\dfrac{1-R_{\text{eff}}}{1-R}\right)^{1-\gamma}\Delta K\,, & \text{if } R \ge R_{\text{eff}}\,, \end{cases} \tag{3.21}$$

Fig. 3.7, where $R_{\text{eff}} = 0.2$ and $\gamma = 0.8$ were used, shows a very good correspondence between the data and the model. The data were normalised using $\Delta K_{\text{eff}}(\mathrm{d}a/\mathrm{d}N = 10^{-8}$, 10^{-7} and 10^{-6} m/cycle) = 4, 8 and 15.5 MPa$\sqrt{\text{m}}$.

In a final attempt, Eq. 3.21 can be made even more flexible introducing the exponent $\gamma_1 = \gamma(R \le R_{\text{eff}}) \neq 0$:

$$\Delta K_{\text{eff}} = \begin{cases} \left(\dfrac{1-R_{\text{eff}}}{1-R}\right)^{1-\gamma_1}\Delta K\,, & \text{if } R \le R_{\text{eff}} \\ \left(\dfrac{1-R_{\text{eff}}}{1-R}\right)^{1-\gamma}\Delta K\,, & \text{if } R \ge R_{\text{eff}}\,, \end{cases} \tag{3.22}$$

Setting $R_{\text{eff}} = 0$, Eq. 3.22 transforms into Walker's equation. Eq. 3.22 has the benefit of being more flexible compared to Walker's equation, however, this is at the cost of another parameter, R_{eff}.

3.4.2 Application to 5083-H321 aluminium alloy ΔK_{th} data

Recently, Kranenburg et al. [92] carried out fatigue crack propagation threshold tests on the 5083-H321 aluminium alloy. They generated and compared ΔK_{th} data testing at constant R (ASTM E647) and constant K_{max}. Since ΔK_{th} from the constant K_{max} method are given at $R = 0.8$, 0.86, and 0.93 only, the following examination is confined to the constant R data. Figure 3.8b shows both, experimental data and the fitted Eq. 3.20, with $R_{\text{eff}} = 0.42$ and $\Delta K_{\text{eff,th}} = 1.3$ MPa$\sqrt{\text{m}}$. It must be noted that $R_{\text{eff}} = 0.42$ was chosen to fit the data points at low R best, whereas the data rather indicate $R_{\text{eff}} = 0.6$.

It is seen that the transition from partly open to fully open behaviour is smooth rather than sharp. Therefore, Eq. 3.20 does not fit the data at $R = 0.4$ and 0.5 very well. However, above $R \approx 0.5$ and below $R \approx 0.3$ good agreement is obtained.

If a fatigue crack propagation threshold exists, it should be independent of R and the measured dependency on R must be a result of crack closure, hence $\Delta K_{\text{eff,th}}$ should be constant. This allows to plot $U = \Delta K_{\text{eff,th}}/\Delta K_{\text{th}}$,

with $\Delta K_{\mathrm{eff,th}} = 1.3$ MPa$\sqrt{\mathrm{m}}$, versus R, see Fig. 3.8a. It can be seen that the data points at $R \leq 0.6$ follow a straight line nicely. Fitting a linear equation (Elber's equation) to those data points using the least mean squares method, $U = 0.59 + 0.69R$ is found, which is included in Figs. 3.8a and b. The very good agreement is obvious. However, it can be expected that Elber's line rapidly deviates from experimental data at negative stress ratios. Above $R = 0.6$ Elber's equation does not apply, since the crack is fully open.

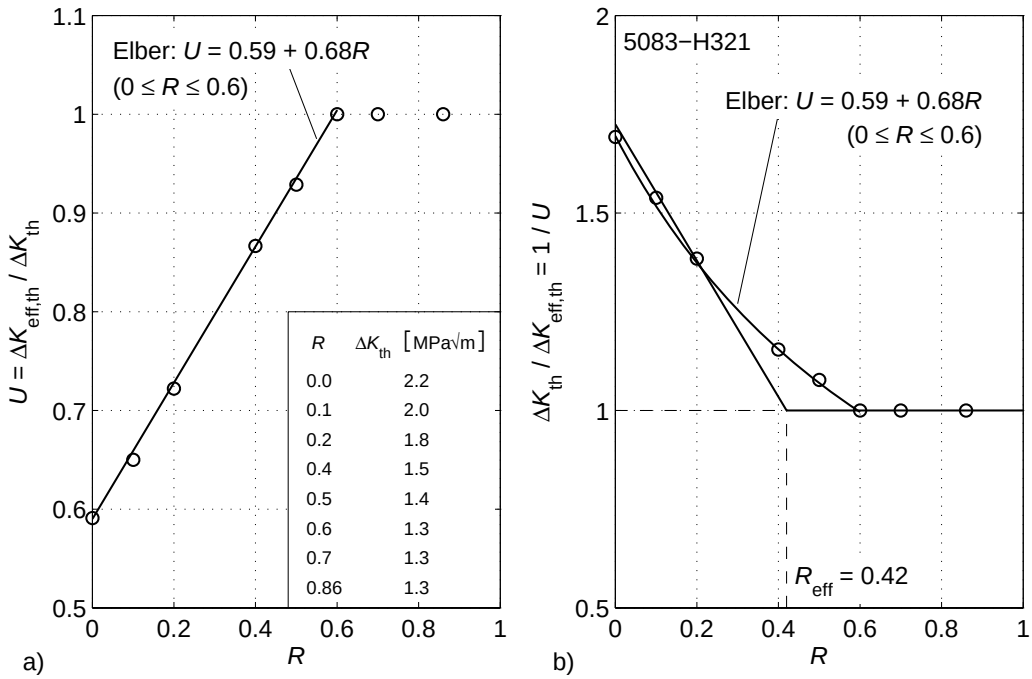

Figure 3.8: (a) U as a function of R for the 5083-H321 aluminium alloy using the experimental data from [92] and Elber's equation fitted to the data points excluding the values at $R = 0.7$ and 0.86, (b) $\Delta K_{\mathrm{th}}/\Delta K_{\mathrm{eff,th}}$ as a function of R, the fitted Eq. 3.20 ($R_{\mathrm{eff}} = 0.42$, $\Delta K_{\mathrm{eff,th}} = 1.3$ MPa$\sqrt{\mathrm{m}}$) and Elber's equation fitted to the data points excluding the values at $R = 0.7$ and 0.86.

3.5 A new mean stress equation

It has been shown in Section 3.3.3 how Walker's equation can be fitted to crack propagation data. However, the distinct change of γ at $R = 0$, which is somewhat arbitrary, is a weakness. This weakness is eliminated with the approach described in Section 3.4, but at the cost of having an additional variable. Still, as it is the case for Walker's equation, two line segments are required to cover the stress ratio range $-1 \leq R < 1$, which is not a convenient feature.

Both, Elber's and Schijve's equations fit the experimental 2024-T3 aluminium alloy data very well, which is not very surprising, since they were proposed for this alloy. Elber's equation covers $-0.1 \leq R \leq 0.7$ only. Therefore, the author was tempted to propose another equation to express the mean stress dependency. Re-plotting the data in Fig. 3.3 using a logarithmic ordinate gives the diagram in

Fig 3.9. It is seen that the data points at each da/dN level fit nicely to a straight

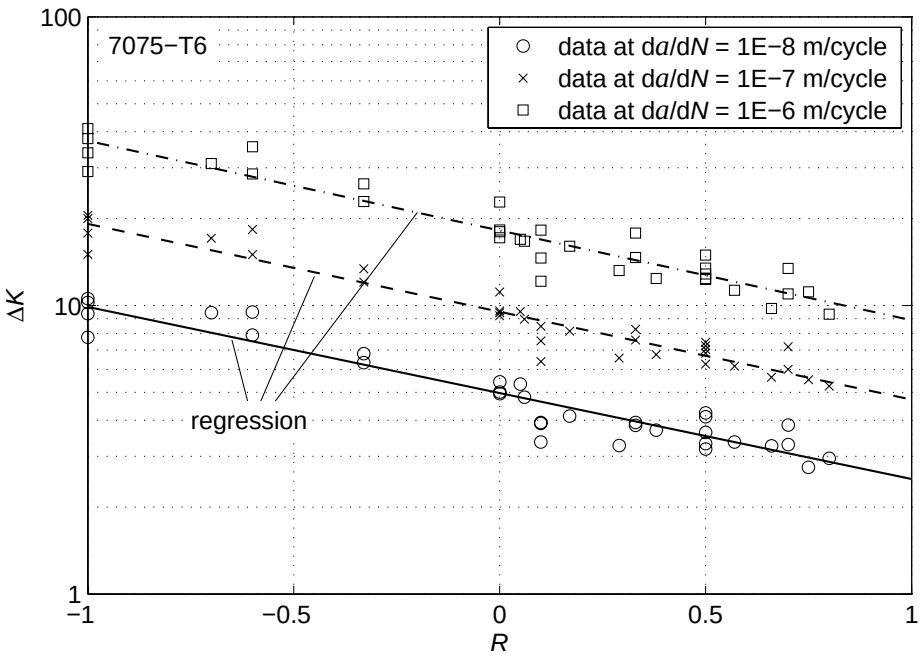

Figure 3.9: ΔK as a function of R for the 7075-T6 aluminium alloy using the data in Table 3.1 and the fitted Eq. 3.23.

line, which can be expressed as:

$$\log \Delta K = \log \Delta K^* - \beta R\,, \tag{3.23}$$

where $\Delta K^* = \Delta K(R = 0)$. Equation 3.23 may be transformed to a form similar to Walker's equation when expressing ΔK^* as a function of R:

$$\Delta K^* = 10^{\beta R} \Delta K\,. \tag{3.24}$$

Using the least mean squares method to fit Eq. 3.23 to the crack propagation data for the aluminium alloys 7075-T6 and 2024-T3, the constants in Table 3.3 are found. The β values for 7075-T6 are 0.3, whereas β for 2024-T3 varies from 0.25 to 0.29. The variation for 2024-T3 is mainly due to the few data points below $R = 0$. The results are visualised in Fig. 3.9 and Fig. 3.10.

Normalising ΔK with ΔK^*, only done here for the 7075-T6 aluminium alloy, Fig. 3.11 is obtained, where a linear ordinate is used. In this normalised form the data points collapse to a single line. Since $\beta = 0.3$ at all three da/dN levels, see Table 3.3, Eq. 3.24 gives the same line in Fig. 3.11 for each set of data points.

Contrary to Walker's equation, $\Delta K/\Delta K^*$ in the proposed equation does not reach zero when R approaches 1. The same thing occurs in Elber's and Schijve's equations. Below $R = -1$, Eq. 3.24 may deviate from the experimental data. However, due to the lack of data, this could not be checked. Taking the relatively large scatter in data into account, a β value of 0.3 for both alloys would be a realistic assumption. Equation 3.24 provides a good approximation of the stress ratio dependency of crack propagation data and the single parameter β can easily be found from usual da/dN data.

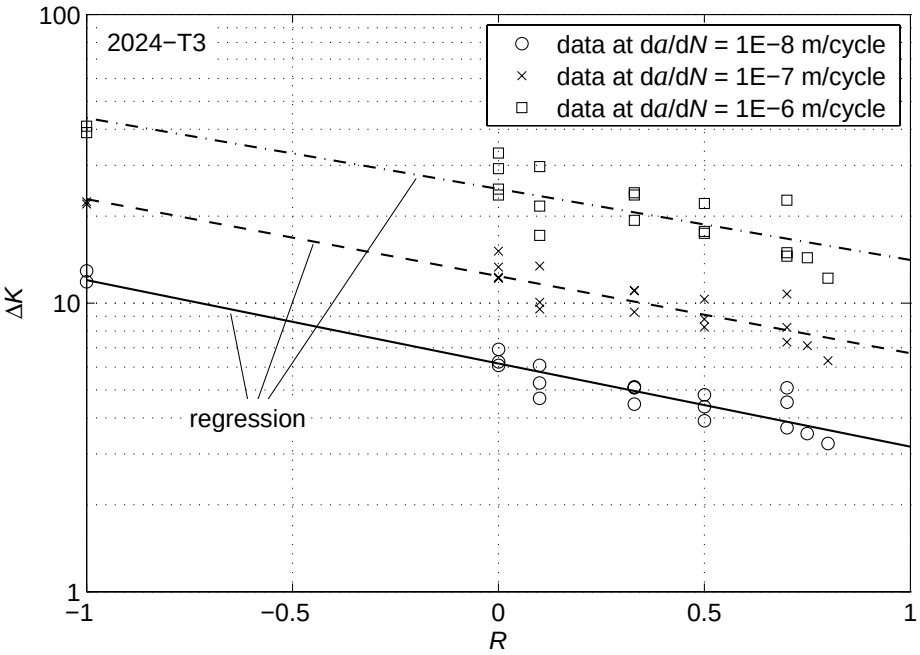

Figure 3.10: ΔK as a function of R for the 2024-T3 aluminium alloy using the data in Table 3.1 and the fitted Eq. 3.23.

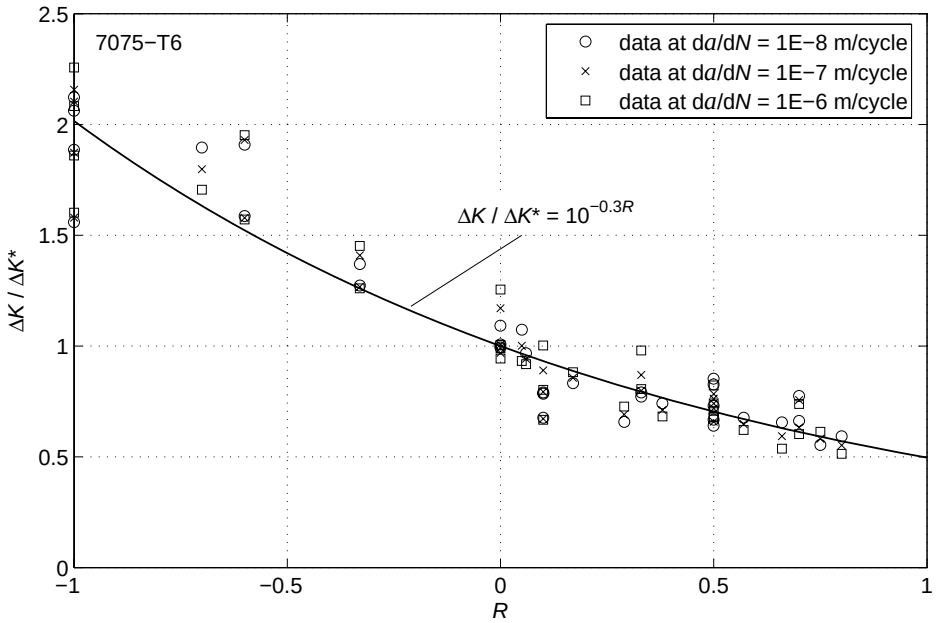

Figure 3.11: $\Delta K/\Delta K^*$ as a function of R for the 7075-T6 aluminium alloy using the data in Table 3.1 and the fitted Eq. 3.23.

Table 3.3: Predicted constants in Eq. 3.23 for the aluminium alloys 7075-T6 and 2024-T3.

	7075-T6		2024-T3	
$\mathrm{d}a/\mathrm{d}N$ [m/cycle]	ΔK^* [MPa$\sqrt{m}$]	β	ΔK^* [MPa$\sqrt{m}$]	β
1×10^{-8}	5.0	0.30	6.0	0.29
1×10^{-7}	9.5	0.30	12.5	0.26
1×10^{-6}	18.2	0.31	25.8	0.24

3.6 Remarks

In the previous sections, a number of equations to account for the dependency of crack propagation data on mean stress has been discussed, and compared to the experimental data. Since this investigation is only carried out for two aluminium alloys it is certainly not generally applicable. However, it may give an indication of the advantages and drawbacks in the different methods.

None of the methods seem much superior to the others, especially when bearing in mind the relatively large scatter in data. Within that scatter they will all yield reasonable results.

Walker's approach and the one suggested in Section 3.4 require two lines to describe either side of $R = 0$ or $R = R_{\text{eff}}$, respectively. The distinct change in behaviour at $R = 0$ or $R = R_{\text{eff}}$ gives the approaches a partly physical basis. On the other hand, comparison with experimental data reveals that the real behaviour is more complicated. The approach described in Section 3.4, especially with $\gamma < 1$ for $R > R_{\text{eff}}$, yields very good agreement with experimental data. However, due to the extra variable R_{eff}, data fitting is not trivial. Being forced to handle two equations may prove inconvenient if the crack propagation data stress ratio and the load stress ratio do not fall on the same line.

Crack propagation threshold data seem to own a constant $\Delta K_{\text{eff,th}}$, hence, if known, Elber's equation can be fitted easily and yields very good agreement, when the closure free data are excluded.

The new mean stress equation proposed in Section 3.5 combines simplicity, easy adaption to crack propagation data and covers the range $-1 \leq R \leq 1$ with a single expression.

CHAPTER 4

Short crack growth testing

The welded T-joints which will be investigated in Chapters 5 and 6 are made from the aluminium alloy 6082-T6. Little published crack propagation data are available for this alloy. Published crack propagation data are mostly generated with specimens containing a deep (long) crack, whereas many cracks in real structures are rather short. In addition, no Walker exponent for this alloy was available. Therefore this chapter has the following objectives. First, fatigue crack propagation tests were carried out to determine whether there is a significant difference in the behaviour of short and long cracks, and to see if using the characteristic crack length, a^*, is an appropriate means of dealing with the probable differences. The second objective was to produce additional crack propagation data for the aluminium alloy under investigation and the third was to investigate the mean stress dependency of the 6082-T6 aluminium alloy.

This work was focused on sub-millimetre cracks which were supposed to propagate in the same material as was used for the T-joints and with a propagation direction perpendicular to the extrusion direction. The most straightforward method to monitor crack growth would be to use a microscope. However, this requires both manual reading and a clearly visible crack tip. A more elegant method for data acquisition is measuring the drop in electrical potential at the propagating crack.

During the planing of the tests, the test equipment required and the available competence in carrying out such testing were thoroughly investigated. Due to the lack of both a resonance test machine to test at high frequencies and the lack of experience in applying the potential drop technique to aluminium in the department's own workshop (potential changes with nanovolt magnitude must be measured) it was decided to use an external laboratory. The raw data produced by the laboratory were processed and evaluated in parallel to the tests and feedback was given to the laboratory in order to adjust the test parameters for each new specimen.

4.1 Test specimens and measurement technique

4.1.1 The test specimens

The test specimen geometry chosen was a single edge notch tension (SENT) specimen, see Fig. 4.1, which fitted the existing clamping equipment and the available material best.

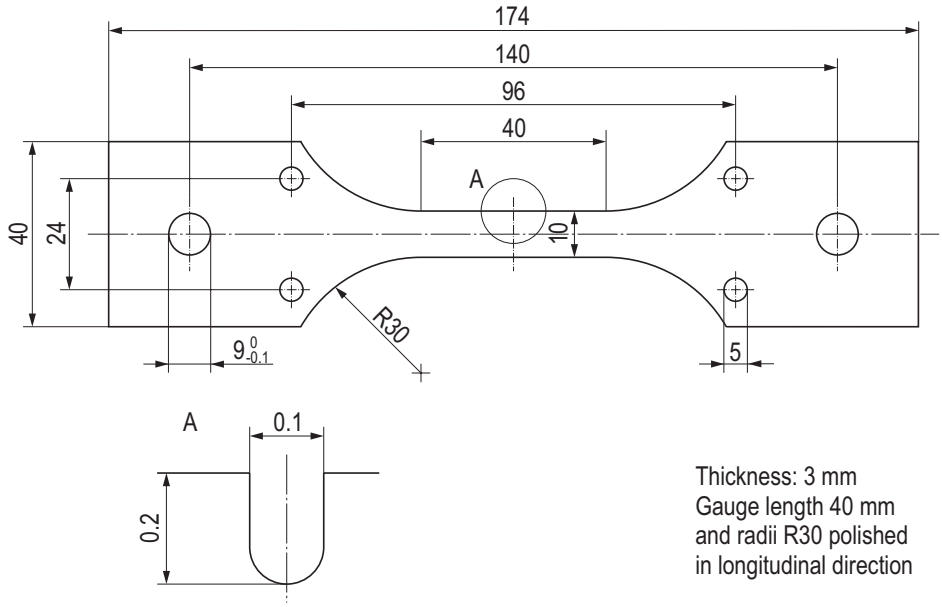

Figure 4.1: Geometry of the short crack growth test specimens including the geometry of the starter notch.

The specimens were machined from the same 6082-T6 aluminium RHS profiles as used in the T-joints. Both the machining and the polishing were carried out in the department's own workshop. The specimen thickness varied between 2.8 mm and 3.2 mm, which was due to the variations in the wall thickness of the RHS profiles.

A specialized company in Switzerland spark eroded the tiny starter notch (U-notch, 0.2 mm deep and 0.1 mm wide, cf. Fig. 4.1). In addition, two shallow grooves (0.06 mm deep and 0.1 mm wide) were eroded on each side of the starter notch. These grooves were 2 mm away from the starter notch and were used to position the potential drop probes accurately.

4.1.2 Test conditions and potential drop technique

A resonance test machine was used to carry out the crack propagation tests. The test frequency was 100 Hz and the specimens were subjected to a direct current (DC) of 15 A for the potential drop measurements. Figure 4.2 shows a specimen fixed with two bolts to the insulated clamping system, the current wires and two microscopes. Figure 4.3 shows a close-up of specimen 3 with the starter notch and the attached potential drop probes. Eight specimens were tested successfully at four different stress ratios, cf. Table 4.1.

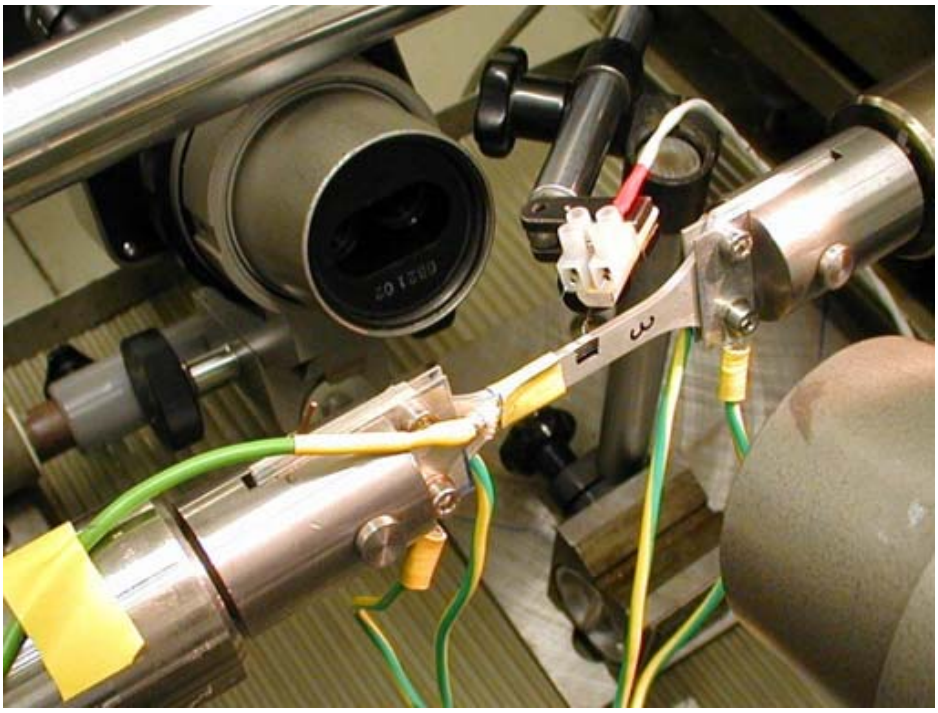

Figure 4.2: Specimen 3 in the resonance testing machine.

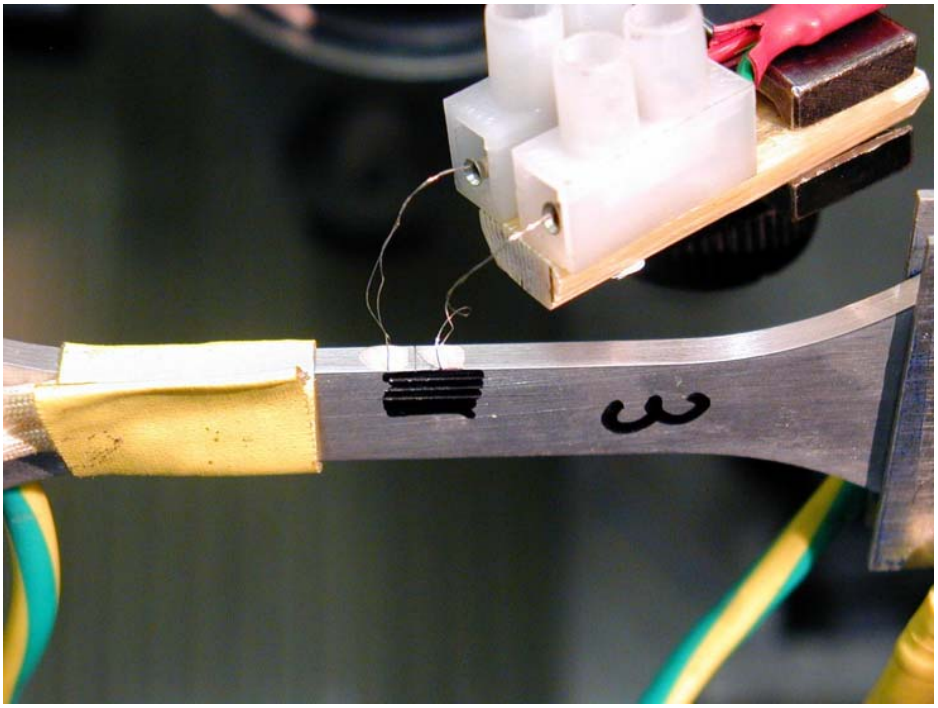

Figure 4.3: A close up of specimen 3 showing the starter notch and the attached potential drop probes.

To compensate for the change of the electrical resistance of the specimen due to temperature changes, the temperature of the specimen was measured with a thermocouple, which was kept in place by the yellow tape seen in Fig. 4.3. A computer program collected the electrical potential drop change, the temperature and the elapsed number of cycles. The program automatically compensated for temperature changes.

Since the measured voltage is of the order of μV and changes in crack depth result in voltage changes with nV magnitude, high and precise amplification is required. Therefore, a high quality tailor-made pre-amplifier was used to amplify the temperature signal and the voltage change by a factor 2000.

A special DC potential drop technique was used, where the current is pulsed and the current flow is reversed with each successive pulse, see Fig. 4.4 [93]. To make sure that each measurement is made at the highest load, multiple measurements were made near each peak. In addition, the voltage drop is averaged over the time of one current pulse, t_p, cf. Fig. 4.4. The total voltage drop is then found from the difference between two successive current pulses.

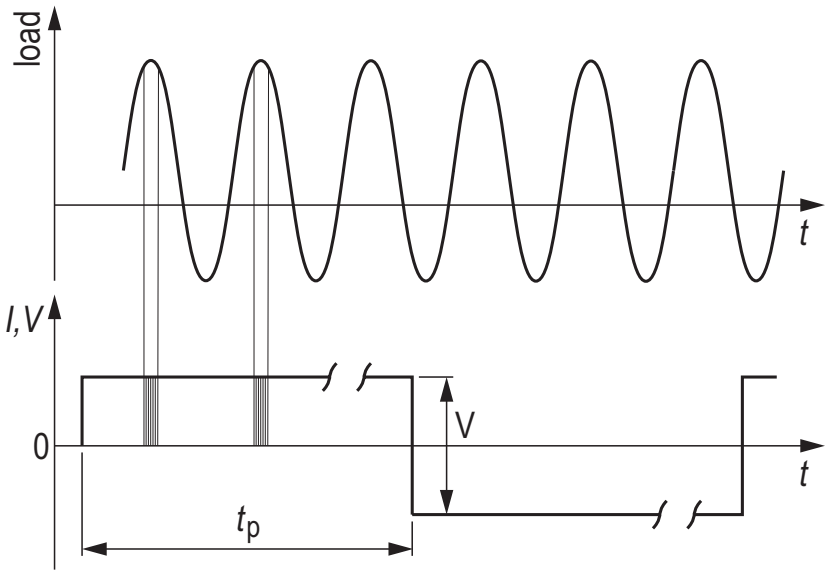

Figure 4.4: Potential drop technique with pulsed direct current.

As a means of quality control it was planned to measure the crack depth optically employing the two microscopes seen in Fig. 4.2. Some specimens were therefore equipped with a very fine grid ahead of the starter notch. This grid was generated photographically [94]. However, since it was extremely difficult to accurately locate the crack tip, these measurements were eventually suspended.

4.2 Some pre-test evaluations

The measurements had to be started close to the threshold region, since the main difference in the crack propagation rate between short and long cracks is supposed to be in this region. Therefore, some calculations were carried out to estimate an appropriate load level.

4.2.1 Fatigue limit of notched specimen

The loading must exceed the fatigue limit of the notched specimen to initiate a crack at the starter notch. From $R_\mathrm{m} = 300$ MPa, the fatigue limit of a smooth specimen is estimated to $\sigma_\mathrm{A}(R = -1) = 120$ MPa. Converting to $R = 0.1$ using Walker's equation with $\gamma_\mathrm{A} = 0.5$ gives $\sigma_\mathrm{A}(R = 0.1) = 80$ MPa.

Using different assumptions, the stress concentration factor at the starter notch can be calculated to:

$$K_\mathrm{t} = \begin{cases} 1 + 2\sqrt{d/\rho} = 5 & \text{, elliptical hole, infinite plate,} \\ 5.6 & \text{, } \textit{Dubbel} \text{ [44], U-notch, semi-infinite plate,} \\ 5.3 & \text{, FE analysis, U-notch.} \end{cases} \tag{4.1}$$

The three values are almost identical and $K_\mathrm{t} = 5.3$ is used in the further calculations. Estimating the fatigue notch factor with the three approaches described in Section 2.5.2 gives:

$$\begin{aligned} &\text{Peterson:} && K_\mathrm{f} = 1 + \frac{K_\mathrm{t} - 1}{1 + \rho_0/\rho} = \{\rho_0 = 0.64 \text{ mm}\} = 1.3 \\ &\text{Neuber:} && K_\mathrm{f} = 1 + \frac{K_\mathrm{t} - 1}{1 + \sqrt{2\rho^*/\rho}} = \{\rho^* = 0.2 \text{ mm}\} = 2.1 \\ &\text{Gradient:} && \chi = \frac{1}{5.3}\frac{5.3 - 4.3}{(4.8 - 4.7954) \text{ mm}} = 41 \text{ mm}^{-1} \\ & && K_\mathrm{f} = \frac{K_\mathrm{t}}{1 + \sqrt{\rho_\mathrm{o}\chi}} = \{\rho_\mathrm{o} = 0.075 \text{ mm}\} = 1.9\,. \end{aligned}$$

Finally, assuming $K_\mathrm{f} \approx 2$, the fatigue limit of the SENT specimen is found to:

$$S_\mathrm{A,notch}(R = 0.1) = \frac{\sigma_\mathrm{A}}{K_\mathrm{f}} = 40 \text{ MPa}\,. \tag{4.2}$$

4.2.2 Fatigue limit of cracked specimen

Whether a crack that has been initiated can grow or not is determined by the threshold stress intensity factor range, ΔK_th. Assuming the total crack depth to be just slightly larger than the depth of the starter notch, for example $a = 0.21$ mm, and using $\Delta K_\mathrm{th}(R = 0.1) = 3$ MPa$\sqrt{\mathrm{m}}$, the stress range becomes

$$\Delta S(R = 0.1) = \frac{\Delta K_\mathrm{th}}{1.12\sqrt{\pi a}} = 104 \text{ MPa}\,. \tag{4.3}$$

Hence, conservatively assuming that the crack has grown out of the notch stress field already, $S_\mathrm{a} \geq 52$ MPa is required to propagate the crack.

The estimates from Eqs. 4.2 and 4.3 are relative close to each other. During the experiments, however, it was found that a crack started to propagate at even lower stress amplitudes and the stress amplitude required to start crack propagation varied to some extent from specimen to specimen.

4.3 Correlating potential drop and crack depth

Subjecting the specimen to an electric current, which of course requires electrically insulated clamping, a potential drop can be measured between any two points (probes) that are a distance apart in the direction of the current flow. If there is a crack between the probes, the potential drop will increase as the crack propagates. A calibration curve or function is required to relate the measured potential drop change to the change in crack depth.

4.3.1 Edge crack in a semi-infinite plate

According to Dobmann et al. [95] the electrical potential drop over an edge crack in a semi-infinite plate is given by

$$\frac{V}{V^*} = \sqrt{1 + \left(\frac{d+a}{y}\right)^2}\,, \tag{4.4}$$

where V^* is the electrical potential drop measured in a smooth specimen, $d+a = 0$, and y is the distance between the probes and the crack, see Fig. 4.5. Since the

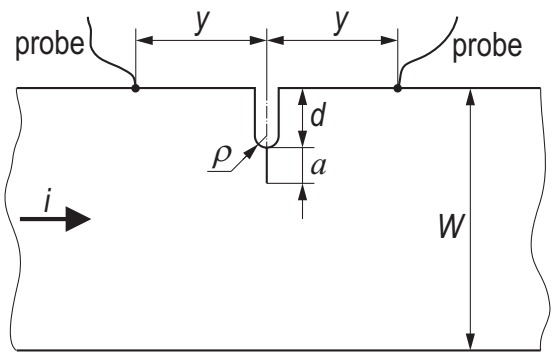

Figure 4.5: Potential drop measuring principle and nomenclature.

specimens tested here contain a starter notch, it is more convenient to transform Eq. 4.4 such that it is normalised with $V_0 = V(d)$:

$$\frac{V}{V_0} = \sqrt{\frac{1 + \left(\frac{d+a}{y}\right)^2}{1 + \left(\frac{d}{y}\right)^2}}\,. \tag{4.5}$$

Introducing the relative potential drop change, u, Eq. 4.5 becomes:

$$u = \frac{V - V_0}{V_0} = \sqrt{\frac{1 + \left(\frac{d+a}{y}\right)^2}{1 + \left(\frac{d}{y}\right)^2}} - 1\,. \tag{4.6}$$

Finally, rewriting Eq. 4.6, the crack depth can be expressed as a function of u:

$$a = y\sqrt{(u+1)^2\left[1+\left(\frac{d}{y}\right)^2\right]-1} \quad -d\,. \tag{4.7}$$

4.3.2 Edge crack in a finite plate

As long as $a \ll W$ the above equations hold true in a finite plate, too. When the crack becomes deeper, i.e., the finite plate width has to be accounted for, another calibration function, usually known as Johnson's formula [96], must be used:

$$\frac{V}{V^*} = \left(\frac{\pi y}{2W}\right)^{-1} \cosh^{-1}\left[\frac{\cosh\dfrac{\pi y}{2W}}{\cos\dfrac{\pi(d+a)}{2W}}\right]. \tag{4.8}$$

Transforming Eq. 4.8 to make it non-dimensional with respect to V_0, the crack depth is obtained from

$$a = \frac{2W}{\pi}\cos^{-1}\left[\frac{\cosh\dfrac{\pi y}{2W}}{\cosh\left(A(u+1)\right)}\right] - d\,, \tag{4.9}$$

with

$$A = \cosh^{-1}\left[\frac{\cosh\dfrac{\pi y}{2W}}{\cos\dfrac{\pi d}{2W}}\right]. \tag{4.10}$$

4.4 The stress intensity factor

The stress intensity factor must be calculated to express the crack propagation rate, $\mathrm{d}a/\mathrm{d}N$, as a function of ΔK. For an edge crack in a semi-infinite plate the well-known equation

$$\Delta K = 1.12\Delta S\sqrt{\pi a} \tag{4.11}$$

applies. The SENT specimens used here, however, will follow this relation for relatively short cracks ($a/W < 0.1$) only. As the crack grows deeper, two effects are no longer negligible. The first one is the increasing contribution from the bending stress due to the unsymmetric specimen. Secondly, ΔK will increase more rapidly as the crack approaches the opposite specimen surface.

An equation that takes care of both effects can be found in [97] and is written as:

$$\Delta K = \Delta S\sqrt{W}\frac{\sqrt{2\tan\dfrac{\pi a}{2W}}}{\cos\dfrac{\pi a}{2W}}\left[0.752 + 2.02\frac{a}{W} + 0.37\left(1-\sin\frac{\pi a}{2W}\right)^3\right] \tag{4.12}$$

Section 4.5.1 evaluates the impact of using Eq. 4.7 together with Eq. 4.11 versus using Eqs. 4.9 and 4.12.

4.5 Results

According to Section 4.2, a crack should initiate and propagate at $S_a \geq 40$ MPa and employing the threshold stress intensity factor range, an initiated crack would grow at $S_a \geq 52$ MPa. However, the experiments revealed that a propagating crack could be initiated already at stress amplitudes ≈ 30 MPa ($R = 0.1$). One reason for the estimated high stress amplitude required to propagate an initiated crack may be due to the high threshold stress intensity factor range used, which was estimated from crack growth data in Eurocode 9. Borrego et al. [98] suggested $\Delta K_{th} = (2.184 - 1.007R)$ MPa$\sqrt{m}$, hence, $\Delta K_{th}(R = 0.1)$ would be 2.1 MPa$\sqrt{m}$ instead of the 3 MPa$\sqrt{m}$ used here. Furthermore, the notch tip is certainly not perfectly smooth and the spark erosion process may have changed the material properties at the notch tip.

The tests were started at low stress amplitude. When no change in the electrical potential was observed, the load was increased by 5 % every 1 million cycles until a crack had been initiated. This was determined by a relative potential drop change of 0.8 %. Thereafter the load was reduced to obtain reasonable lifetimes. To keep the increase in crack depth during this load reduction period as small as possible, the load had to be reduced quickly. However, this represented some difficulties. Since the stress intensity factor range was very close to the threshold value, too large a reduction in load immediately resulted in crack arrest. Hence, time-consuming manual manipulation was required. Having reached a reasonable stress level, the crack was by that time approximately 0.5 mm deep, the stress was kept constant. The tests were concluded at a crack depth of approximately 3 mm, with some of the specimens having survived more than 30 million cycles. Some specimens could not be used, because they fractured at one of the bolt holes used for the clamping.

During early propagation, the cracks were not through edge cracks, as intended, but were growing from one of the two corners in the starter notch instead. Only after having reached a depth of ≈ 1 mm, the cracks became through edge cracks, which were still not equally deep on both sides of the specimen. A tentative explanation of this behaviour is found in the specimens themselves. After machining the specimens from the hollow section profiles, they were slightly distorted, which was probably caused by released residual stresses. Due to the specimens not being totally flat, out-of-plane bending occurred, which made the loading more severe at one of the corners in the starter notch.

Another observation has been made after finally fracturing the specimens. Inspecting the fracture surfaces, the structure near the specimen surfaces was found to be much coarser than the structure inside the specimen. Figure 4.6 shows a typical fracture surface. The rougher surface structure prevails up to about 1 mm below both surfaces of the specimen. These different zones reflect the grain structure shown in Fig. 5.7. The material structure near the surfaces, which is a result of the extrusion process, probably causes some of the variations in the recorded crack propagation data.

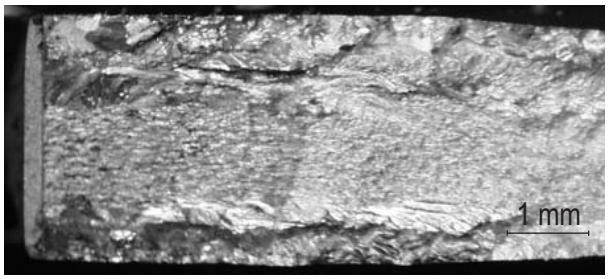

Figure 4.6: Starter notch (left hand side) and a typical fracture surface.

4.5.1 Semi-infinite plate or SENT?

The results from the two assumptions are compared in Fig. 4.7 to find out whether the equations for an edge crack in a semi-infinite plate, Eqs. 4.7 and 4.11, apply, or whether the effects from the finite width and the bending part of the loading must be accounted for, Eqs. 4.9 and 4.12. It is seen that up to a crack length of ≈ 1 mm ($a/W = 0.1$), both assumptions give similar results. For longer cracks the solution for the SENT specimen yields larger stress intensity factor ranges. Since the specimens were tested up to a crack depth of approximately 3 mm, Eqs. 4.9 and 4.12 were used throughout the following investigations.

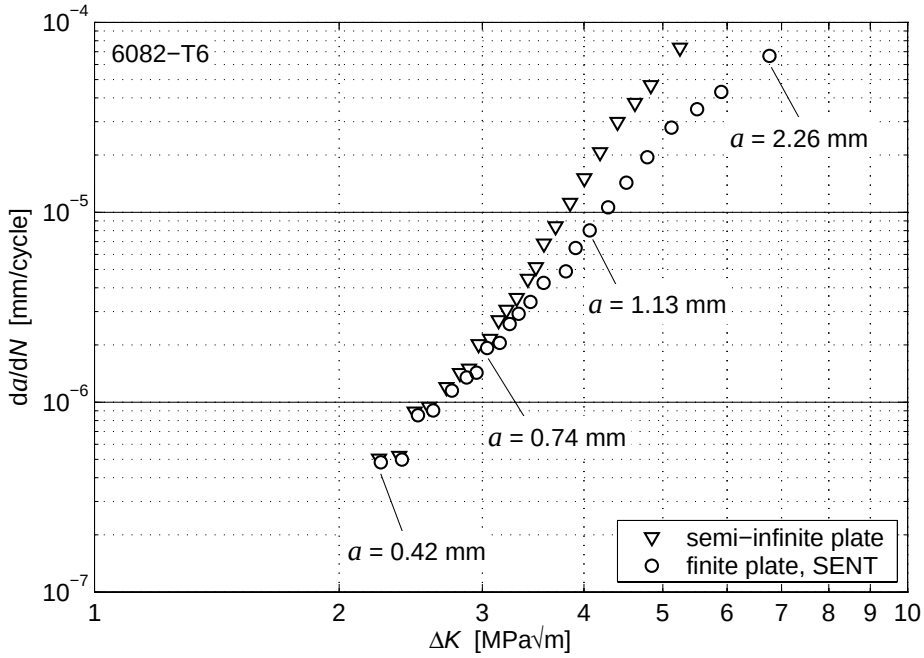

Figure 4.7: Difference between assuming an edge crack in a semi-infinite plate and the same crack in a SENT specimen.

4.5.2 Crack propagation data

As mentioned the output from the potential drop measurements, i.e., the relative potential drop change, u, was transformed to a crack depth by applying Eq. 4.9. Thereafter appropriate intervals, Δa were chosen to calculate $\mathrm{d}a/\mathrm{d}N$. The mean

crack length in each interval was used together with Eq. 4.12 to find ΔK. In Fig. 4.8 the crack propagation data obtained are plotted together with the long crack propagation data given in Eurocode 9. The corresponding Paris constants are listed in Table 4.1.

Comparing the presented results with the curve from Eurocode 9, it is immediately seen that they coincide to a large degree.

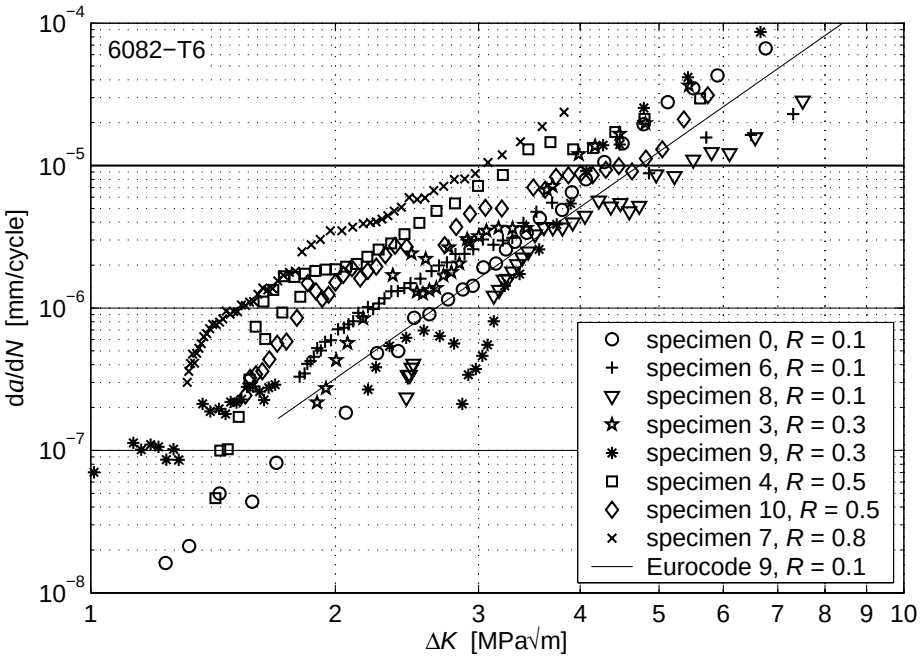

Figure 4.8: Obtained crack propagation data compared to the curve from Eurocode 9.

Especially at lower crack propagation rates the scatter in the experimental results is considerable. Some of the scatter is certainly due to the different grain structures the crack must pass through during propagation. The data from specimen 9 show some crack retardation behaviour at intermediate growth rates, which is probably due to the formation of an oxide layer during a longer stop of the test.

Apart from the results from the specimens 0 and 9, all crack propagation data seem to converge towards some threshold stress intensity factor ranges. These threshold values are close to $\Delta K_{\text{th}} = 2.184 - 1.007R$ [MPa$\sqrt{\text{m}}$] as observed by Borrego et al. [98].

However, the data from the specimens 0 and 9 show no threshold. This indicates some form of short crack growth behaviour, i.e., faster propagation at low ΔK. Actually, the measurements from these specimens could be evaluated starting directly with the initiated crack, i.e., the cracks were ≈ 0.2 mm deep. However, this was the case for the data from specimens 3 and 4 too, and they seem to approach a threshold value.

The limited number of results and the scatter make it difficult to draw conclusive facts regarding the difference in growth behaviour between short and long

Table 4.1: Paris constants calculated from the test data.

Specimen no.	R	C (mm/cycle, MPa$\sqrt{\text{m}}$)	m
0	0.1	6.1×10^{-9}	5.1
6	0.1	5.0×10^{-8}	2.9
8	0.1	1.8×10^{-8}	3.8
3	0.3	3.1×10^{-8}	4.2
9	0.3	—	—
4	0.5	2.5×10^{-7}	2.9
10	0.5	1.4×10^{-7}	3.0
7	0.8	2.5×10^{-7}	3.4

cracks at low ΔK. However, the experimental results clearly justify the usage of the crack propagation data published in Eurocode 9 in the previous two chapters.

The fact that little evidence of short crack growth behaviour was found, is certainly due to the cracks not being short enough.

4.5.3 Mean stress dependency

The crack propagation tests were carried out at four different stress ratios, $R =$ 0.1, 0.3, 0.5 and 0.8, which offers the possibility to evaluate the mean stress dependency of the obtained crack propagation data. Together with the data from Eurocode 9, cf. Table 5.3, and from Borrego et al. [98], see Table 4.2, the obtained data are plotted in a ΔK vs. R plot, see Fig. 4.9.

Table 4.2: 6082-T6 aluminium alloy Paris constants generated by Borrego et al. [98].

No.	R	C (mm/cycle, MPa$\sqrt{\text{m}}$)	m
1	-0.25	1.9×10^{-8}	3.98
2	0.05	5.1×10^{-8}	3.54
3	0.25	8.9×10^{-8}	3.45
4	0.40	1.2×10^{-7}	3.40

Carrying out a linear regression analysis including all data points at positive stress ratios, a Walker exponent of $\gamma = 0.78$ is obtained, which is much larger than the value $\gamma = 0.6$ that has been found suitable for both 7075-T6 and 2024-T3. Apart from the scatter at $R = 0.1$, the data points nicely follow Walker's curve. At negative stress ratios only one data point is given. Hence, no statement about the mean stress dependency in this region can be made, apart from the observation that the data point falls below the line representing $\gamma = 0$.

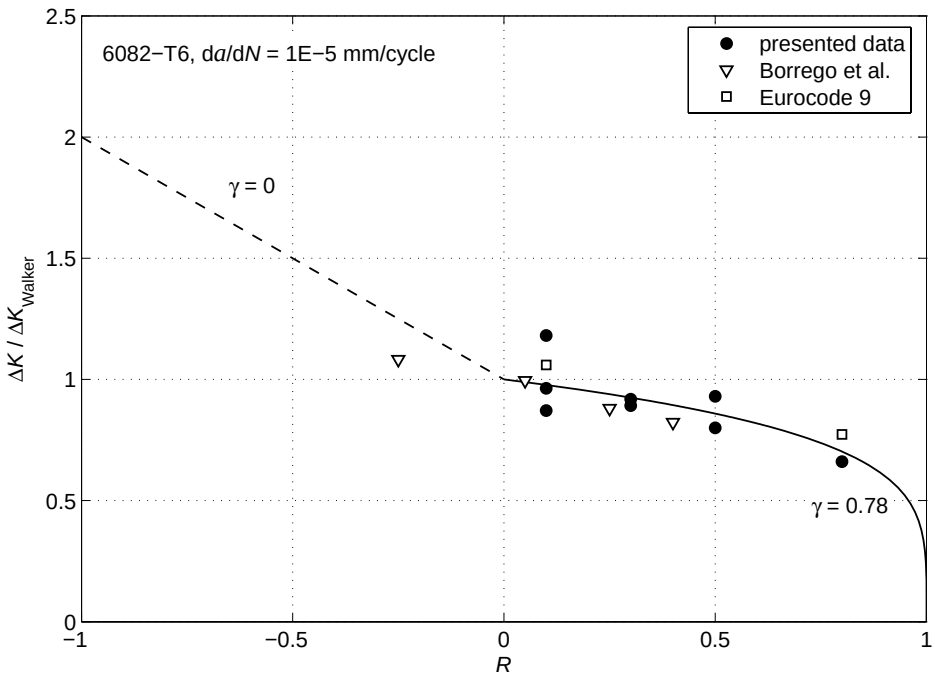

Figure 4.9: $\Delta K/\Delta K_{\text{Walker}}$ as a function of R including the presented data, data from Eurocode 9 (Table 5.3) and Borrego et al. [98] (Table 4.2) compared to Walker's equation.

Applying the mean stress equation presented in Section 3.5, a linear regression analysis gives $\beta = 0.19$. This value is rather low compared to the $\beta = 0.24 \ldots 0.31$ obtained for the 7075-T6 and 2024-T3 aluminium alloys, which is partly due to the low value at $R = -0.25$.

Using Eq. 3.24 with $\beta = 0.19$ (Walker's equation with $\gamma = 0.78$ gives a similar result), the $\mathrm{d}a/\mathrm{d}N$ data collapse into a narrow scatter band, see Fig. 4.11. It is also seen that near the threshold the stress ratio dependency is more pronounced. Specimen 9 has been left out of the diagram shown in Fig. 4.11.

4.6 Remarks and discussion

Crack propagation tests on SENT specimens with sub-millimetre cracks have been carried out. The crack length has been successfully monitored with a special DC potential drop technique. It has been proven that this technique is applicable to aluminium alloys with very short cracks. This is not obvious since aluminium is a very good conductor, which means that very precise measurements are required. Observing the crack propagation optically using microscopes was found to be extremely difficult, if not impossible, since the crack tip was more or less invisible.

Apart from the specimens 0 and 9, no accelerated crack propagation rates for short cracks were found, certainly because the cracks were not short enough. Nevertheless, the data obtained for sub-millimetre cracks validate those given in [5] and [98], which were conducted with much longer cracks. Bearing in mind that the crack growth data has been mainly generated at cracks shorter than

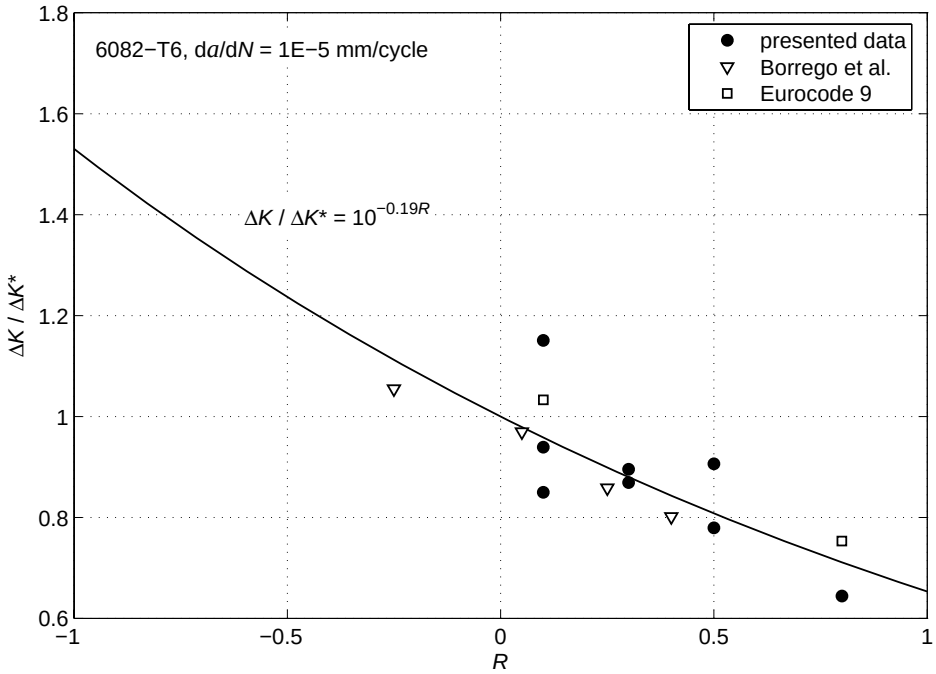

Figure 4.10: $\Delta K/\Delta K^*$ as a function of R including the presented data, data from Eurocode 9 (Table 5.3) and Borrego et al. [98] (Table 4.2) compared to the mean stress equation presented in Section 3.5.

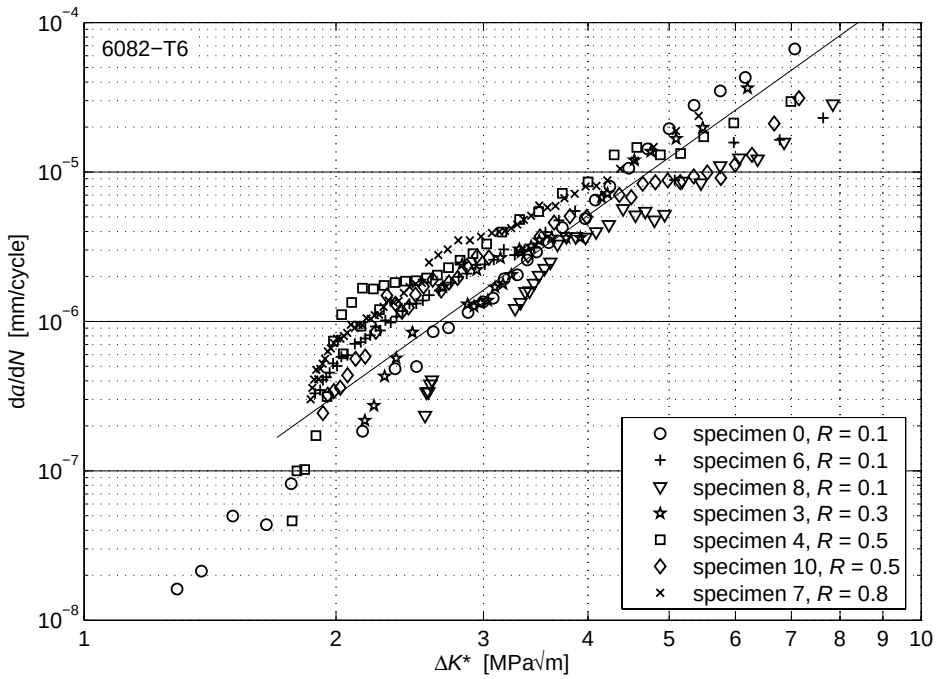

Figure 4.11: $\mathrm{d}a/\mathrm{d}N$ as a function of ΔK^*.

1 mm, the amount of scatter is not unexpected. Some of the scatter is probably due to the interaction between the crack and the different micro-structural zones of the specimen, cf. Section 4.5.

The mean stress dependency of the 6082-T6 aluminium alloy crack propagation data has been investigated and a Walker exponent $\gamma = 0.78$ has been calculated. This value is somewhat higher than $\gamma \approx 0.6$, which was found suitable for the 7075-T6 and 2024-T3 aluminium alloys, i.e. the mean stress dependency of the 6082-T6 alloy is less pronounced.

Beside the data obtained, the tests gave valuable information about possible modifications to improve the experiments. It was found that the tests are very sensitive to stops. After a longer stop, the crack propagation rates remained constant for a while or even decreased. This behaviour is probably due to the formation of an oxide layer, which reduces the effective ΔK. The use of a liquid to make the crack visible may slow down crack growth too.

The following points may be considered to increase the quality and to test even shorter cracks:

- Machining of very plane specimens to avoid out-of-plane bending.
- Thinner specimens (1.5-2 mm) would increase the electrical resistance of the specimens, hence increase the measured potential drop.
- Heat treatment of the specimens in order to obtain a homogeneous microstructure.
- Use a central indent as a starter notch to develop a through edge crack faster.
- After having initiated a through edge crack, the crack depth should be reduced as much as possible ($a \approx 0.1$ mm) by machining the edge of the specimens.
- The load range used to initiate a crack should be maintained throughout propagation.

When planning the experiments it was intented to adjust the loading during the tests in order to keep ΔK relatively constant. It was expected to get data points describing a vertical line in a $\mathrm{d}a/\mathrm{d}N$ versus ΔK plot, which would clearly indicate the faster growth whilst the cracks are short. However, small load reductions immediately resulted in crack arrest and the idea had to be abandoned. Designing the test setup to enable a “continuous” load reduction should make such measurements possible.

CHAPTER 5

A welded T-joint subjected to 4-point bending

In order to support or reject the thesis stated in Chapter 1 and to find answers to the questions raised, the most common fatigue life assessment approaches, cf. Chapter 2, have been applied to the same structure, a welded T-joint subjected to 4-point bending loading. In addition, due to the availability of experimental data generated on T-joints with different residual stress level, the effect of the stress ratio, i.e., the residual stress, has been included in the analysis, using Walker's equation with $\gamma = 0.78$, cf. Chapter 4.

5.1 Background

5.1.1 Fatigue tests

As a part of a parallel project within the NorLight framework, welded T-joints, see Figs. 5.1 and 5.2, made from extruded 6082-T6 aluminium alloy profiles with rectangular hollow cross-section (RHS), were produced and fatigue tested. The specimens were welded according to the welding procedure specification given in Appendix D. A detailed description of the test conditions and the results has been published in [32]. Therefore, only a brief summary of the experiments will be given here.

The specimens were subjected to 4-point bending, see Fig. 5.3a, at $R = 0.1$. One of the main goals of those experiments was to explore the fatigue life improvement due to artificially introduced residual stresses at the weld. The methods for introducing the superimposed residual stress fields were verified through welding simulations [78]. Two series of specimens were tested. The joints of the first series (batch 1) were simply welded together, while the two profiles were kept in position. In the joints of the second series (batch 2) a compressive residual stress

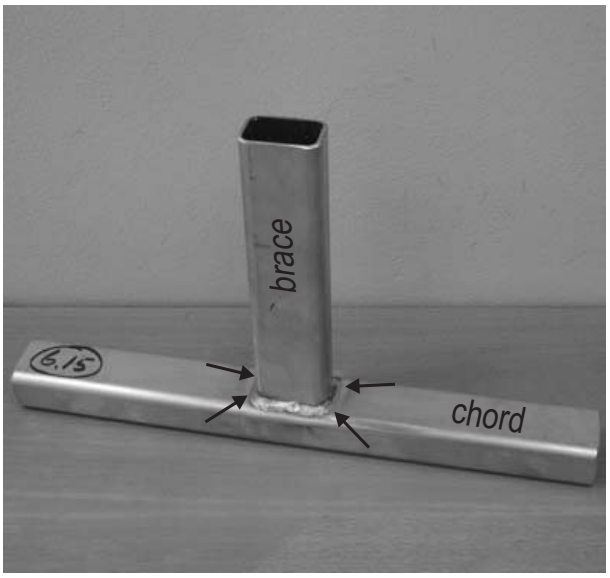

Figure 5.1: T-joint made from rectangular hollow sections. The arrows indicate the corner areas at one of which the crack starts propagating.

in the loading direction was introduced at the weld toe. This was achieved by elastically deforming the lower profile (chord), see Fig. 5.3b, prior to and during the welding. After welding the chord was unloaded thus adding a compressive stress to the tensile welding stress.

During testing it was found that cracks first become visible at one of the "corners" along the weld toe, see arrows in Fig. 5.1. This behaviour could be expected, since those areas have the highest stress concentration. The crack subsequently propagates into the chord and after having penetrated the profile wall thickness, it propagates along the weld toe. Final fracture occurs just after the upper flange has fractured completely. Figure 5.4 shows a cross section of the weld and illustrates the region where the crack propagates. The obtained fatigue lives have been plotted in Fig. 5.5. Underneath the weld toe, there appears to be a zone of limited or no fusion. This zone is marked "cold lap". Cold laps of aluminium welds are often caused by a surface oxide layer, which has a considerable higher temperature of fusion than metallic aluminium (2050°C and 650°C, respectively). Since the temperature at the rim of the weld bead during welding is somewhat lower than the temperature inside the weld bead, the temperature is probably not sufficient to break down the oxide layer in order to obtain complete fusion at the weld toe. Actually, similar features are normally seen in aluminium production welds, even though the welds meet the specifications. As indicated in Fig. 5.4, the cracks propagated a small distance, usually a few tenth of a millimetre, behind the weld toe creating a small lip. This was seen as an indication of limited fusion. However, the lip was always much smaller then the zone marked "cold lap" in Fig. 5.4 would suggest. Even if there is a zone of limited fusion at the weld toe only a very small amount of mode II crack growth could be expected. In a study on welded cruciform steel joints, cold laps have been shown to reduce the fatigue strength [99], since cold laps act as sites for fatigue crack initiation. It has been shown that a crack growing from a cold lap rapidly reaches a vertical orientation [100]. Therefore, the analyses were based on the assumption of mode I crack propagation in the through thickness direction The cold lap was taken into

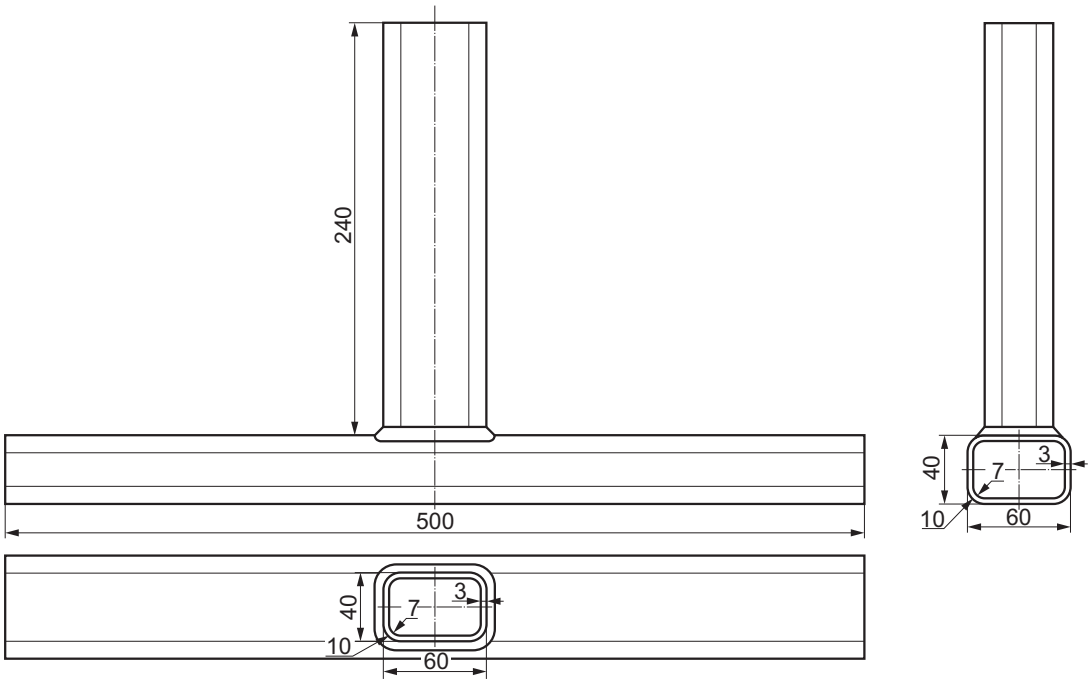

Figure 5.2: Drawing of the T-joint.

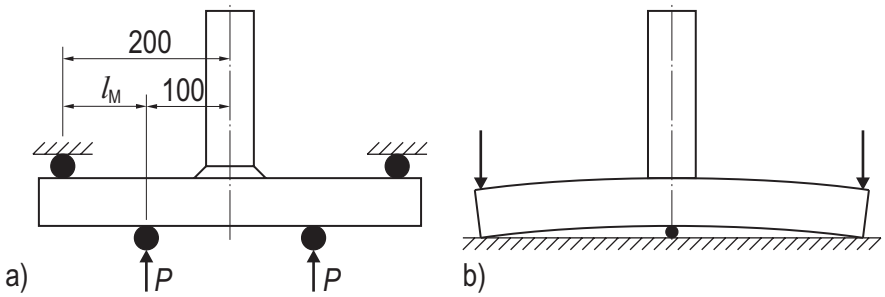

Figure 5.3: (a) T-joint subjected to 4-point bending, (b) elastically pre-deformed chord.

account by assuming a zero weld toe radius when choosing the M_k equation for the crack propagation analysis.

Using linear regression (least mean squares method), Basquin's law, Eq. 2.1, was fitted to the test data [32]. The constants σ_f', representing mean values, the exponents b and the standard deviation of $\log N_f$, $s_{\log N_f}$, are given in Table 5.1. In addition, the values for the mean minus two standard deviation curve are given. The corresponding mean S-N curves have been plotted in Fig. 5.5.

5.1.2 Calculating the nominal stress

Calculating the nominal stress in the chord is rather straightforward. The 4-point bending applies a bending moment $M_A = Pl_M$ to the part of the chord between the two inner loading points, see Fig. 5.3a. From beam theory the following

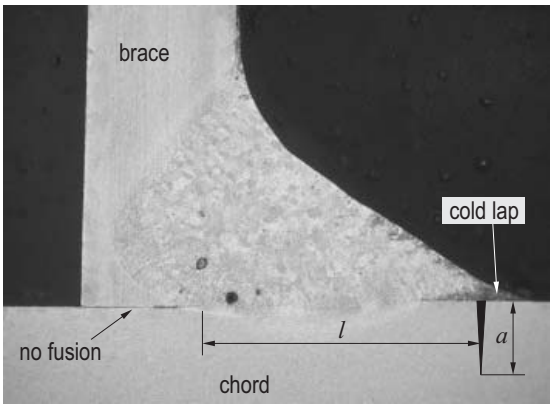

Figure 5.4: Cross section of the weld.

Table 5.1: Constants in Basquin's law for batches 1 and 2.

		$1/b$	σ'_{f} [MPa]	A ($\Delta\sigma$ [MPa], N [cycles])	$s_{\log N_{\mathrm{f}}}$
mean	Batch 1	-4.63	647	1.30×10^{14}	0.11
	Batch 2	-5.07	633	2.76×10^{15}	0.15
mean $- 2s_{\log N_{\mathrm{f}}}$	Batch 1	-4.63	581	7.93×10^{13}	
	Batch 2	-5.07	551	1.37×10^{15}	

equation to calculate the bending stresses is known:

$$S = \frac{M}{I_{\mathrm{chord}}} y \,, \tag{5.1}$$

where y is a coordinate running from the centre of the chord section ($y = 0$) to the lower surface ($y = 20$ mm) of the chord, thus, the maximum nominal tensile stress, $S_{\max}$, is found at the upper surface ($y = -20$ mm). With $I_{\mathrm{chord}} = 125\,830$ mm^4, see Appendix C, and $M = -M_{\mathrm{A}}$, Eq. 5.1 becomes

$$S_{\max} = \frac{1.59 \times 10^{-4}}{\mathrm{mm}^3} M_{\mathrm{A}} \,. \tag{5.2}$$

5.1.3 Residual stress

Since the batch 2 specimens were given a compressive residual stress field at the weld toe, it is desirable to include this when estimating the fatigue life. In general, the residual stress magnitude and its distribution in welded structures are unknown. A rough method to estimate the residual stress level is based on prevented contraction of the weld whilst cooling down, see for example Berkovits et al. [19]. Fortunately, the residual stress in the T-joint has been calculated, cf. [32], using the finite element program WELDSIM, a proprietary code to simulate and optimize the welding process [20–22, 78]. Plots of the residual stress distributions in the z-direction (along the axis of the chord) for batches 1 and 2 are shown in Fig. 5.6. As can be seen from this figure, the residual stress com-

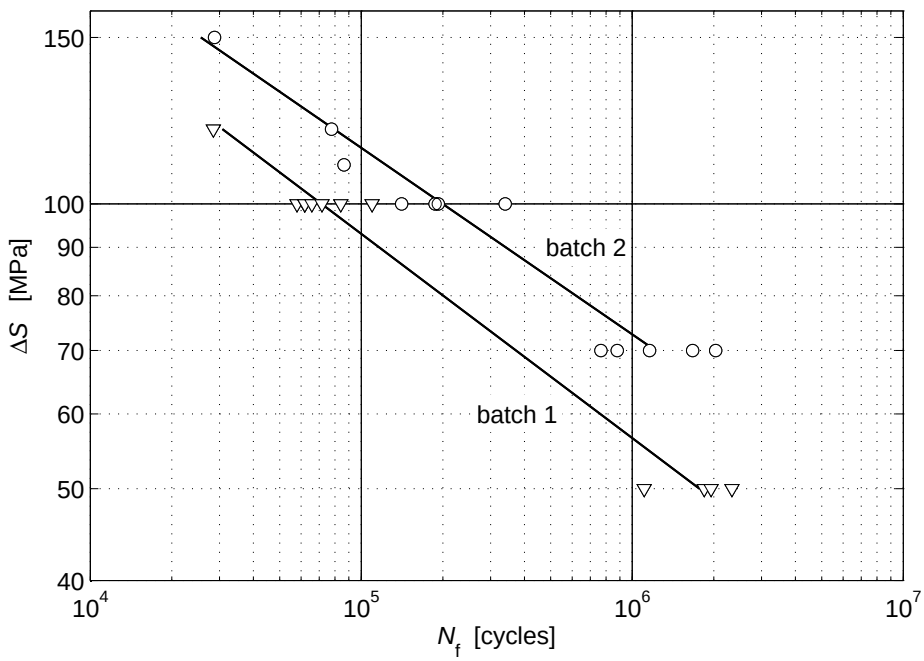

Figure 5.5: Experimentally found fatigue lives for batches 1 and 2 and the corresponding mean S-N curves.

ponent in the z-direction is relatively evenly distributed along the weld toe. It must be mentioned that the finite element mesh density was not high enough to obtain the residual stress distribution through the wall thickness and the stress peak at the weld toe. Hence only a through-thickness mean value of the residual stress is shown in Fig. 5.6. The required, much higher mesh density to obtain a very detailed residual stress distribution would demand excessive computation time and was not feasible. However, it was assumed that the calculated mean values were sufficient with respect to the fatigue life predictions presented later. Numerical values of the residual stress at the weld toe, estimated from the plots, are given in Table 5.2.

The residual stress acts as a mean stress, hence it changes the stress ratio, R. Therefore, to include the effect of the residual stress in the analysis, the stress ratio must be calculated locally, at the point where fatigue cracking is expected. Using the relations between the maximum, the minimum and the mean stress and the stress range, the stress ratio can be written as

$$R = \frac{\sigma_{\mathrm{m}} - \Delta\sigma/2}{\sigma_{\mathrm{m}} + \Delta\sigma/2}\,. \tag{5.3}$$

The stress ratio at the weld toe, R_{weld}, which includes the residual stress, has been calculated from Eq. 5.3, where $\sigma_{\mathrm{m}} = S_{\mathrm{m,weld}} = S_{\mathrm{m}} + S_{\mathrm{residual}}$. R_{weld} is a nominal stress ratio including the nominal stress. If the through-thickness distribution at the weld toe of both the applied and the residual stress is known, a real local stress ratio could be calculated. This stress ratio would be not constant in the through-thickness direction.

The stress ratios at the weld toe for two stress ranges are given in Table 5.2. It can be seen that the actual stress ratio at the weld toe differs strongly from

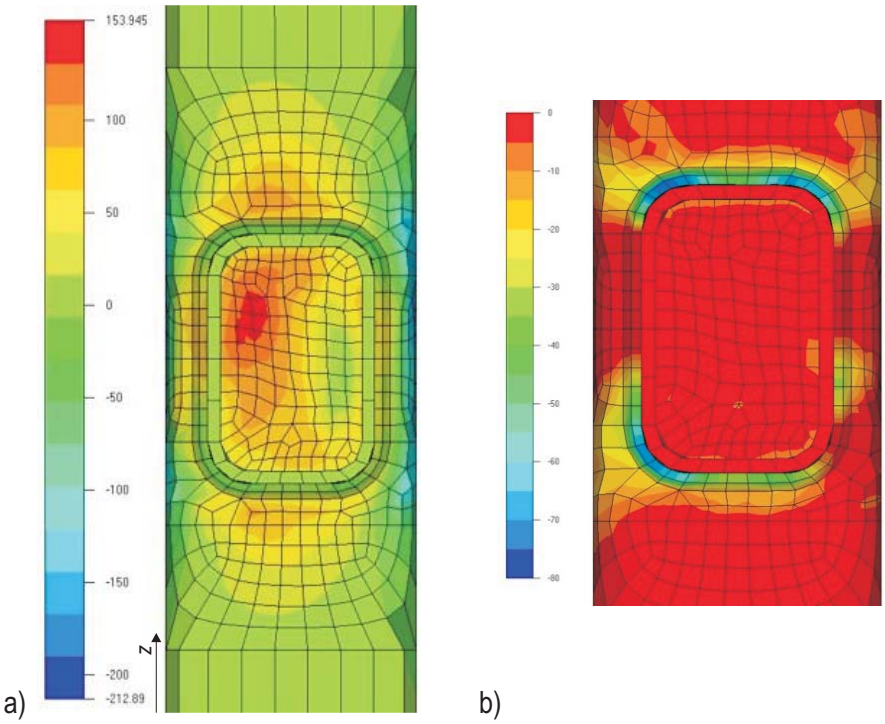

Figure 5.6: Residual stress distribution in the z-direction [32]: (a) batch 1 and (b) batch 2.

the nominal applied stress ratio and therefore must be taken into account when predicting fatigue life.

Table 5.2: Stress ranges, mean stresses, residual stresses and stress ratios at the weld toe.

	R	ΔS [MPa]	S_{m} [MPa]	S_{residual}† [MPa]	$S_{\mathrm{m,weld}}$ [MPa]	R_{weld}
Batch 1	0.1	50	30.5	50	80.5	0.53
		100	61.1	50	111.1	0.38
Batch 2	0.1	50	30.5	-20	10.5	-0.41
		100	61.1	-20	41.1	-0.10

† - Calculated by means of WELDSIM (see e.g. [78])

5.1.4 Material data

The T-joints were produced from extruded 6082-T6 aluminium alloy profiles and the material data used in the analyses are listed in Table 5.3. $R_{\mathrm{p0.2}}$ and R_{m} are lower bound data stated by Hydro Automotive Structures. C, m and ΔK_{th} have been approximated from $\mathrm{d}a/\mathrm{d}N$ versus ΔK plots in Eurocode 9 [5].

Table 5.3: 6082-T6 aluminium alloy material data.

$R_{p0.2}$	R_m	m		C (m/cycle, MPa$\sqrt{m}$)		ΔK_{th} [MPa$\sqrt{m}$]	
[MPa]	[MPa]	$R = 0.1$	$R = 0.8$	$R = 0.1$	$R = 0.8$	$R = 0.1$	$R = 0.8$
270	300	4.0	3.9	2×10^{-11}	8×10^{-11}	3	1

5.1.5 Micro-structure

Figure 5.7 shows the micro-structure near the weld. Figure 5.7a represents a cross section parallel to the axis of the chord and Fig. 5.7b shows a cut along the weld slightly behind the weld toe perpendicular to the axis of the chord. The weld itself has a fine grain structure, whereas the chord has large grains in a layer below the top and bottom surfaces. Between these two layers, the grain structure is very fine. The grain structure in the chord near the weld seems almost unaffected by the welding process. The variation in the through-thickness micro-structure is reflected in the fracture surfaces observed during the short crack growth tests, cf. Chapter 4.

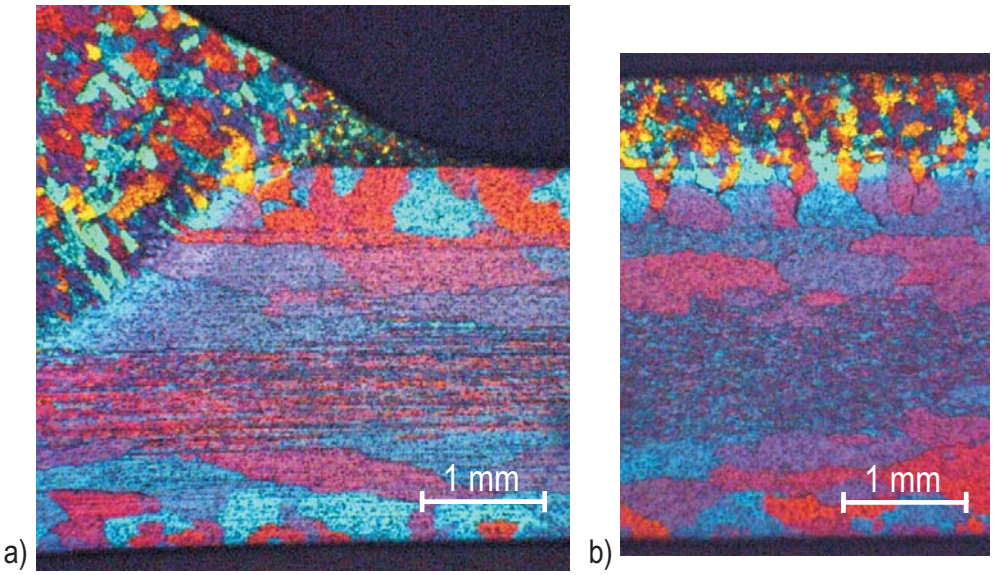

Figure 5.7: Micro-structure near the weld: (a) parallel to the axis of the chord and (b) perpendicular to the axis of the chord.

5.2 Nominal stress

The relatively simple T-joint geometry seems well suited to assess fatigue life using nominal stress. The nominal stress is calculated from Eq. 5.2. Following Eurocode 9, it should be modified for the shear lag effect. However, finite element analyses presented in [32] have shown that the effect is almost negligible in the analysed T-joints.

Finding a suitable detail category is not as straightforward as it might seem, since joints made from hollow sections are often not given. As can be seen from Table 5.4, using different codes and standards leads to slightly different detail categories, and the Basquin exponents differ slightly too. The effect of the differences is seen in Fig. 5.8, where experimental data and the design S-N curves are plotted.

Table 5.4: Nominal stress detail categories for the T-joint and the corresponding constants in Basquin's law.

	Comment	Detail category	f	ΔS_{C} † [MPa]	$1/b$	A (ΔS [MPa], N [cycles])
BS 8118 [14]		20	—	20.0	-3.0	1.60×10^{10}
Eurocode 9 [5]	$t < 4$ mm	25	—	25.0	-3.2	5.95×10^{10}
IIW [6]	batch 1	20	1	20.0	-3.0	1.60×10^{10}
	batch 2	20	1.16	23.2	-3.27	5.84×10^{10}
ECCS [15]	detail E6	23	—	23.0	-3.37	7.76×10^{10}

† at $N = 2 \times 10^6$ cycles

The different design curves lie within a factor of ≈ 1.7 in life. The curve from Eurocode 9, representing $t < 4$ mm, has been chosen, since the thin walled hollow section behaves more like a thin plate ($t = 3$ mm) than a massive section ($t = 40$ mm), see Section 5.5.2. For batch 2, a fatigue enhancement factor $f = 1.16$ has been calculated (IIW), which leads to a fatigue strength at 2×10^6 cycles of $\Delta S_{\mathrm{C}} = 23.3$ MPa. Rotating the design curve from detail category 20 around the point at $N = 1 \times 10^4$ cycles, such that it passes through ΔS_{C}, the enhanced design curve is obtained. This curve has a slope of $1/b = -3.27$.

All design curves are conservative. The conservatism increases the lower the stress range becomes, which is due to the different exponents $1/b \approx -3$ and $1/b \approx -5$ for design curves and experimental curves, respectively. The different exponents may be an indication of higher quality welds in the experiments leading to a longer crack initiation period, which in turn is more pronounced at low stresses. Introducing the fatigue enhancement factor does not give a remarkable improvement.

5.3 Structural hot spot stress

The structural hot spot stress concentration factor used in this study has been based on surface stress extrapolation and the extrapolation scheme adopted by IIW [6]. As mentioned in Chapter 2, new and perhaps more robust and versatile extrapolation methods to estimate the structural stress based on the stress distribution through the thickness have recently been suggested, e.g., [26,33,34]. However, none of these has yet been included in design codes and recommendations and an assessment using alternative extrapolation schemes will not be included in this study.

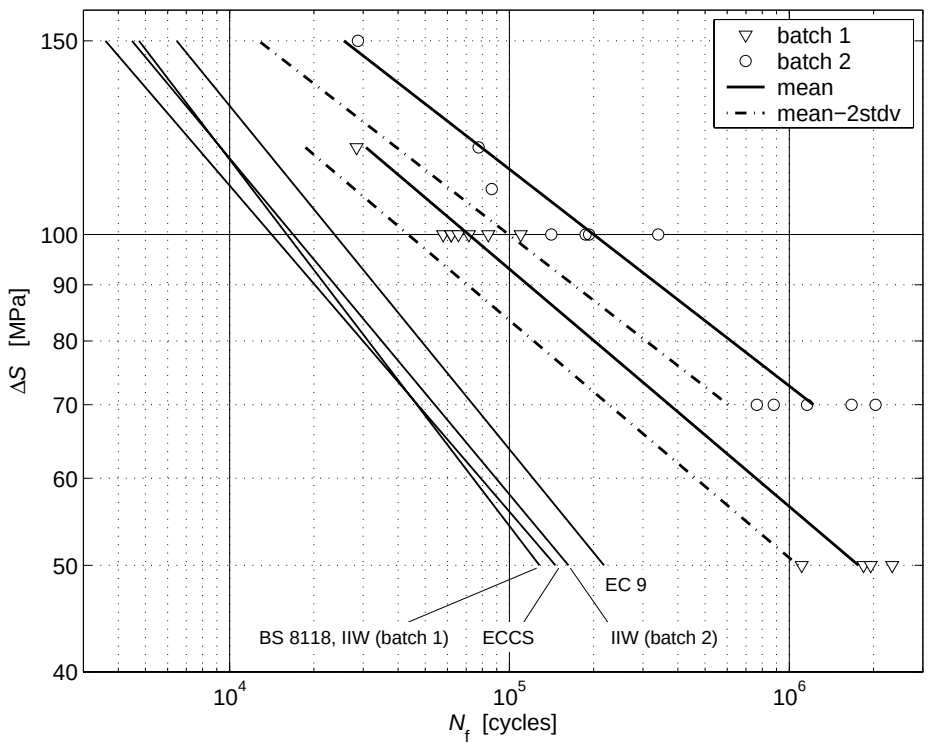

Figure 5.8: Experimental S-N curves for batches 1 and 2 compared to nominal stress design curves from Eurocode 9 [5], BS 8118 [14], IIW [6] and ECCS [15].

Structural hot spot stress design curves are given in Eurocode 9 [5] and in the IIW recommendations [6]. Eurocode 9 gives the structural hot spot stress design curves as a function of member thickness. As for nominal stress, the curve for $t < 4$ mm was chosen, which corresponds to "detail category" 44. The exponent $1/b = -3.2$ is the same as for nominal stress. IIW assigns two different detail categories to nine different joints. The T-joint falls into detail category 40 with $1/b = -3$. A fatigue enhancement factor $f = 1.16$ is calculated for batch 2, which leads to a fatigue strength $\Delta\sigma_{\mathrm{C,hs}} = 46.4$ MPa at 2×10^6 cycles. Rotating the design curve from detail category 20 around the point at $N = 1 \times 10^4$ cycles, such that it passes through $\Delta\sigma_{\mathrm{C,hs}}$, the enhanced design curve, which takes the beneficial effect of the compressive residual stress into account, is obtained. This curve has a slope of $1/b = -3.27$. All Basquin constants are listed in Table 5.5.

5.3.1 Structural hot spot stress concentration factor

So far, the experimental results have been plotted as a function of nominal stress. To be comparable with the structural hot spot stress design curves, either experimental results or design curves must be transformed. This is achieved by multiplication with the structural hot spot stress concentration factor, K_{hs}, which is defined as

$$K_{\mathrm{hs}} = \frac{\sigma_{\mathrm{hs}}}{S}\,, \tag{5.4}$$

Table 5.5: Structural hot spot stress "detail categories" for the T-joint and the corresponding constants in Basquin's law.

	Comment	Detail category	f	$\Delta\sigma_{\mathrm{C,hs}}$ † [MPa]	$1/b$	A (ΔS [MPa], N [cycles])	ΔS_{C} †† [MPa]
Eurocode 9 [5]	$t < 4$ mm	44	—	44	-3.2	3.63×10^{11}	20.7
IIW [6]	batch 1	40	1	40	-3.0	1.28×10^{11}	18.8
	batch 2	40	1.16	46.4	-3.27	5.63×10^{11}	21.8

† at $N = 2 \times 10^6$ cycles, †† at $N = 2 \times 10^6$ cycles using $K_{\mathrm{hs}} = 2.13$

where σ_{hs} and S are the structural hot spot stress and the nominal stress, respectively. Tveiten [32] has compiled a detailed analysis on the influence of FE element choice, weld stiffness representation and extrapolation method on the calculation of the structural hot spot stress in the T-joint. Using quadratic volume elements with reduced integration and linear extrapolation (extrapolation and modelling principles based on recommendations given by IIW [6], Niemi [17], and Tveiten and Moan [31]) he obtains $K_{\mathrm{hs}} = 2.13$.

It was decided to transform the design curves rather than the experimental results to obtain direct comparability to the other diagrams. Converting Basquin's law from structural to nominal stress is done as follows:

$$N_{\mathrm{f}} = A\,(\Delta\sigma_{\mathrm{hs}})^{1/b} = A\,(K_{\mathrm{hs}}\Delta S)^{1/b}\ . \tag{5.5}$$

The resulting S-N curves are plotted in Fig. 5.9. All design curves are conservative and are almost identical with the results from the nominal stress approach, cf. Fig. 5.8. Again, the fatigue enhancement factor gives only a negligible contribution and is not capable to account for the effect of the compressive residual stress.

5.3.2 Parametric equations

The structural hot spot stress concentration factor for many joint geometries can be found from parametric equations. In the IIW recommendations *Fatigue Design Procedure for Welded Hollow Section Joints* [101], there is an extensive collection of such equations for joints made from tubular and rectangular hollow section. Although those recommendations refer to steel joints, they should be applicable to aluminium joints as well, since K_{hs} should be independent of the material. Along lines D and C, see Fig. 5.10, the following equations are given:

$$K_{\mathrm{hs}} = 1.373(2\gamma)^{0.205\beta}\,\tau^{0.24} \qquad \text{(line D)} \tag{5.6}$$

$$K_{\mathrm{hs}} = 0.725(2\gamma)^{0.248\beta}\,\tau^{0.19} \qquad \text{(line C)}\,, \tag{5.7}$$

with $2\gamma = b_{\mathrm{chord}}/t_{\mathrm{chord}}$, $\beta = b_{\mathrm{brace}}/b_{\mathrm{chord}}$ and $\tau = t_{\mathrm{brace}}/t_{\mathrm{chord}}$, where b and t are section width and wall thickness, respectively.

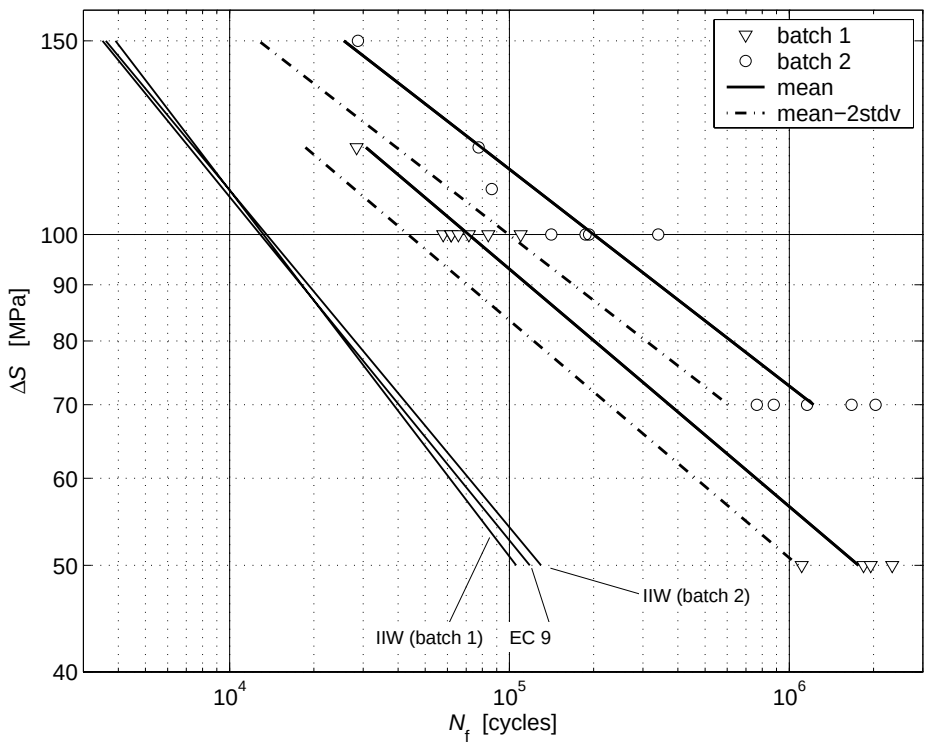

Figure 5.9: Experimental S-N curves for batches 1 and 2 compared to structural hot spot stress design curves from Eurocode 9 [5] and IIW [6] expressed in terms of nominal stress.

With $b_{\text{brace}} = 40$ mm, $b_{\text{chord}} = 60$ mm and $t_{\text{brace}} = t_{\text{chord}} = 3$ mm, see Fig. 5.2, $2\gamma = 20$, $\beta = 0.67$ and $\tau = 1$, thus, $K_{\text{hs}} = 2.07$ and 1.19 along line D and line C, respectively. Comparing the value along line D with $K_{\text{hs}} = 2.13$ from [32] very good agreement is found, especially considering the variation in the K_{hs} predictions from 1.78 to 2.13 due to different finite elements, weld idealisations and extrapolation methods [32]. $K_{\text{hs}} = 2.13$ was used in Fig. 5.9, because it appears to be the most realistic value since it was obtained from a finite element analysis of the actual geometry using volume elements.

5.4 Effective notch stress

After having applied both the nominal and the structural hot spot stress approach to the T-joint, the effective notch stress approach will be examined.

In order to calculate the stress at the expected failure site, a very fine finite element mesh is required to capture the local geometry. In general, the global model of a structure is far too coarse to give local stresses, and the modelling effort, computing time and hardware resources required prohibit the modelling of a complex structure in enough detail. The sub-modelling technique presents a possible solution to this problem. A sub-model from the region close to the expected failure site is created, which contains all geometrical features that have an impact on the local stress. Along the boundary between the global model and the sub-model, the results from the global-model, i.e., displacements and

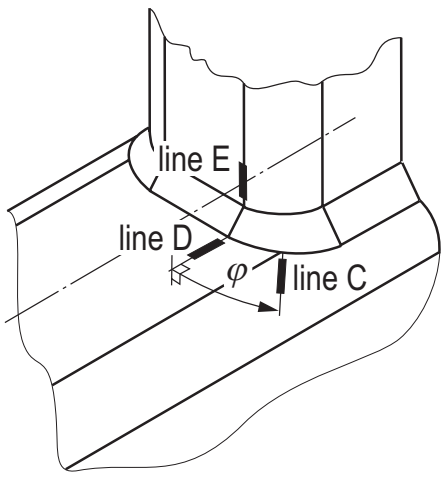

Figure 5.10: Definition of the lines along which the hot spot stress concentration factor is given.

rotations, become boundary conditions of the sub-model.

The next problem encountered is very pronounced when analysing welded structures. The local geometry, especially the weld toe radius, underlies large scatter along a weld seam and from component to component. Setting the weld toe radius to zero the weld notch becomes singular and the stresses in an FE analysis will depend on the mesh density and will not converge. From this point of view, Neuber's approach defining a fictitious weld toe radius, ρ_f, which gives K_f directly is very attractive, see Eq. 2.13. Conservatively assuming $\rho = 0$, cf. Radaj [18], results in $\rho_f \neq 0$, hence a finite radius that can be modelled with finite elements.

According to Tveiten [32], the weld toe radius and the weld angle in the T-joint varies between 0.9 and 2.3 mm with a mean value of 1.3 mm and between 17° and 57° with a mean value of 35°, respectively. Thus, assuming $\rho = 0$ might be too conservative. However, it is often difficult to conclude whether there is a radius at all. In addition, if the cold lap presents a zone of no or limited fusion, the weld toe radius would be practically zero.

In order to get an idea how important the weld toe radius and the weld angle are, both have been varied in a series of FE analyses.

5.4.1 Stress analysis

A finite element model of the T-joint was created using ABAQUS CAE and analysed with ABAQUS Standard. Due to symmetry only a quarter of the T-joint was modelled, see Fig. 5.11a. When meshing with three-dimensional elements, local mesh refinement is difficult, especially when the stress output along certain paths is required, e.g., perpendicular to the weld toe. In order to keep the fine mesh at the weld and reduce the required hardware resources and computing time, two sub-models were generated. The first sub-model (sub-1), see Fig. 5.11b, receives the boundary conditions from the global model and the second sub-model (sub-2), see Fig. 5.11c, receives its boundary conditions from the first sub-model.

During the fatigue tests, the load was applied to the chord through cylindrical rods, see Fig. 5.3a. Due to the different stiffness in the flanges and webs of the

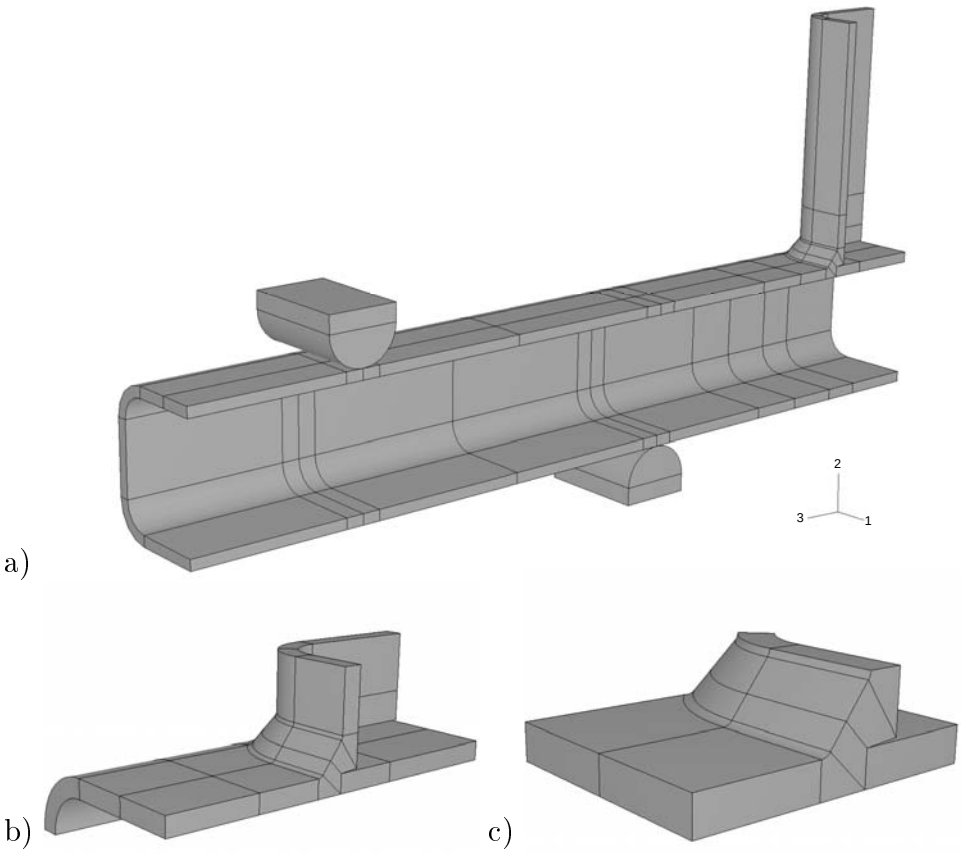

Figure 5.11: Model geometry: (a) global model, (b) first sub-model, (c) second sub-model.

hollow section, the section distorts so that the rods partly lose contact. The stiffness differences make modelling the load boundary conditions with line forces unrealistic [102]. Although, due to Saint-Venant's principle, the error from the locally incorrect boundary conditions should not affect the stresses at the weld toe, the rods have been modelled as well, see Fig. 5.11a. The interaction between the rods and the T-joint was modelled as a contact problem. Figure 5.12 plots the deformation near an actuator rod showing, when carefully examined, that rod and T-joint partly separate. Figure 5.13 shows the overall deformation of the T-joint.

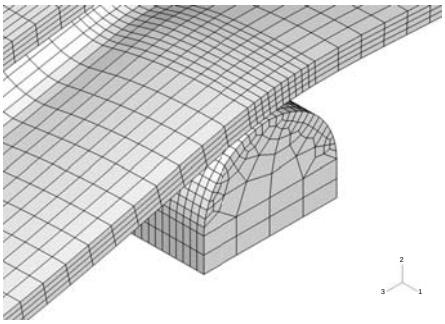

Figure 5.12: Local deformation at an actuator rod.

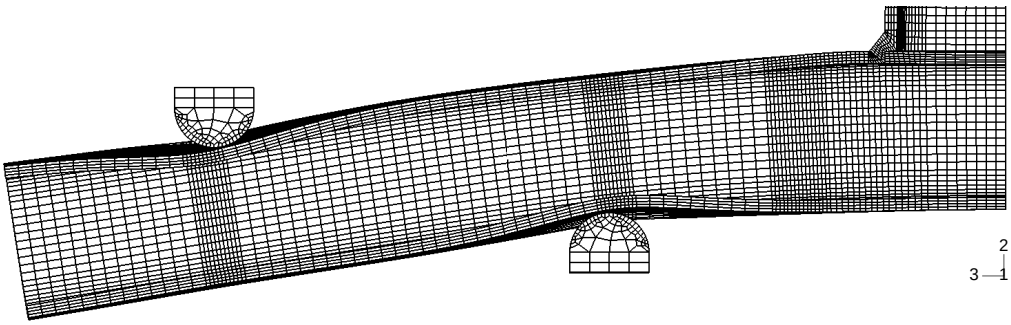

Figure 5.13: Deformation of the T-joint.

Convergence study

At first, a convergence study was carried out to find a mesh-element combination that reflects the local stress and its through-thickness distribution with sufficient accuracy. The global model was meshed with linear brick elements with reduced integration (ABAQUS element C3D8R) and with a mesh density near the weld as given in Table 5.6. After having analysed the first sub-model using the same mesh as for the global model to check whether it behaves in the same way as the global model, the mesh was refined. Thereafter, the second sub-model with an even more refined mesh and quadratic brick elements with reduced integration (ABAQUS element C3D20R) was analysed. In a final refinement step, the mesh of the second sub-model was constructed so that the mesh was denser near the weld toe (using biased mesh seeds). All these mesh configurations have been collected in Table 5.6.

Table 5.6: Model specifications from the convergence study ($\rho =$ 1 mm and $\theta = 45^{\circ}$) and stress concentration factors, based on von Mises equivalent stress.

	Element	Number of elements*				K_t	
Model	type	M1†	M2†	M3†	M4†	A†	B†
Global	C3D8R	4(1)	6(1)	10(1)	10(1)	1.19	1.63
Sub-1	C3D8R	8(1)	8(1)	20(1)	20(1)	1.36	1.86
Sub-2a	C3D20R	8(1)	8(1)	20(1)	20(1)	1.66	2.25
Sub-2b	C3D20R	8(3)	8(3)	30(1)	20(10)	1.70	2.32

* Numbers in brackets denote bias, † defined in Fig. 5.14a.

Figure 5.14b presents the von Mises equivalent stress obtained with the second sub-model (no bias). It is immediately seen that the stress along the weld toe is highest in the curved part and it is, therefore, not surprising that the cracks started in this area during the experiments.

The stress concentration factor at the weld toe at both the symmetry line and the point of maximum stress is given in Table 5.6. It should be noted that the

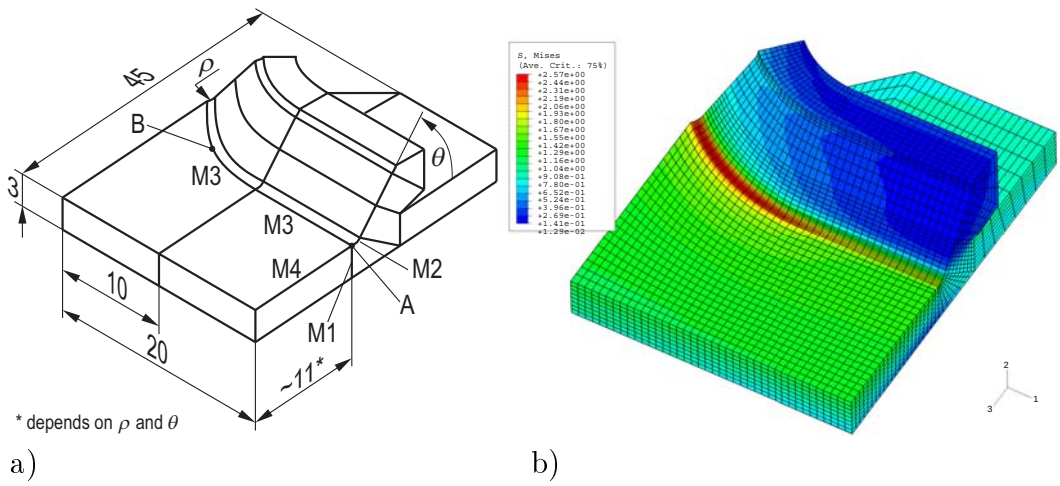

Figure 5.14: (a) Mesh definition notation and the points (A and B, where B marks the maximum von Mises stress) at which K_t is calculated, (b) Von Mises equivalent stress.

highest stress is not obtained at the weld toe but some distance into weld toe radius.

The through-thickness von Mises stress distributions from the different finite element models have been plotted in Fig. 5.15. As expected, the linear elements are inferior to the quadratic elements. Even using quadratic elements requires a relatively large number of elements through the wall thickness. Finally, it can be concluded that both meshes used with the second sub-model give reasonable results.

In order to get a detailed overview of the stress state at the most highly stressed point, all stress components have been extracted from the finite element analysis and Mohr's stress circle has been constructed. Both stress values and Mohr's stress circle are given in Fig. 5.16.

It is seen that the principal axes 1 and 2 are almost perpendicular and tangential to the global axes x and y, respectively. The third principal stress is practically zero as it should be, because of the free surface. Since $\sigma_2/\sigma_1 = 0.24$ the von Mises equivalent stress is 10 % less than the Tresca equivalent stress.

5.4.2 Estimating the fatigue life

Unfortunately, no S-N curve obtained with smooth specimens manufactured from weld or HAZ material is available. However, in context with the effective notch stress approach according to Radaj, the IIW recommendations [6] give FAT 75 and $1/b = -3$. The corresponding Basquin constants are listed in Table 5.7.

Based on the stress analysis in the previous section, the fatigue notch factor and the fatigue life is estimated. The T-joint obeys a relatively simple geometry, which allows to define a nominal stress. Thus, beside the stress gradient and Radaj's approach, both Peterson's and Neuber's equations to estimate the notch sensitivity can be applied and compared to each other. For a description of the approaches see Section 2.5.2. The stress gradient approach requires the

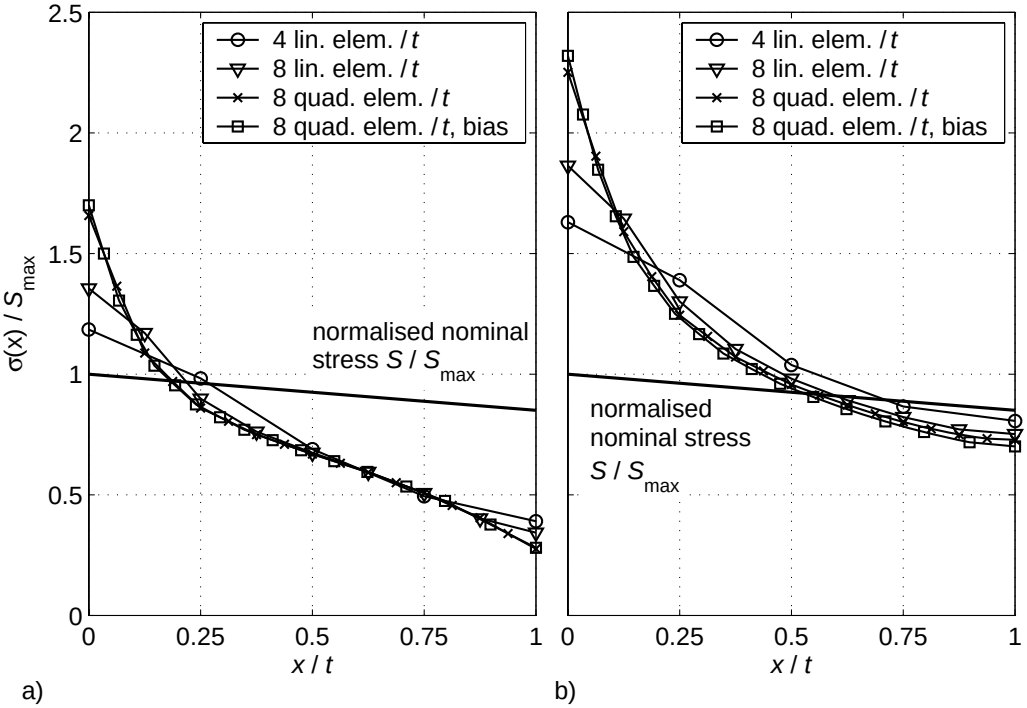

Figure 5.15: Normalised von Mises equivalent stress through-thickness distribution at the weld toe: (a) in the symmetry line (point A), (b) maximum value (point B).

stress/nominal stress	
$\sigma_x/S_{\max}$	2.56
$\sigma_y/S_{\max}$	0.62
$\sigma_z/S_{\max}$	0.02
$\tau_{xy}/S_{\max}$	-0.13
$\tau_{xz}/S_{\max}$	-0.08
$\tau_{yz}/S_{\max}$	0.02
$\sigma_1/S_{\max}$	2.57
$\sigma_2/S_{\max}$	0.61
$\sigma_3/S_{\max}$	0.02
$\sigma_{\text{Mises}}/S_{\max}$	2.32

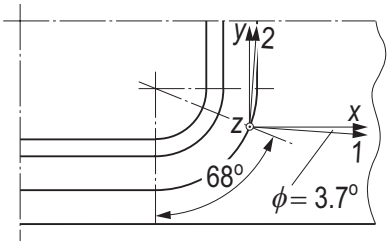

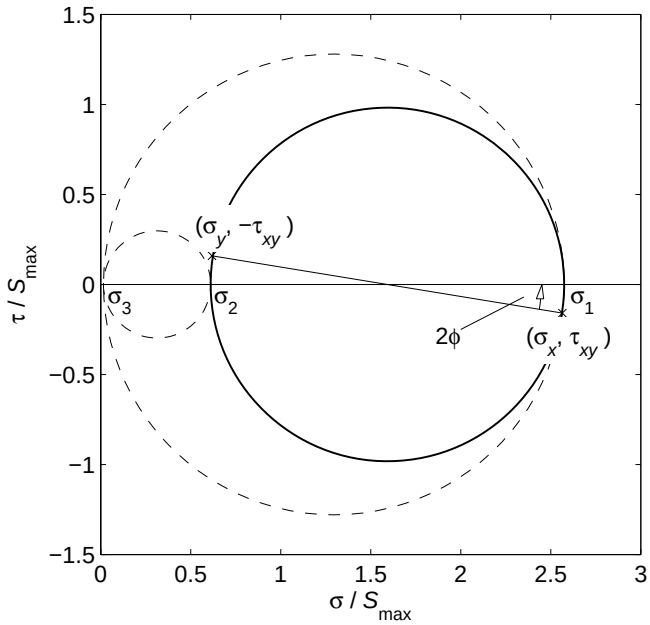

Figure 5.16: Stress components, principal stresses and von Mises equivalent stress at the point with the highest von Mises stress at the weld toe and Mohr's stress circle.

Table 5.7: Effective notch stress design curve and the corresponding constants in Basquin's law.

	"Detail category"	$\Delta\sigma_C$ † [MPa]	$1/b$	A (ΔS [MPa], N [cycles])	ΔS_C † [MPa] $K_f = 1.8$	$K_f = 2.32$
IIW [6]	75	75	-3.0	8.44×10^{11}	42	32

† at $N = 2 \times 10^6$ cycles

normalised stress gradient χ, which can be found from the finite element results. Using the von Mises stress field at point B, cf. Fig. 5.15b, χ becomes

$$\chi = \left| \frac{1}{\sigma_{\max}} \frac{\mathrm{d}\sigma}{\mathrm{d}x} \right|_{x=0} = \frac{1}{2.32} \frac{2.32 - 2.08}{0.1 \text{ mm}} = 1.03 \text{ mm}^{-1} . \tag{5.8}$$

Recalling Eq. 2.15, the relative stress gradient ahead of an U-notch subjected to tension loading can be roughly estimated by $\chi \approx 2/\rho = 2/1 \text{ mm} = 2 \text{ mm}^{-1}$, which is twice as much as the above result from the FE analysis. The main reason for this difference is the notch angle, which is 0° and 135° for U-notch and weld, respectively. The relevant equations and the required material constants to estimate the fatigue notch factor are listed in Table 5.8 together with the obtained fatigue notch factors. It is seen that the three approaches yield almost identical fatigue notch factors. Although, supported by Fig. 2.5 this must be expected, but such a good agreement is surprising and rather accidental.

Table 5.8: Fatigue notch factors calculated from $K_t = 2.32$ employing different approaches.

Approach	Eqs.	Material parameter [mm]	Geometric parameter	K_f
Peterson	2.9, 2.10	$\rho_0 = 0.64$ [42]	$\rho = 1$ mm	1.80
Neuber	2.9, 2.12	$\rho^* = 0.2$ [11]	$\rho = 1$ mm	1.81
Gradient	2.18, 2.20	$\rho^o = 0.075$ [11]	$\chi = 1.03$ mm^{-1}	1.82
Radaj	—	—	$\rho = \rho_f = 1$ mm	2.32

Having estimated K_f, the effective notch stress S-N curve can be expressed in terms of the nominal stress as follows:

$$N_f = A\,(\Delta\sigma)^{1/b} = A\,(K_f \Delta S)^{1/b} . \tag{5.9}$$

With the Basquin parameters given in Table 5.7, the S-N curve prediction labelled $K_f = 1.8$ in Fig. 5.17 is obtained. It is seen that the prediction is in good agreement with the experimental curve. Only at higher stresses it is somewhat non-conservative.

Radaj's effective notch stress approach

Following Radaj's reasoning, see Section 2.5.2, the stress concentration factor obtained from the model with a weld toe radius $\rho = \rho_f = 1$ mm already represents

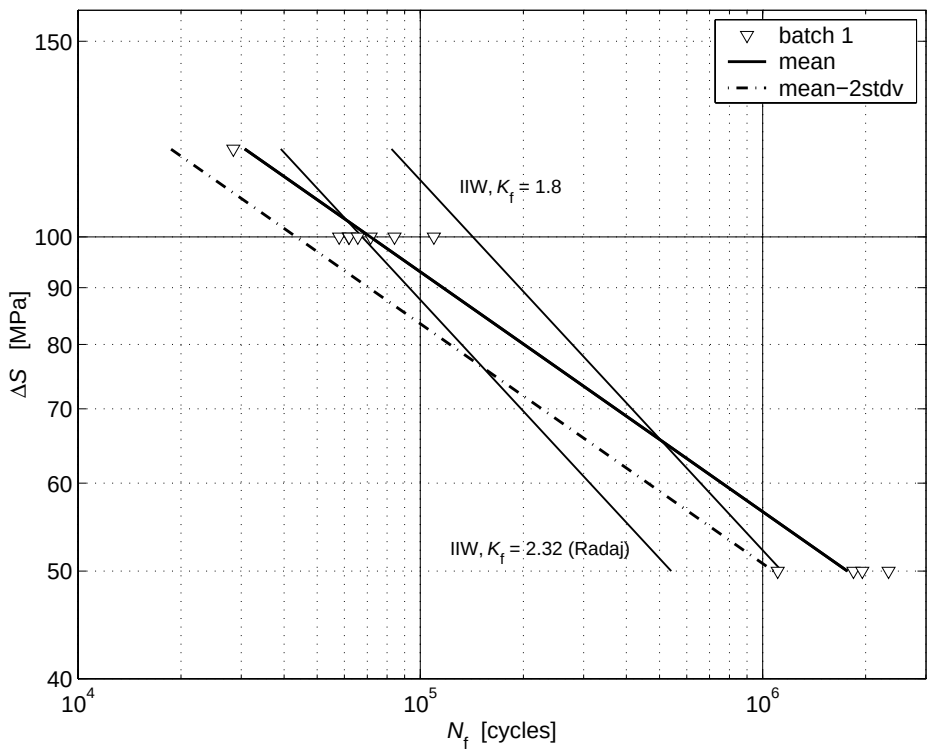

Figure 5.17: Experimental S-N curves for batches 1 and 2 compared to effective notch stress design curves from IIW [6] expressed in terms of nominal stress.

the fatigue notch factor, i.e., $K_\mathrm{f} = K_\mathrm{t} = 2.32$. The resulting S-N curve using the Basquin constants listed in Table 5.7 is plotted in Fig. 5.17. Excellent agreement between the prediction and the experimental curve is obtained. Although not recommended for joints with wall thickness less than 5 mm [6, 28], the results indicate the applicability of the method down to 3 mm wall thickness.

Impact of weld toe radius and angle

The main problem modelling the local weld geometry is that neither the weld toe radius, ρ, nor the weld angle, θ, have exactly determined values. It is, therefore, important to know the impact of ρ and θ on local stress and hence on fatigue life. A series of analyses to investigate the effect has been carried out, where the ABAQUS element C3D20R was used throughout. Table 5.9 sums the model specifications and the results.

Using Peterson's approach, see Section 2.5.2, with $\rho_0 = 0.64$ mm, cf. Table 5.8, gives the fatigue notch factors listed in Table 5.9. Employing Basquin's law to find the influence of the variations of K_f on fatigue life yields

$$\frac{N_\mathrm{f1}}{N_\mathrm{f2}} = \frac{A\left(K_\mathrm{f1}\Delta S\right)^{1/b}}{A\left(K_\mathrm{f2}\Delta S\right)^{1/b}} = \left(\frac{K_\mathrm{f1}}{K_\mathrm{f2}}\right)^{1/b} . \tag{5.10}$$

With $1/b = -3$, a decrease of the weld toe radius from $\rho = 1.5$ mm to $\rho = 0.5$ mm gives a rise in fatigue life by a factor 1.5. This rather surprising result is due to the K_f drop predicted with Peterson's approach when ρ/ρ_0 tends towards zero,

Table 5.9: Sensitivity study model specifications and the obtained stress concentration and fatigue notch factors.

			Number of elements*				B†	
No.	ρ	θ	M1†	M2†	M3†	M4†	K_t	K_f
1	0.5	52.0°	10(6)	8(4)	40(1)	16(10)	2.67	1.73
2	1.0	52.0°	8(3)	8(3)	30(1)	20(10)	2.32	1.80
3	1.5	52.0°	8(3)	8(3)	30(1)	20(10)	2.15	1.81
4	1.0	45.0°	10(6)	8(4)	40(1)	16(10)	2.23	1.75
5	1.0	41.5°	10(6)	8(4)	40(1)	16(10)	2.17	1.70

* Numbers in brackets denote bias, † defined in Fig. 5.14a.

see Fig. 2.3. Keeping $\rho = 1.0$ mm and decreasing the weld angle from $\theta = 52^{\circ}$ to $\theta = 41.5^{\circ}$ extends the fatigue life by a factor 1.2. This behaviour could be expected, since the larger θ the more abrupt is the change in cross section, hence the larger is the stress concentration. Summarising, it can be said that within the confines of this sensitivity study a very small effect of the weld geometry on the predicted fatigue life is found.

5.5 Crack propagation analysis

Integrating Paris' law, Eq. 2.28, gives after introducing the characteristic crack length, a^*, and the weld toe magnification factor, M_k, an equation to predict the fatigue life of a welded component containing small initial defects:

$$N_p = \frac{1}{C\left(\Delta S\sqrt{\pi}\right)^m} \int_{a_i}^{a_f} \left(M_k F \sqrt{a + a^*}\right)^{-m} \mathrm{d}a \,. \tag{5.11}$$

Since both F and M_k are functions of a, this equation must be integrated numerically. Before the integration is carried out, the influence of some variables on the analysis will be discussed.

5.5.1 The characteristic crack length a^*

If a crack propagates from a weld toe, and the stress concentration is expressed through the weld toe magnification factor, M_k, the following modified stress intensity factor range definition must be used:

$$\Delta\tilde{K} = M_k F \Delta S \sqrt{\pi\left(a + a^*\right)} \,. \tag{5.12}$$

Setting $\Delta K = \Delta K_{th}$ in Eq. 2.41 and replacing the local stress range, $M_k \Delta S$, with the fatigue limit of a smooth specimen, $\Delta\sigma_A$, gives after rearranging an equation to find a^*

$$a^* = \frac{1}{\pi}\left(\frac{\Delta K_{th}}{F \Delta\sigma_A}\right)^2 \,, \tag{5.13}$$

which is identical to Eq. 2.36. In order to calculate a^*, ΔK_{th} and $\Delta\sigma_{\mathrm{A}}$ must be converted to the same stress ratio. Applying Walker's equation, Eq. 5.13 can be written as

$$a^* = \frac{1}{\pi}\left(\frac{\Delta K_{\mathrm{th,Walker}}}{F\Delta\sigma_{\mathrm{A,Walker}}}\right)^2 = \frac{1}{\pi}\left(\frac{(1-R_{\mathrm{A}})^{1-\gamma_{\mathrm{A}}}\Delta K_{\mathrm{th}}}{(1-R_{\mathrm{th}})^{1-\gamma_{\mathrm{th}}}F\Delta\sigma_{\mathrm{A}}}\right)^2 , \tag{5.14}$$

where R_{A} and R_{th} are the stress ratios at which $\Delta\sigma_{\mathrm{A}}$ and ΔK_{th} are given, respectively.

The fatigue limit of a polished aluminium alloy test specimen at $R = -1$ may be estimated from the empirical equation

$$\frac{\Delta\sigma_{\mathrm{W}}}{2} = \sigma_{\mathrm{W}} \approx 0.4R_{\mathrm{m}} , \tag{5.15}$$

which is given in [11]. It must be noted that some authors point out that the traditional definition of the fatigue limit (stress amplitude at 2×10^6 cycles) may not be suitable for aluminium alloys. Beste [103] reports that for a number of aluminium alloys the S-N curves proceed with constant slope till beyond 1×10^9 cycles. From Eq. 5.15 the fatigue limit of the aluminium alloy 6082-T6 at $R = -1$ is estimated to $\Delta\sigma_{\mathrm{W}} = 240$ MPa.

In the effective stress intensity factor definitions proposed by El Haddad et al. [61] and Härkegård [62], the geometry factor, F, is assumed to be constant, which makes the calculation of a^* straightforward. Since the semi-elliptical surface crack analysed in this work obeys a geometry factor that is not constant, a problem is encountered when calculating a^*. Using the geometry factor equation for the deepest point of a semi-elliptical surface crack suggested by Newman and Raju [68], assuming $a = 0$, $a \ll t$ and $c \ll w$, a dependency on the, usually unknown, a/c ratio remains:

$$F = \frac{1}{\sqrt{1+1.464\left(\frac{a}{c}\right)^{1.65}}}\left(1.13 - 0.09\frac{a}{c}\right) . \tag{5.16}$$

The geometry factor defined through Eq. 5.16 is plotted as a function of a/c in Fig. 5.18. The curve does not vary dramatically with a/c. However, remembering that F is squared when calculating a^* the effect of the a/c ratio on the predicted fatigue life will be notable.

When the initial a/c ratio is known, which is rather unlikely, a^* can be calculated. In case of an unknown a/c ratio, a practical solution could be to use $F_{\mathrm{min}} = F(a/c = 1) = 0.66$, see Fig 5.18. The latter gives a large a^* and would therefore predict the shortest fatigue life when employing Eq. 5.12. According to Fig. 5.23, a crack will rapidly reach an aspect ratio $a/c \approx 0.35$ and maintain a/c between 0.4 and 0.5 under further propagation. It might, therefore, be an realistic choice to assume $F(a/c = 0.35) \approx 1$ when calculating a^*.

Inserting $\Delta K_{\mathrm{th}}(R = 0.1) = 3$ MPa$\sqrt{\mathrm{m}}$, see Table 5.3, assuming $\gamma_{\mathrm{th}} = 0.6$, and $\sigma_{\mathrm{A}}(R = -1) \approx 0.4R_{\mathrm{m}} = 120$ MPa, with $\gamma_{\mathrm{A}} = 0.5$, into Eq. 5.14 gives

$$a^* = \begin{cases} 0.25 \text{ mm}, & F = 0.66 \\ 0.11 \text{ mm}, & F = 1 \end{cases} . \tag{5.17}$$

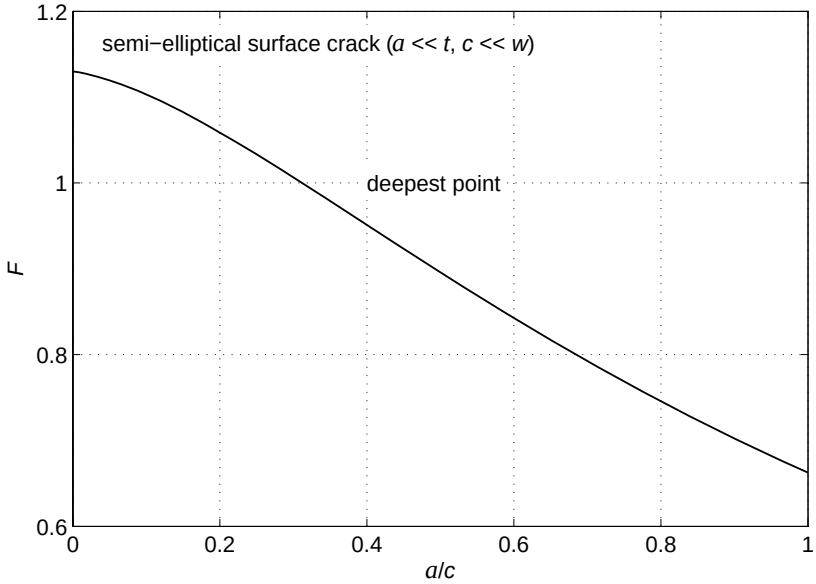

Figure 5.18: Geometry factor, F, [68] in the a-direction (deepest point) as a function of a/c.

$\gamma_{\mathrm{A}} = 0.5$ was chosen, since this makes Walker's equation equal to the mean stress equation suggested by Smith et al. [80] and $\gamma_{\mathrm{th}} = 0.6$ was used instead of 0.78, see Section 4.5.3, since the mean stress dependency is more pronounced at the threshold.

5.5.2 Finite versus infinite plate thickness

The equations to calculate F and M_{k} used in this work, were developed for a plate and a joint made from plates, respectively. Therefore, it is not straightforward to apply them to hollow sections. The main question is whether to set the "plate" thickness in the equations equal to the total section height or to the wall thickness of the section. Using the section height would result in a "thick" or infinite plate, whereas choosing the wall thickness would give a "thin" or finite plate, if the section is thin walled. Obviously, a crack starting at the surface of a hollow section will propagate through the section wall. It seems, therefore, most relevant to assume a crack propagating through a thin plate. However, this would neglect the supporting effect from the rest of the rectangular hollow section (webs and opposite flange). Another argument for assuming a finite plate is that crack propagation is a highly localised process and therefore the local geometry (two thin plates welded together) is of primary importance.

Assuming a crack propagating in a finite plate complicates the analysis. Firstly, the geometry factor F becomes dependent of the crack depth and secondly, there is a distinction between bending and tension. The first limitation prohibits using the closed form solution of Eq. 2.29. This is not a major obstacle, since involving the factor M_{k} to account for the stress concentrations at the weld toe requires numerical integration, because M_{k} is a function of crack depth in both cases, finite and infinite plate.

Semi-elliptical surface cracks with different a/t ratios in a rectangular hollow section (40×60 mm cross section with a wall thickness $t = 3$ mm) have been analysed to justify the assumption of a finite plate. The fracture analysis program FRANC3D was employed for this purpose [104, 105]. FRANC3D uses the displacement output of a boundary element program called BES. Both programs are developed by the Cornell Fracture Group at Cornell University. The geometry model and the boundary element mesh at and near the crack are shown in Fig. 5.19. The obtained geometry factors are plotted in Fig. 5.20 together with the Newman and Raju solution for a crack in a finite plate [68].

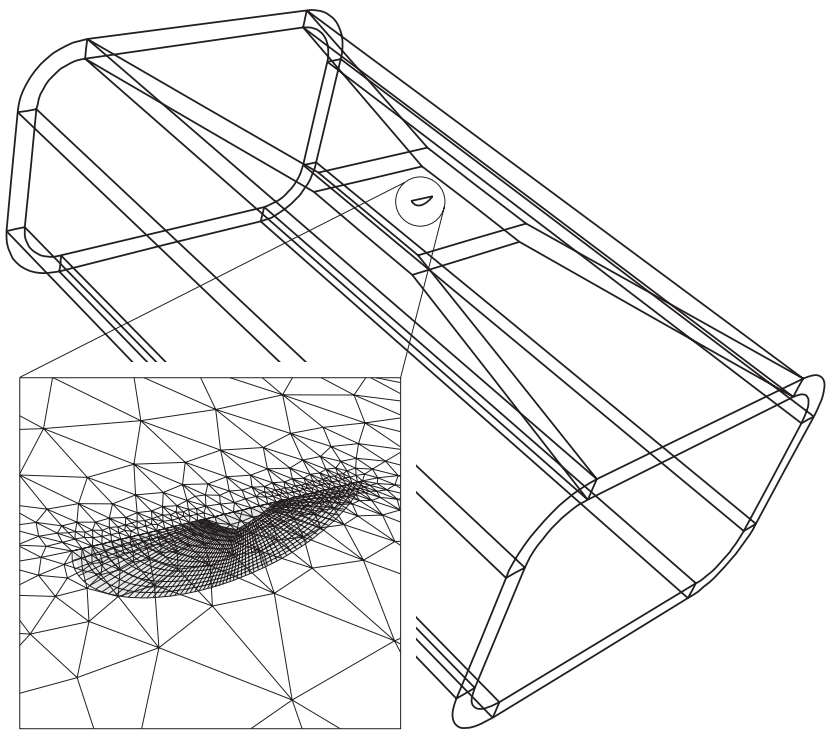

Figure 5.19: FRANC3D geometry model and boundary element mesh at and near the crack.

Although there is no perfect agreement between the equation and the Franc3D results, both have similar behaviour, i.e., the wall thickness is the significant parameter and the overall geometry (hollow section) is of minor importance. Therefore, the thickness parameter in the F and M_{k} equations was set to 3 mm within all analyses.

5.5.3 Tension or bending loading

The 4-point bending loading gives a linear stress distribution in the cord, see Fig. 5.21. However, as the crack propagates only through the flange, the stress distribution in the flange is of interest. The stress decreases from $\sigma_{\max}$ at the outer surface of the flanges to σ_{i} at the inner surface, where the relation between

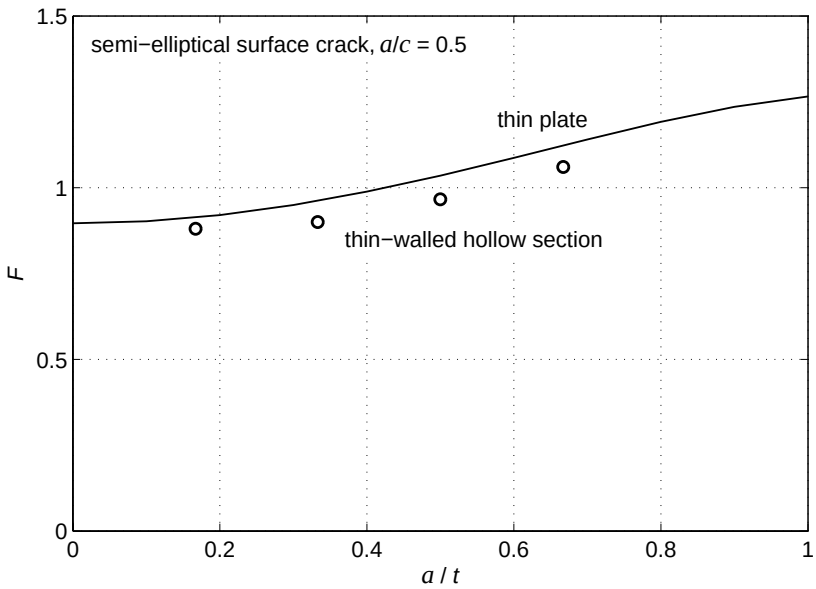

Figure 5.20: Geometry factor F for a semi-elliptical surface crack ($a/c = 0.5$) in a rectangular hollow section compared to F in a thin plate [68].

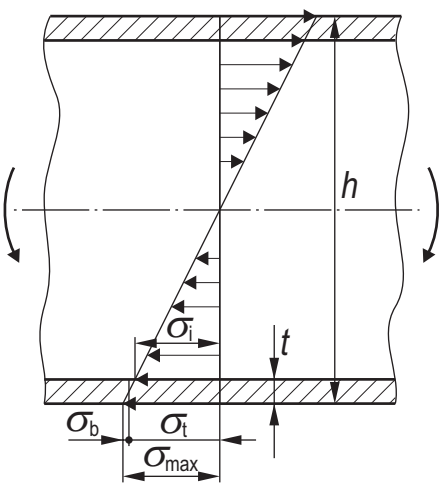

Figure 5.21: Nominal bending stress distribution in a thin-walled, hollow section beam, illustrating the almost uniform tension/compression ruling in flanges.

$\sigma_{\max}$ and σ_{i} can be expressed as

$$\sigma_{\mathrm{i}} = \left(1 - 2\frac{t}{h}\right)\sigma_{\max}\,. \tag{5.18}$$

Inserting the actual dimensions ($t = 3$ mm, $h = 40$ mm) it is seen that the stress decreases by only 15 % through the thickness of a flange. Dividing the stress in the flanges into a tension and a bending component gives

$$\sigma_{\mathrm{t}} = \left(1 - \frac{t}{h}\right)\sigma_{\max} = 0.925\sigma_{\max}\,, \tag{5.19}$$

$$\sigma_{\mathrm{b}} = \frac{t}{h}\sigma_{\max} = 0.075\sigma_{\max}\,. \tag{5.20}$$

Superposition leads to the stress intensity factor

$$K = K_{\mathrm{t}} + K_{\mathrm{b}} = (0.925F_{\mathrm{t}} + 0.075F_{\mathrm{b}})\,\sigma\sqrt{\pi a}\,. \tag{5.21}$$

It is seen that the tension component dominates, which is even amplified due to $F_{\mathrm{t}} > F_{\mathrm{b}}$. As a consequence it is assumed that the upper part (flange) of the box section is subjected to uniform tension with $S = S_{\max}$. This assumption makes the loading slightly more severe since the crack is assumed to propagate through a constant and not a decreasing stress field.

5.5.4 Crack shape, initial and final crack depth

Starting from some defect at the weld toe, a semi-elliptical crack propagates, as the experiments have shown, mainly in the thickness direction [77], i.e., through the upper flange. Only after having penetrated the flange, the crack propagates rapidly along the weld toe. It seems, therefore, straightforward to assume the fatigue life being covered by the propagation of a semi-elliptical surface crack, especially since most of the life is spent while the crack is short.

The initial a/c ratio has been set to 0.5. An initial crack depth of $a_{\mathrm{i}} = 0.05$ mm was assumed, since this is just below the resolution limit of the replica method used for weld geometry (and possible weld defects at the fusion line) measurements [32]. The final crack depth was set to $a_{\mathrm{f}} = 2.85$ mm which corresponds to 95 % of the wall thickness. It must be mentioned that the predicted fatigue life is relatively insensitive to the choice of a_{i}, since the parameter a^* levels the effect of the initial crack depth, as long as a_{i} is smaller than or of about the same size as a^*. The final crack length is not very important, since most of the life is spent while the crack is short.

The influence of the above assumptions is studied more closely in Section 5.5.7.

5.5.5 The factors F and M_{k}

The geometry factor F was calculated from the set of equations proposed by Newman and Raju [68], which is given in Appendix B.2.

Bowness and Lee [67] derived a set of equations to calculate M_{k} for a welded T-joint with a non-load-carrying weld. Those equations are based on finite element

analyses of a "welded" joint made from plates, see Fig. B.2. From the four sets of equations they have derived, the set for membrane load and zero weld toe radius was chosen. The membrane load, since the load in the flange is almost pure tension, cf. Section 5.5.3 and the zero weld toe radius because Bowness and Lee argue that the equations derived with zero weld toe radius, referred to as "as welded condition", are suited for cases where the weld toe was not ground. In addition a small cold lap would practically remove any weld toe radius.

All equations are given in Appendix B.3, for both the deepest point and the points where the crack front intersects the component surface.

Computing the ratios $l/t \approx 5$ mm/3 mm $= 1.7$ and $a_\mathrm{i}/t = 0.05$ mm/3 mm $= 0.017$, it is seen that both are well within the M_k validity limits, Eq. B.5. A weld angle of $\theta = \pi/4$ was used throughout.

An interesting feature of the weld toe magnification factor is that in contrast to F, which becomes constant when $a/t \ll 1$, M_k varies rapidly as long as $a/t \ll 1$, hence, M_k is very sensitive to a/t. This is due to the fact that a given crack is "pushed" deeper into the non-linear stress peak as the thickness t becomes larger. Employing M_k, it is therefore not possible to neglect the effect of a finite plate width on ΔK by assuming t to be very large.

5.5.6 Results

Equation 5.11 was numerically integrated using Simpson's rule. Letting a semi-elliptical surface crack ($a/c = 0.5$) propagate from $a_\mathrm{i} = 0.05$ mm to $a_\mathrm{f} = 2.85$ mm, the S-N curves obtained are plotted in Fig. 5.22.

The predicted lines do not follow a straight line but are slightly curved. The line corresponding to batch 1 is concave when looking from below. This is due to the increasing negative effect of S_residual as ΔS decreases. The opposite is the case for the batch 2 line, which is convex when looking from below. The compressive residual stress causes the tensile part of the cycle to decrease when ΔS decreases. The limiting case, where the whole stress cycle is compressive, $\Delta S = |S_\mathrm{residual} - S_\mathrm{m}|$, is approached asymptotically. The curvature is hardly seen in Fig. 5.22, because of the limited ΔS range covered by the diagram.

As expected, using $a^* = 0.25$ mm gives shorter fatigue lives than $a^* = 0.11$ mm, see also Eq. 5.17 for further details. Since the initial crack depth chosen is very small, a^* tends to have a high impact on the result. It is clearly seen that the introduction of local stress ratios using Walker's equation leads to longer fatigue lives in the case of compressive residual stress at the weld toe (batch 2). The overall agreement between experimental and predicted curves is good. However, even though the "slopes" match slightly better than in case of the stress based S-N curves, the predicted "slopes" are still too steep. The slope mismatch may indicate the existence of a crack initiation phase, which is more pronounced at low stresses. The predicted curves are somewhat non-conservative. There may be several reasons for this shortcoming. Due to the joint geometry, the corners where the cracks are originated will be subjected to stress concentrations that are not included in M_k. Furthermore, the change in material properties resulting from the welding process (heat affected zone) has not been taken into account. A lower fatigue limit, e.g., due to lower tensile strength, would result in a larger

a^* and hence in shorter lives.

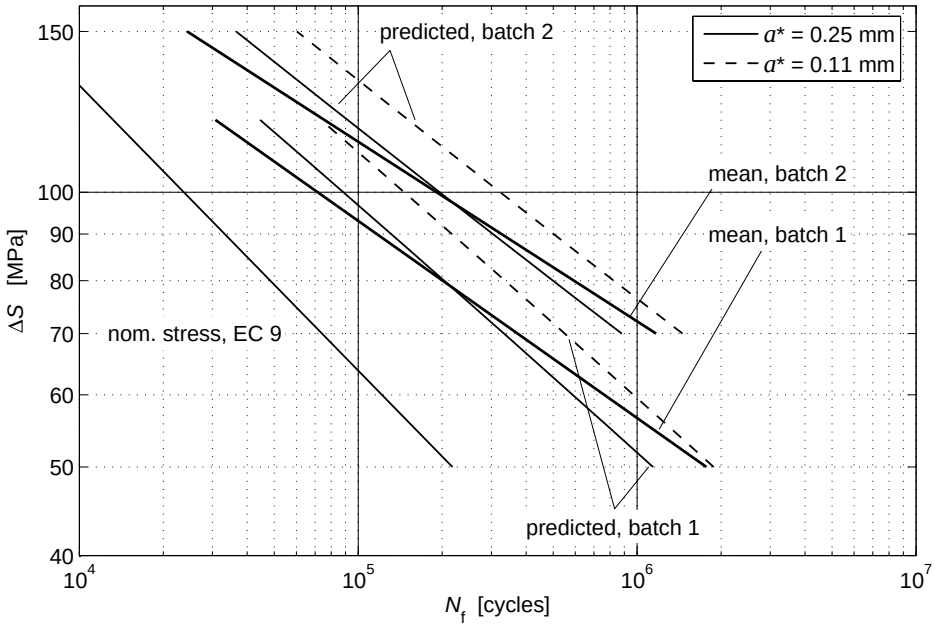

Figure 5.22: S-N curves for a semi-elliptical crack at the weld toe in a thin plate propagating from $a_\mathrm{i} = 0.05$ mm to $a_\mathrm{f} = 2.85$ mm and the mean test curves.

Evolution of the crack aspect ratio

When the crack aspect ratio, a/c, is treated as a variable in the analysis, it is, of course, interesting to see how it develops as the crack propagates. Figure 5.23 shows a plot of the a/c ratio as a function of crack depth obtained from the analysis.

Driven by the stress gradient the initially chosen aspect ratio rapidly approaches some sort of "natural" value of $a/c \approx 0.35$. Propagating away from the stress peak at the surface, a/c increases to approximately 0.4 when the crack has penetrated 20 % of the wall thickness. Throughout further propagation, a/c increases slowly towards 0.5.

5.5.7 Some sensitivity studies

In the previous analysis, the initial crack depth and the initial a/c ratio were "best-guess" values and such a situation is very likely to occur whenever the fatigue life of a welded component is to be assessed. It is therefore of primary importance to examine the sensitivity of the fatigue life prediction to those parameters. In addition, the crack propagation data present an obvious source of uncertainty, which will be examined as well.

Varying the initial crack depth

In a series of analyses the initial crack depth, a_i, has been varied from 0.1-0.5 mm. The predicted S-N curves, including the one obtained previously us-

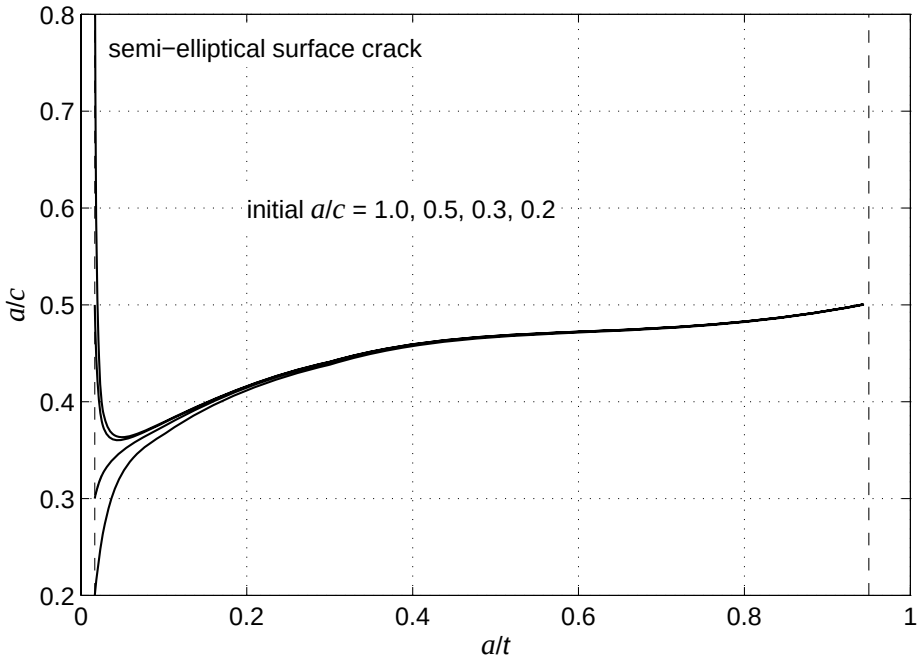

Figure 5.23: The a/c ratio of a crack propagating at a weld toe as a function of the crack depth.

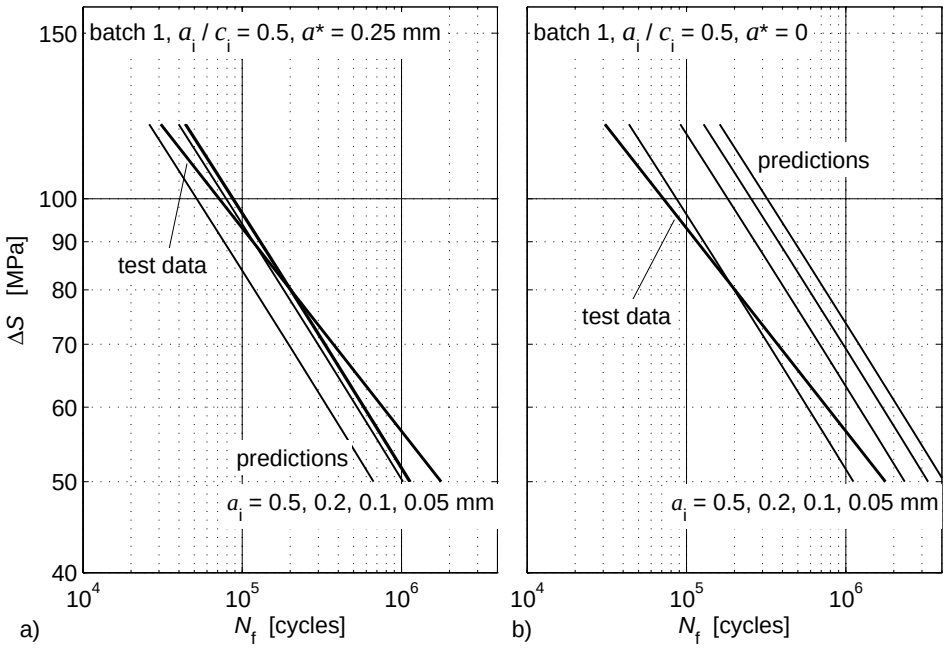

Figure 5.24: S-N curves for a semi-elliptical crack at the weld toe propagating from different initial crack depths a_i to $a_\mathrm{f} = 2.85$ mm: (a) $a^* = 0.25$ mm, (b) $a^* = 0$.

ing $a_i = 0.05$ mm, are plotted in Fig. 5.24a. The characteristic crack length $a^*(F = 1) = 0.25$ mm was used in all cases.

From Fig. 5.24a it is immediately seen that the effect of a_i is rather small. Only if $a_i = 0.5$, which is about $5a^*$, a notable impact on the fatigue life is found. The main reason for the small effect of a_i lies in the use of $a+a^*$ instead of a. This insensitivity with respect to a_i is rather welcome, since, as has been said before, the initial crack depth is usually unknown. The effect of a_i on predicted fatigue life when setting $a^* = 0$ is documented in Fig. 5.24b. The differences between the predictions are larger, but not quite as large as expected from the fact that a_i usually dictates the fatigue life. A reason for the relatively small impact of a_i may lie in the fact that the crack propagates initially relatively fast through the near surface region due to the high peak stress. This high peak stress counteracts to some extent the initially slow propagation of a crack in a plate.

Varying the a/c ratio

In order to investigate the effect of the initial a/c ratio, $a/c = 0.2, 0.3, 0.5$ and 1.0 were analysed. The predicted S-N curves are plotted in Fig. 5.25. It is seen that the crack shape has a very small impact on fatigue life. Comparing Figs. 5.25a and 5.25b it is found that the small impact of the initial a/c ratio is not due to a^*.

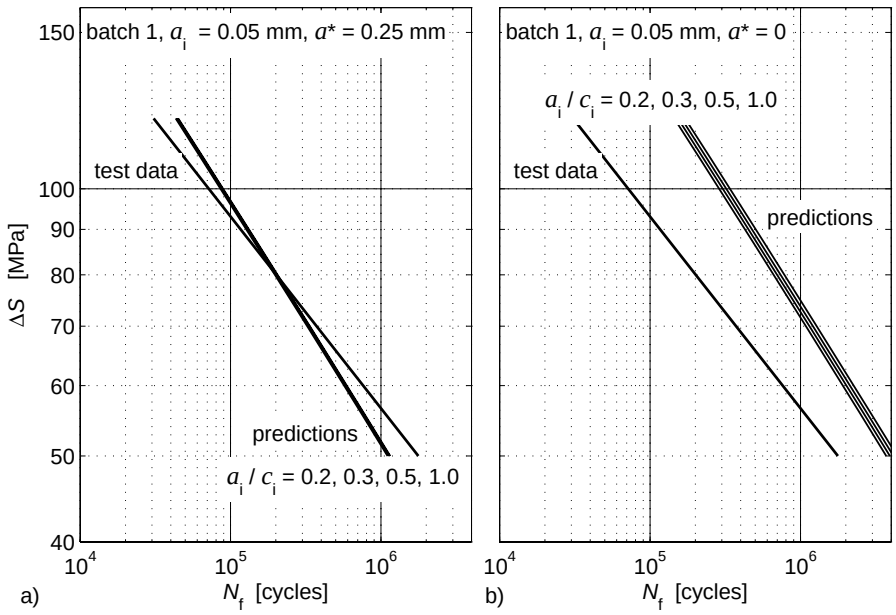

Figure 5.25: S-N curves for a semi-elliptical crack at the weld toe propagating from $a_i = 0.05$ mm to $a_f = 2.85$ mm, assuming different initial a/c ratios: (a) $a^* = 0.25$ mm, (b) $a^* = 0$.

The main reason for the small effect of a/c on the fatigue life is the fact that a/c rapidly approaches a value of approximately 0.35, see Fig. 5.23. Already from this figure it could be guessed that the initial crack aspect ratio plays only

a minor role. The reason why the initial a/c is that unimportant is because only a relatively small part of the fatigue life is spent before $a/c \approx 0.35$ is reached.

Variability and availability of crack propagation data

Having reliable material data is crucial when carrying out analyses. Hudson and Seward [106] and Hudson and Ferrainolo [107] have compiled a compendium of sources of fatigue crack propagation and fracture toughness data for a wide range of metallic materials. When looking for crack propagation data of aircraft application aluminium alloys (2000 and 7000 series), sources are quite frequent, whereas data for alloys used in automotive structures (5000 and 6000 series) are rare. Often data are published in the report series of certain institutions (e.g. NASA, AFML) and may not be easily available from all libraries. Another problem arises from the existence of different crack propagation laws. Since they usually use different constants, the constants one may look for are certainly not given, if any constants are given at all. Therefore, the constants must often be estimated from $\mathrm{d}a/\mathrm{d}N$ versus ΔK plots which especially in the case of journal articles are often small and of poor quality. In addition, estimating the required data from a simple visual curve fit will be subjective, i.e., it will give different results when carried out by different persons. It is obvious that due to such error sources the progress achieved by more fine tuning of the models may be in vain.

Since crack propagation data for the 6082-T6 aluminium alloy are rare, the data for the 7075-T6 aluminium alloy, see Tables 3.1 and 5.10, were used to evaluate the variation in the fatigue life resulting from variations in documented crack propagation data. Carrying out this sensitivity study on an aluminium alloy different from 6082-T6 should not be a serious limitation, since the sources of the scatter should be relatively independent of the material.

The data in Table 3.1 are given at different stress ratios. Therefore, the constants C have been transformed to $R = 0$ using Eq. A.6 with $\gamma(R > 0) = 0.63$ and $\gamma(R < 0) = 0$, see Section 3.3.3. In Table 5.10 both original data and transformed constants C are given.

Letting a semi-elliptical crack ($a_\mathrm{i}/c_\mathrm{i} = 0.5$) propagate at a weld toe from $a_\mathrm{i} = 0.05$ mm to $a_\mathrm{f} = 2.85$ mm, using the data from Table 5.10, fatigue lives at three different stress levels were obtained. Due to the large amount of data only maximum and minimum fatigue life predictions, $N_\mathrm{f,max}$ and $N_\mathrm{f,min}$, respectively, mean value, $\bar{N}_\mathrm{f}$, standard deviation, s, and the factor $f_\mathrm{N} = N_\mathrm{f,max}/N_\mathrm{f,min}$ have been tabulated in Table 5.11. This was done at three different stress levels.

From the large difference between $N_\mathrm{f,max}$ and $N_\mathrm{f,min}$ as well as from the standard deviation or the factor f_N it is seen that the fatigue lives predicted using the different crack propagation data show a large variation. These variations overshadow the rather small variations obtained from varying a_i or the initial a/c ratio. This result highlights the importance of good and reliable material data.

Table 5.10: Paris constants (C and m) for the aluminium alloys 7075-T6 and the constant C transformed to $R = 0$ using Walkers equation with $\gamma(R > 0) = 0.64$ and $\gamma(R < 0) = 0$.

Source	R	C (m/cycle, MPa$\sqrt{\text{m}}$)	m	$C(R = 0)$ (m/cycle, MPa$\sqrt{\text{m}}$)
Broek and Schijve [84]	0.66	7.00×10^{-11}	4.20	1.37×10^{-11}
	0.57	1.00×10^{-10}	3.80	3.15×10^{-11}
	0.50	2.00×10^{-11}	4.30	6.84×10^{-12}
	0.38	7.00×10^{-11}	3.80	3.64×10^{-11}
	0.29	2.00×10^{-10}	3.30	1.33×10^{-10}
	0.17	8.00×10^{-11}	3.40	6.37×10^{-11}
	0.06	3.00×10^{-11}	3.70	2.76×10^{-11}
Bu and Stephens [85]	0.50	9.17×10^{-11}	3.64	3.69×10^{-11}
	0.05	1.25×10^{-11}	3.99	1.16×10^{-11}
	-1.00	2.03×10^{-12}	3.61	2.47×10^{-11}
Dowling [12]	0.00	2.71×10^{-11}	3.70	2.71×10^{-11}
DTDH [87]	0.70	6.95×10^{-11}	3.69	1.40×10^{-11}
	0.33	1.77×10^{-10}	3.00	1.14×10^{-10}
	0.00	4.37×10^{-11}	3.21	4.37×10^{-11}
	-0.33	1.47×10^{-11}	3.40	3.87×10^{-11}
	-0.60	3.89×10^{-12}	3.49	2.00×10^{-11}
	-1.00	4.41×10^{-12}	3.32	4.40×10^{-11}
Durán et al. [88]	0.70	1.04×10^{-10}	3.83	1.97×10^{-11}
	0.10	1.30×10^{-10}	3.59	1.13×10^{-10}
Eurocode 9 [5]	0.10	8.65×10^{-11}	3.49	7.57×10^{-11}
Fleck and Anderson [89]	0.75	3.60×10^{-10}	3.29	6.96×10^{-11}
	0.50	2.55×10^{-10}	3.06	1.18×10^{-10}
	0.10	1.65×10^{-10}	3.00	1.47×10^{-10}
Hudson [90]	0.80	1.32×10^{-10}	4.00	1.30×10^{-11}
	0.50	4.14×10^{-11}	3.88	1.57×10^{-11}
	0.33	8.30×10^{-11}	3.50	5.01×10^{-11}
	0.00	3.40×10^{-11}	3.56	3.40×10^{-11}
	-0.33	1.35×10^{-11}	3.58	3.74×10^{-11}
	-0.60	6.14×10^{-12}	3.58	3.30×10^{-11}
	-0.70	1.69×10^{-12}	3.87	1.31×10^{-11}
	-1.00	3.24×10^{-12}	3.59	3.90×10^{-11}
Wu et al. [91]	0.50	1.96×10^{-10}	3.40	8.39×10^{-11}
	0.00	3.22×10^{-11}	3.56	3.22×10^{-11}
	-1.00	8.03×10^{-12}	3.48	8.95×10^{-11}

Table 5.11: Maximum and minimum predicted fatigue life, $N_{\mathrm{f,max}}$ and $N_{\mathrm{f,min}}$, respectively, mean value, $\bar{N}_{\mathrm{f}}$, standard deviation, s, and the factor $f_{\mathrm{N}} = N_{\mathrm{f,max}}/N_{\mathrm{f,min}}$.

$\Delta\sigma$ [MPa]	$N_{\mathrm{f,max}}$ [cycles]	$N_{\mathrm{f,min}}$ [cycles]	$\bar{N}_{\mathrm{f}}$ [cycles]	s [cycles]	f_{N}
50	1 391 000	197 000	679 000	313 000	7.1
75	401 000	59 000	199 000	83 000	6.8
100	164 000	24 000	81 000	32 000	6.8

5.6 Crack propagation using the local stress distribution

There are several reasons why it is tempting to apply another crack propagation approach. First of all, the M_{k} equations proposed by Bowness and Lee were developed for a joint made of plates, not hollow sections. Comparing the results with an other method provides a means of verification. Furthermore, the local stress distribution is easily available from the analyses done in context with the effective notch stress approach, see Section 5.4. The complete procedure to calculate F from the local stress distribution, including the numerical integration of Paris' law, was already programmed by Huth [71].

Figure 5.26 shows the through-thickness distribution of the maximum principal stress (point B in Fig 5.14a), as well as the representation through the following 5th order polynomial

$$\frac{\sigma_1}{S_{\max}} = -5.79\xi^5 + 19.44\xi^4 - 26.17\xi^3 + 17.90\xi^2 - 7.59\xi + 2.58\,. \tag{5.22}$$

Applying Eq. 2.45, the coefficients B_n are found to:

$$\begin{aligned}
B_0 &= -5.79\alpha^5 + 19.44\alpha^4 - 26.17\alpha^3 + 17.90\alpha^2 - 7.59\alpha + 2.58\\
B_1 &= 28.95\alpha^5 - 77.76\alpha^4 + 78.51\alpha^3 - 35.80\alpha^2 + 7.59\alpha\\
B_2 &= -57.90\alpha^5 + 116.64\alpha^4 - 78.51\alpha^3 + 17.90\alpha^2\\
B_3 &= 57.90\alpha^5 - 77.76\alpha^4 + 26.17\alpha^3\\
B_4 &= -28.95\alpha^5 + 19.44\alpha^4\\
B_5 &= 5.79\alpha^5
\end{aligned}$$

The S-N curve in Fig. 5.27 is obtained by letting a semi-elliptical surface crack at the weld toe propagate from $a_{\mathrm{i}} = 0.05$ mm to $a_{\mathrm{f}} = 2.1$ mm ($\alpha = 0.017\ldots0.7$). The assumed final crack depth had to be reduced to 2.1 mm to stay within the validity limit of the method ($\alpha \leq 0.7$). The characteristic crack depth $a^* = 0.25$ mm was used, and as long as the crack was shorter than $\alpha = 0.1$ the F_n value for $\alpha = 0.1$ was assumed. The crack propagation data given at $R = 0.1$, see Table 5.3, were transformed to $R = 0.5$, which, according to Table 5.2, is realistic for batch 1. The transformation was done using Walker's equation with $\gamma = 0.6$.

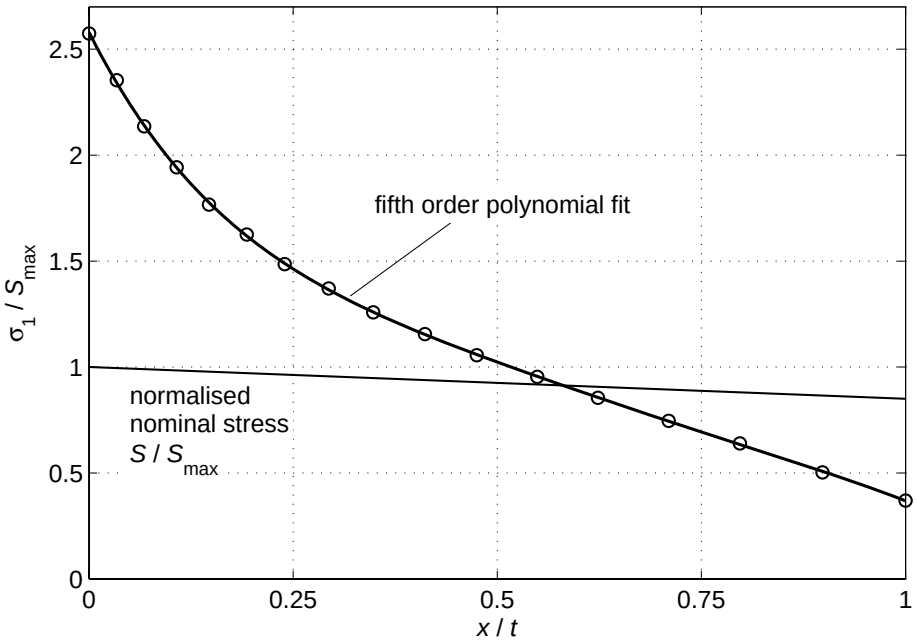

Figure 5.26: Through-thickness distribution of the maximum principal stress at the weld toe (point B) from FE analysis and its approximation by a 5th order polynomial (Eq. 5.22).

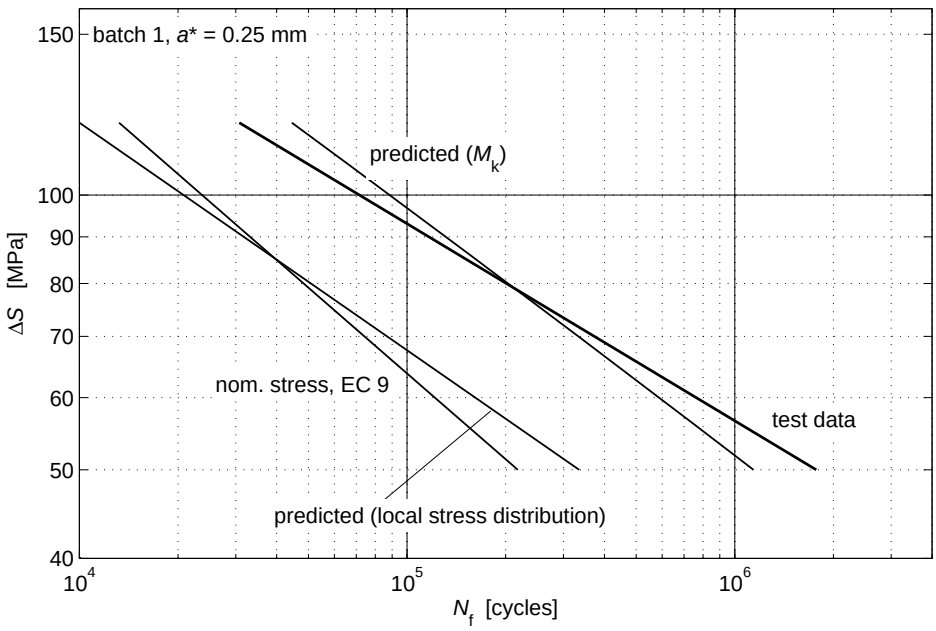

Figure 5.27: S-N curves for a semi-elliptical crack at the weld toe.

For comparison, the nominal stress S-N curve from Eurocode 9 and the one obtained in Section 5.5.6 using the weld toe magnification factor, M_k, are included in Fig. 5.27. It is seen that the fatigue life predicted using the local stress distribution is conservative and similar to the nominal stress S-N curve from Eurocode 9. Some of the deviation between the two crack propagation approaches is certainly due to the use of the maximum stress all along the surface when applying the local stress distribution, which makes is more conservative. The analysis applying the M_k factor uses the nominal stress and excludes some of the stress concentration due to the joint geometry (hollow section, corner). In the real T-joint the crack propagates into a decreasing stress field along the surface, i.e., it will grow more slowly.

5.7 A comparison

Having applied all fatigue life prediction methods presented in Chapter 2 to the same structure, the results will be compared in this section. In Fig. 5.28 the S-N curves obtained with the different approaches and the experimental curve for batch 1 are given, where the nominal stress curve is the one obtained from Eurocode 9.

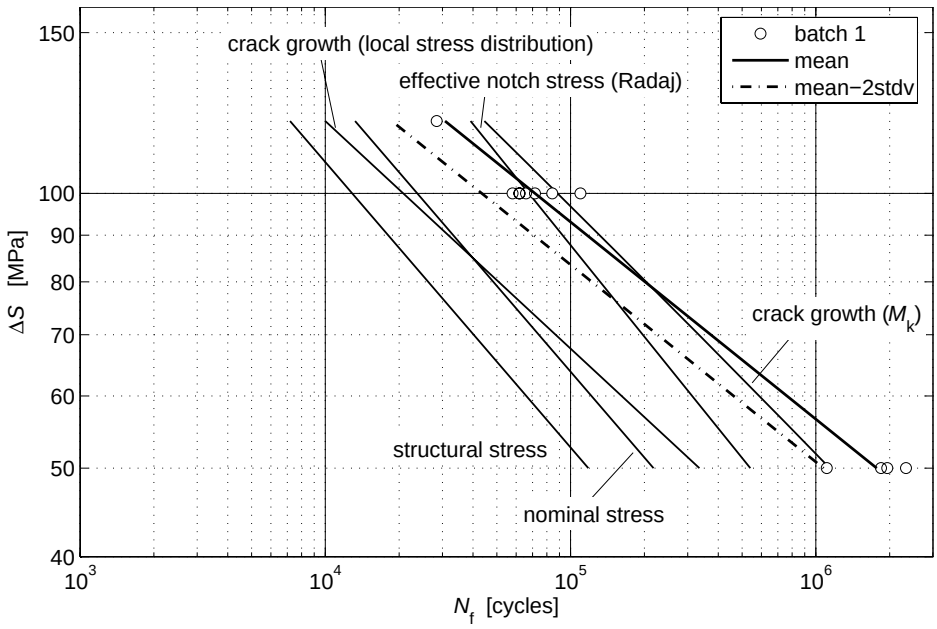

Figure 5.28: S-N curves obtained with the different approaches and the experimental curve for batch 1. Structural hot spot stress and nominal stress results are from Eurocode 9

It should be noted that apart from the two crack propagation approaches, which compare directly to the mean experimental curve, the other predictions must be compared with the mean-2stdv curve. The predicted S-N curves, especially from the stress based approaches, have a steeper slope than the experimental curves.

The crack propagation approach using M_k and the effective notch stress approach (Radaj) yield S-N curves that compare best with the experimental results. The prediction using the notch sensitivity (not included in Fig. 5.28) is slightly non-conservative and the agreement with the experimental curve is not as good as the agreement between the effective notch stress approach (Radaj) and the experimental results.

The nominal stress and the structural hot spot stress as well as the crack propagation approach using the local stress distribution give results conservative with factors of 2-5, 4-10 and 2-3 in life, respectively.

An explanation for the different results from the crack propagation analyses using the M_k factor or the local stress distribution, is found in the actual stress used and the stress gradient along the weld toe. Shorter fatigue lives are predicted using the local stress distribution because the highest stress is used throughout the crack propagation. However, a crack starting at the most highly stressed point will grow into a less stressed region, i.e., it will grow more slowly than assumed in the analysis. On the other hand, the equation used to calculate M_k does not account for the shear lag and the inhomogeneous stress distribution due to the hollow sections, thus a longer lifetime is predicted.

CHAPTER 6

A welded T-joint subjected to transverse bending

After having applied the various fatigue assessment methods to a welded T-joint subjected to 4-point bending, another load case was studied. Under 4-point bending, the weld is non-load carrying. Therefore, a load case where the load is transmitted through the weld was looked for. Eventually it was decided to investigate the T-joint subjected to transverse bending of the brace, as shown in Fig. 6.1. Loading the joint in such a way is obviously not a good design, since severe stress concentrations are produced. Nevertheless, from a research point of view, this load case is of interest [102, 108]. Another reason for applying this load case is that, due to the approximately 3 mm deep crack-like root gap, failure from the root side was expected.

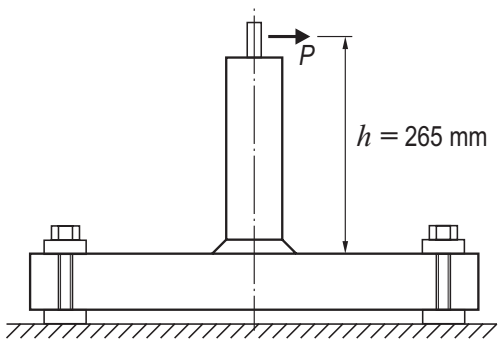

Figure 6.1: T-joint subjected to transverse bending of the brace.

6.1 Fatigue testing

6.1.1 Description

The specimens were welded according to the welding procedure specification given in Appendix D. Altogether thirteen specimens were tested. The specimens were divided into two groups and each group was tested at a different load level. The applied nominal stress ranges in the chord at the weld toe are given in Table 6.1. All specimens were subjected to constant amplitude loading at a stress ratio of $R = 0.1$. The specimens were arranged vertically and clamped to a rigid plate, see Fig. 6.2.

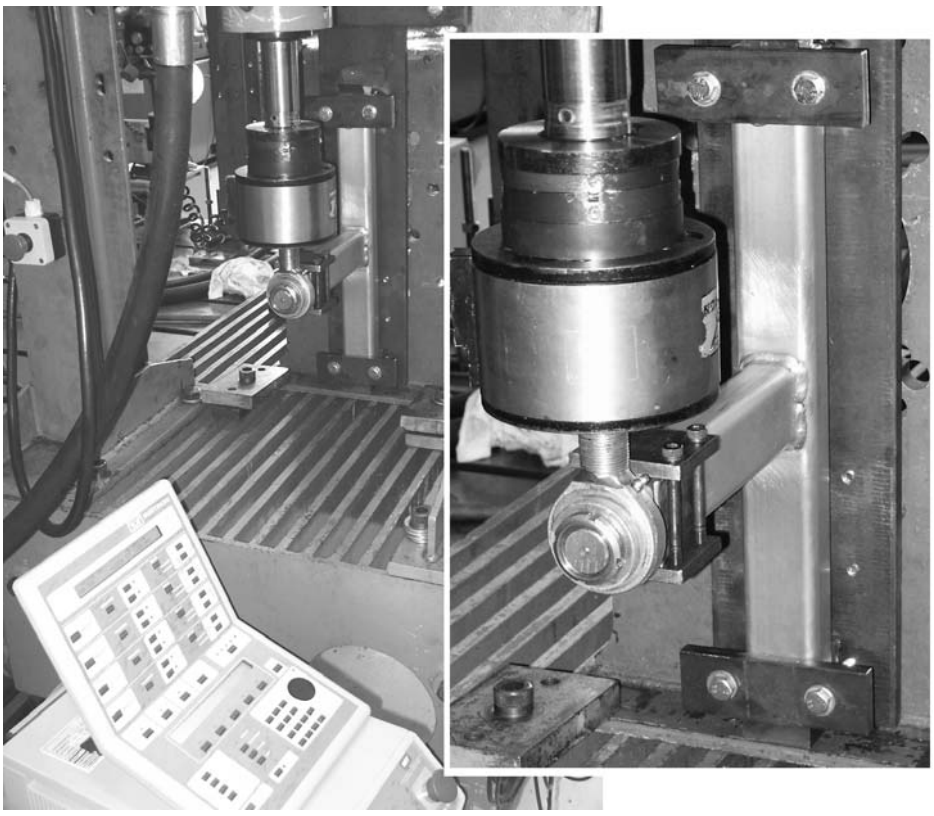

Figure 6.2: T-joint made from rectangular hollow sections.

To apply the load, a bolt, that was cylindrical at one end and with a cross section fitting exactly into the brace (50 mm deep) at the other end, was inserted into the brace and clamped. The cylindrical part of the bolt was mounted to a spherical hinge, which in turn was attached to the load cylinder. The hinge allowed the brace to bend freely. The experiments were carried out using load control, thus the load was kept constant even when the crack becomes prominent. The tests were stopped when the maximum displacement of the loading point had increased by 4 mm. By that time the crack had extended along the weld toe and around the "corners", see Fig. 6.3.

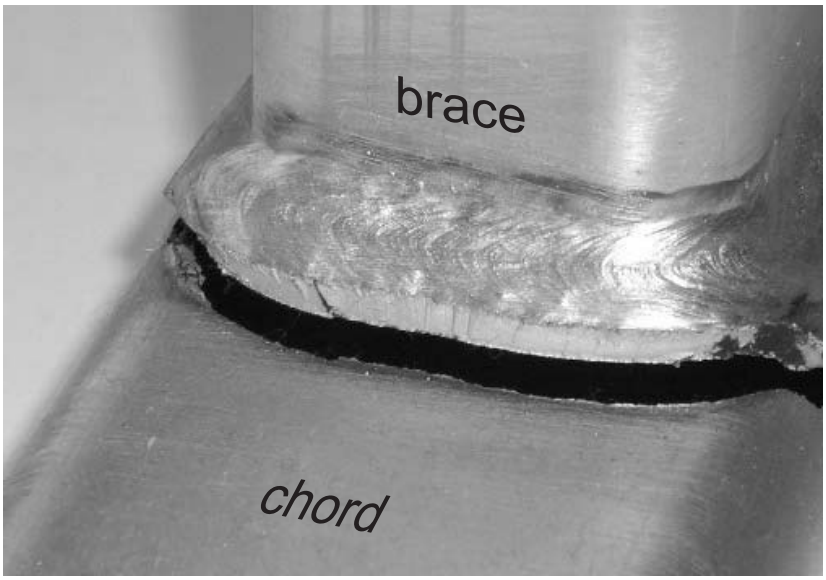

Figure 6.3: Typical crack at the time the test was concluded.

6.1.2 Calculating the nominal stress

As in the previous chapter, the fatigue life will be presented in form of nominal stress S-N diagrams, thus, the nominal stress must be calculated. Both ends of the chord are clamped, which makes the beam structure three times statically undetermined. However, making use of the symmetrical boundary conditions and some elementary beam cases, the problem can be treated quite effectively.

Applying the load P to the brace, cf. Fig. 6.4, the brace receives the bending moment

$$M(z_1) = Pz_1 \,. \tag{6.1}$$

With $z_1 = h = 265$ mm, $y = y_{\text{max,brace}} = 30$ mm for the left surface of the brace and $I_{\text{brace}} = 234\,660$ mm^4, see Appendix C, the maximum stress becomes

$$S_{\text{max,brace}} = \frac{Ph}{I_{\text{brace}}} y_{\text{max,brace}} = \frac{0.034}{\text{mm}^2} P \,. \tag{6.2}$$

Due to symmetry it follows that half of the bending moment $M(z_1 = h) = Ph$ is transferred to either side of the chord, see Fig. 6.4c. To obtain the complete bending moment distribution in the chord, it is assumed that one half of the chord is described by a cantilever beam subjected to $M_0 = Ph/2$. For the displacement of the free end of the beam to vanish, a transverse force, P_0, is required and its magnitude follows from:

$$\frac{M_0 l^2}{2EI_{\text{chord}}} - \frac{P_0 l^3}{3EI_{\text{chord}}} = 0$$

$$P_0 = \frac{3}{2}\frac{M_0}{l} \,. \tag{6.3}$$

From the equilibrium of moments and forces follow the reaction moment $M_{\text{A}} = M_0/2$ and the reaction force $P_{\text{A}} = P_0$, respectively. Now, the bending moment in

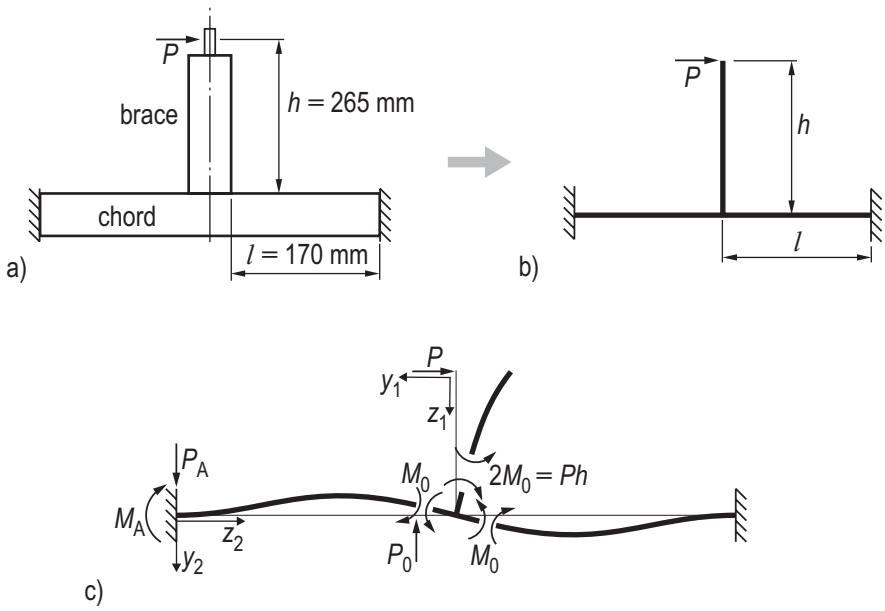

Figure 6.4: Idealisation and nomenclature of the T-joint subjected to transverse bending of the brace.

the chord from the left end to the junction with brace is found to be

$$M(z_2) = \frac{M_0}{2}\left(1 - 3\frac{z_2}{l}\right) . \tag{6.4}$$

The bending moment distribution of the complete T-joint is sketched in Fig. 6.5

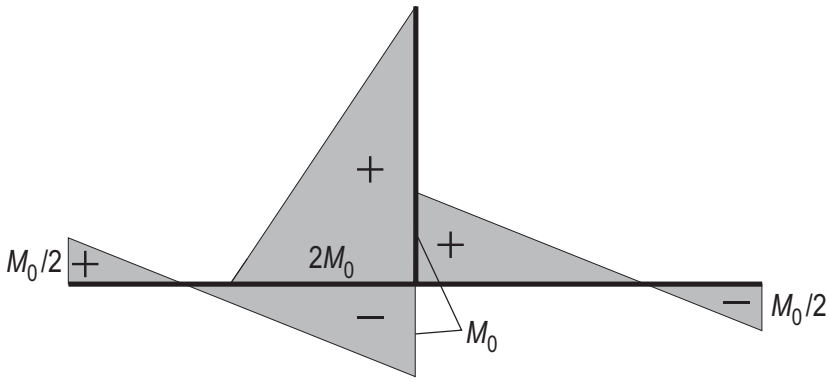

Figure 6.5: bending moment distribution in the T-joint.

With the stress from the axial load $S_{\mathrm{P}} = P/2A$ (tension in the left part of the chord), the total nominal stress in the chord is found from adding the stresses due to the bending moment and the axial force. With $M(z_2 = l) = -M_0 = -ph/2$, $y = y_{\mathrm{max,chord}} = -20$ mm for the upper surface of the chord, $A = 520\ \mathrm{mm}^2$, $I_{\mathrm{chord}} = 125\,830\ \mathrm{mm}^4$, the maximum tensile stress in the chord becomes

$$S_{\mathrm{max,chord}} = \left(\frac{1}{2A} - \frac{h}{2I_{\mathrm{chord}}} y_{\mathrm{max,chord}}\right) P = \frac{(0.001 + 0.021)}{\mathrm{mm}^2} P . \tag{6.5}$$

It is immediately seen that the axial load contributes with 5 % only. Figure 6.6 compares the stress distribution along the chord from beam theory (Eq. 6.5) with the result from a finite element analysis, see Section 6.3. The FE result follows the beam theory nicely up to $z_2/l \approx 0.5$. Thereafter the stress in the chord deviates from the beam theory result. This deviation is due to local buckling in the hollow section and the stress concentration from the weld.

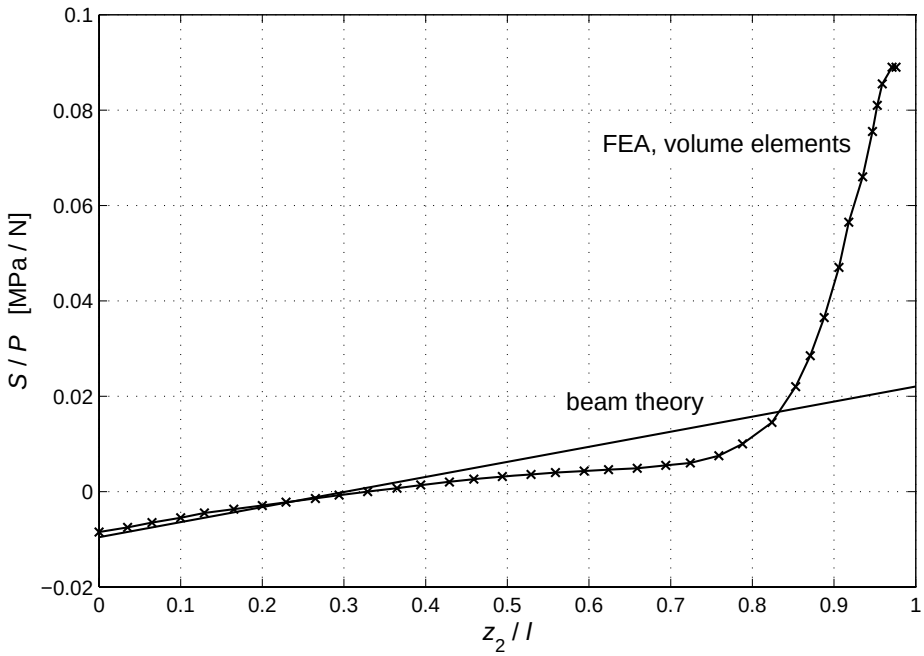

Figure 6.6: Axial stress distribution along the centre line of the upper surface of the chord. Finite element analysis (cf. Section 6.3) compared with beam theory (Eq. 6.5).

Comparing the maximum nominal stress in the brace, Eq. 6.2, with the maximum nominal stress in the chord, Eq. 6.5, it is found that the maximum stress in the brace is 1.5 times its equivalent in the chord. From this evaluation of nominal stress the failure could be expected in the brace. Thus, if the joint fails in the chord, the failure will be related to the local geometry.

6.1.3 Test results

The obtained fatigue lives are listed in Table 6.1 and the Basquin constants of the fitted curve, together with the standard deviation of $\log N_\mathrm{f}$, $s_{\log N_\mathrm{f}}$, are given in Table 6.2. Figure 6.7 shows both the test results and the fitted mean S-N curve. For comparison, the mean S-N curve from the 4-point bending tests (batch 1) is shown in Fig. 6.7 too.

It was found that the crack propagated from the weld toe of the chord, c.f. Fig 6.3, in all specimens. This behaviour was rather unexpected since the root gap, cf. Fig. 5.4, presents a crack-like defect of about 3 mm depth, which led to the presumption that a crack would propagate from the root. This, however, did

not happen. The crack always started at one of the radial parts along the weld toe, see Fig. 5.1 and propagated into the chord.

Table 6.1: Loading conditions and fatigue lives.

Specimen no.	$P_{\min}$ [kN]	$P_{\max}$ [kN]	ΔP [kN]	ΔS [MPa]	N_f [cycles]	comments test no.	strain gauges
1	0.11	1.1	1.0	22.0	504 000	6.1	—
2	0.11	1.1	1.0	22.0	1 000 000	6.2	—
3	0.11	1.1	1.0	22.0	2 220 000	6.3	—
4	0.11	1.1	1.0	22.0	248 000	6.5	—
5	0.11	1.1	1.0	22.0	271 000	6.9	—
6	0.11	1.1	1.0	22.0	297 000	6.10	—
7	0.167	1.67	1.5	33.0	74 000	6.6	—
8	0.167	1.67	1.5	33.0	49 000	6.4	4x
9	0.167	1.67	1.5	33.0	49 000	6.7	—
10	0.167	1.67	1.5	33.0	121 000	6.8	—
11	0.167	1.67	1.5	33.0	63 000	6.12	6x
12	0.167	1.67	1.5	33.0	153 000	6.13	—
13	0.167	1.67	1.5	33.0	138 000	6.14	2x

Comparing the S-N curves from 4-point bending and transverse bending, it is seen that the fatigue live is reduced by a factor of approximately 150 in life in case of the transverse bending load case. This large reduction supports the statement at the beginning of this chapter that the transverse bending load case is not an optimal design. However, as pointed out earlier, the load case was applied in order to investigate the applicability of the various approaches to fatigue life predictions of aluminium load-carrying fillet welds.

Table 6.2: Constants in Basquin's law for transverse bending fatigue tests and the standard deviation, $s_{\log N}$.

	$1/b$	σ'_f [MPa]	A [cycles/MPa$^{1/b}$]	$s_{\log N_f}$
mean	-4.55	231	6.91×10^{11}	0.3
mean $- 2\, s_{\log N_f}$	-4.55	171	1.74×10^{11}	

6.1.4 Strain measurements

In order to get an indication of the load symmetry and monitor when and where a crack starts to propagate, single strain gauges with a gauge length of 7 mm were applied to three specimens (specimens 8, 11 and 13). Figure 6.8 illustrates the

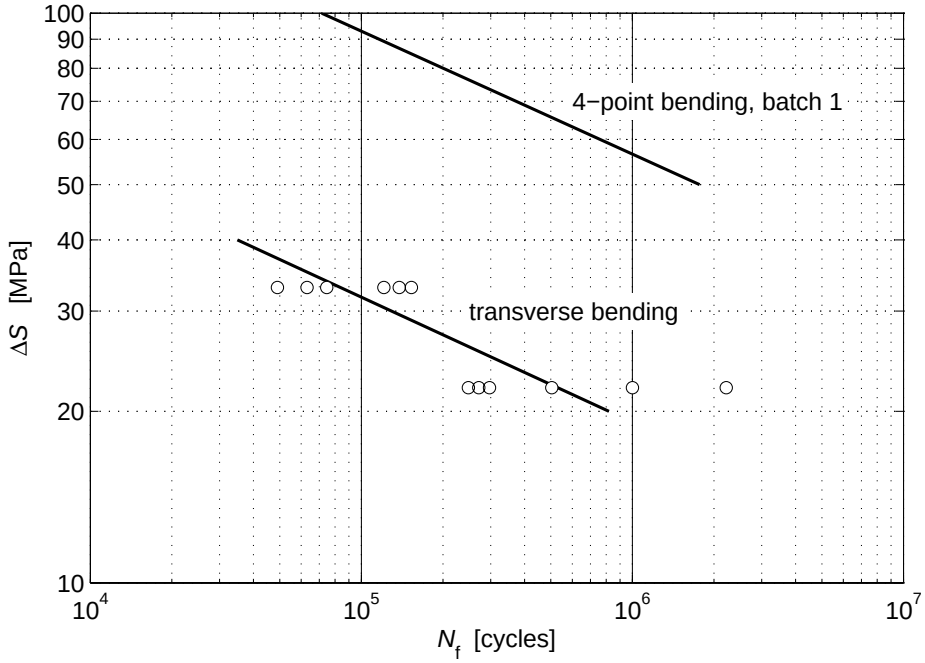

Figure 6.7: Experimentally found fatigue lives and the corresponding mean S-N curve.

location of the strain gauges. It must be noted that not all of the three specimens were equipped with all six strain gauges, see Table 6.1. The strain gauges sg1 through sg4 were to monitor the strain near the weld, whereas the remaining two strain gauges, sg5 and sg6, were to measure the strain undisturbed from the weld.

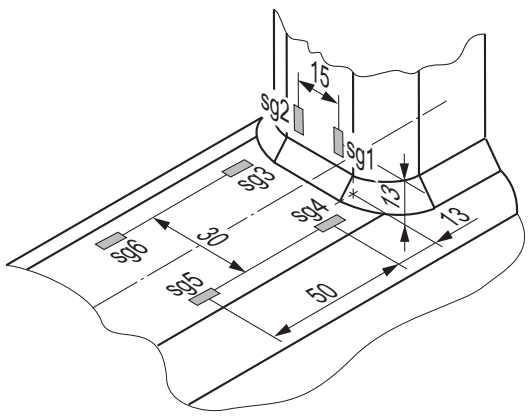

Figure 6.8: Strain gauge placement and notation.

Table 6.3: "Strain ratios" for specimens 8, 11 and 13.

	specimen no.		
"Strain ratios"	8	11	13
$\varepsilon_{\max,\mathrm{sg2}}/\varepsilon_{\max,\mathrm{sg1}}$	0.4	0.5	—
$\varepsilon_{\max,\mathrm{sg3}}/\varepsilon_{\max,\mathrm{sg4}}$	0.8	0.9	1.3
$\varepsilon_{\max,\mathrm{sg5}}/\varepsilon_{\max,\mathrm{sg6}}$	—	1.0	—

Figure 6.9 plots the maximum strain, $\varepsilon_{\max}$, recorded with strain gauges sg1 through sg4 on specimen 8 as a function of the number cycles. Theoretically, the recordings from sg1 and sg2 as well as from sg3 and sg4 should, because of symmetry, be identical as long as no considerable crack has developed. It is, however, immediately seen that they are not equal. The ratio $\varepsilon_{\max,\mathrm{sg2}}/\varepsilon_{\max,\mathrm{sg1}}$, which should be 1, is approximately 0.4 and $\varepsilon_{\max,\mathrm{sg3}}/\varepsilon_{\max,\mathrm{sg4}} \approx 0.8$. Returning

to Fig. 6.9, it is found that the strain recorded with sg4 starts to drop rapidly at approximately 15000 cycles, which indicates that the crack has become large enough to cause major changes in the load distribution. The strains at sg1 and sg4 are decreasing, whereas the strains obtained from sg2 and sg3 increase. At sg4, the strain even becomes negative, which may be explained by the release of tensile residual stresses.

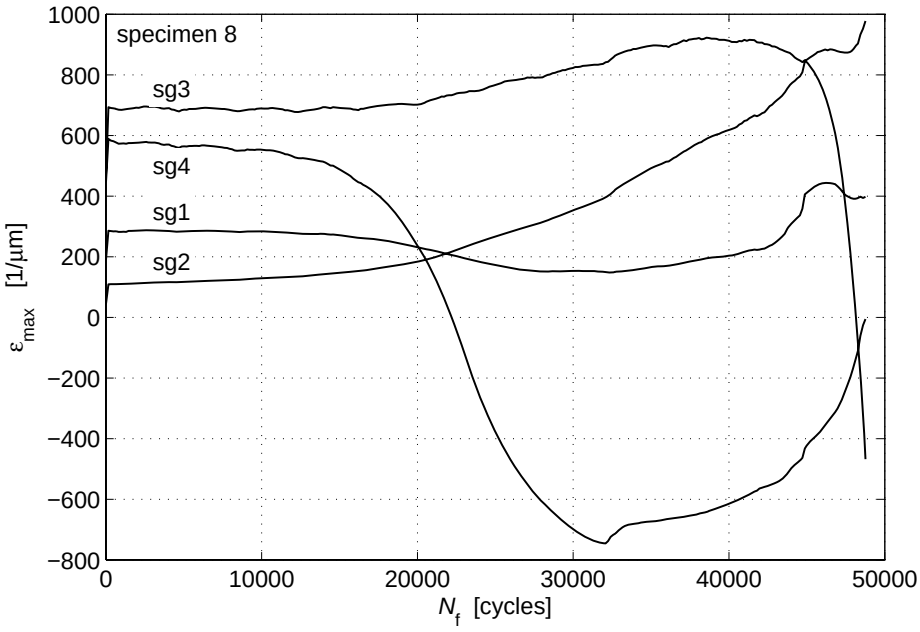

Figure 6.9: Maximum strain, $\varepsilon_{\max}$, as a function of the number cycles recorded with strain gauges sg1 to sg4 on specimen 8.

To investigate whether the large non-symmetry in the strain measurements is caused by non-symmetrical loading, non-symmetries in the weld geometry or erroneous measurements, two more specimens were equipped with strain gauges. Specimen 11 received six strain gauges where the additional strain gauges, sg5 and sg6, were placed on the chord far away from the weld toe to be undisturbed from the weld geometry, see Fig. 6.8. Two strain gauges, sg3 and sg4, were attached to specimen 13. In Table 6.3 "strain ratios" indicating the symmetry of the loading are listed. The pair of strain gauges sg5 and sg6 measure the same strain, hence a ratio of 1.0 is obtained. The other two strain gauge pairs, however, record large differences. This would suggest that the weld is the source of the non-symmetry. However, to become confident, a larger number of specimens equipped with all six strain gauges must be tested. In addition, two more strain gauges should be placed away from the weld on the brace. To trace the crack, smaller strain gauges should be placed closer to the expected crack initiation site. However, it is of course impossible to directly obtain information about the actual size of a crack with this method.

The strain measurements showed that the strain distribution along the weld toe is not symmetric as expected. Since the load cylinder and the specimens were thoroughly aligned, the lack of strain symmetry must be due to non-symmetries

in the weld. There might be some measurement error or a badly applied strain gauge. However, since both specimens 8 and 11 show a similar non-symmetry, this is not most likely.

Due to the higher strain measured at the sg3 side of the chord, the failure of specimen 8 could be expected to start from this side. This was not the case. The crack propagation started from the opposite side, which is clearly seen from the sg4 strain readings, cf. Fig. 6.9. This unexpected behaviour is probably caused by a larger initial defect or a more severe weld toe geometry at the sg4 side.

6.2 Nominal stress

Applying different design codes to the T-joint subjected to 4-point bending showed that the predicted S-N curves differ little from code to code. However, neither Eurocode 9 nor BS 8118 give a detail category suitable for the T-joint subjected to transverse bending of the brace. The experimental results for the 4-point bending load case and the transverse bending load case differ by a factor 3 in stress, cf. Fig. 6.7. Since the detail categories applicable for the 4-point bending loading range between 20 and 25, a detail category 8 would be suitable for the T-joint subjected to transverse bending of the brace. Such a low detail category does not exist in the standards mentioned above. Therefore, to be able to treat welded structures loaded similar to the T-joint discussed here, a detail category 8 should be considered to be included in the design standards.

6.3 Structural hot spot stress

After having applied the nominal stress approach, the structural hot spot stress approach is employed. Unfortunately, BS 8118 does not state structural hot spot stress design curves. Therefore, the curve has been taken from Eurocode 9. Since the structural hot spot stress detail categories in Eurocode 9 are distinguished by the member thickness only, the same design S-N curve (detail category 44) as for the 4-point bending tests applies. Thus, $\Delta\sigma_{\mathrm{C,hs}} = 44$ MPa. The structural hot spot stress S-N curve must be converted to nominal stress to be comparable with the experimental results and the nominal stress approach. This is done by means of the structural hot spot stress concentration factor, K_{hs}. Two finite element models were created to find the hot spot stress and hence K_{hs}. The first, which is a shell model combined with solid elements to represent the weld, did not give reasonable results near the weld. The geometry might be too complex to be adequately described by such a model. The second model, therefore, consisted entirely of volume elements (quadratic elements with reduced integration, C3D20R), see Fig. 6.10, with two elements through the wall thickness.

In addition to the finite element analysis, the following parametric equations, derived by van Wingerde [108] and contained in the IIW document [101], are employed as verification and also to find out whether or not the equations are

applicable to the given T-joint.

$$K_{\mathrm{hs}} = (0.952 - 3.062\beta + 2.382\beta^2 + 0.0228 \cdot 2\gamma) \times (2\gamma)^{(-0.69+5.817\beta-4.685\beta^2)}\, \tau^{0.75} \qquad \text{(line C)} \tag{6.6}$$

$$K_{\mathrm{hs}} = (-0.054 + 0.332\beta - 0.258\beta^2) \times (2\gamma)^{(2.084-1.062\beta+0.527\beta^2)}\, \tau^{0.75} \qquad \text{(line D)} \tag{6.7}$$

$$K_{\mathrm{hs}} = (0.39 - 1.054\beta + 1.115\beta^2) \times (2\gamma)^{(-0.154+4.555\beta-3.809\beta^2)} \qquad \text{(line E)}\,, \tag{6.8}$$

For a definition of β, γ and τ refer to Section 5.3.2. Lines C to E are defined in Fig. 6.11. Equations 6.6 to 6.8 are proposed for T-joints made from square hollow sections subjected to a transverse force on the brace [108]. The cross section of the brace was considerably smaller than the cross section of the chord.

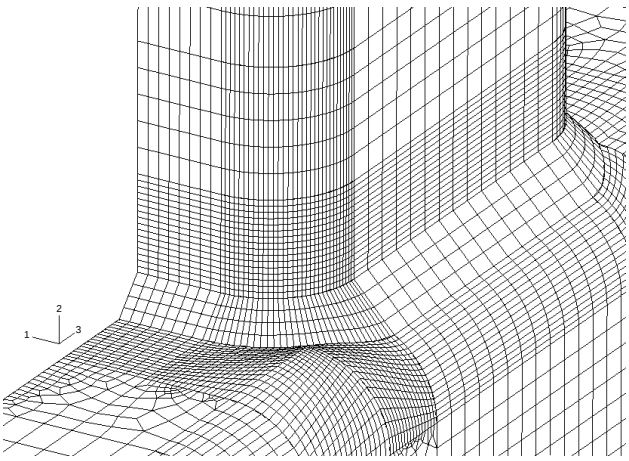

Figure 6.10: Finite element mesh near the weld of the T-joint modelled with volume elements.

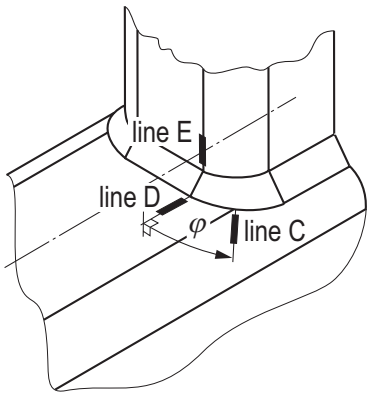

Figure 6.11: Definition of the lines along which the hot spot stress concentration factor was calculated.

The structural hot spot stresses and stress concentration factors along lines C, D and E, see Fig. 6.11, for the T-joint investigated in this work were established using linear extrapolation and the obtained values are listed in Table 6.4. From these values it is seen that the hot spot stress concentration factor from the FE analysis at line D is in good agreement with the value obtained from Eq. 6.7. Along line C the parametric equation (Eq. 6.6) predicts a 30 % larger K_{hs}. Finally, the finite element result and Eq. 6.8 differ most along line E, with Eq. 6.8 predicting a hot spot stress concentration factor that is four times larger than the one from the FE analysis. This deviation is most probably due to the differences in the geometry between the T-joint studied by van Wingerde [108] and and the T-joint investigated in this work.

In order to convert the structural hot spot stress S-N curve to nominal stress, using Eq. 5.5, $K_{\mathrm{hs}} = 8.9$ from the FE analysis was selected since it refers to

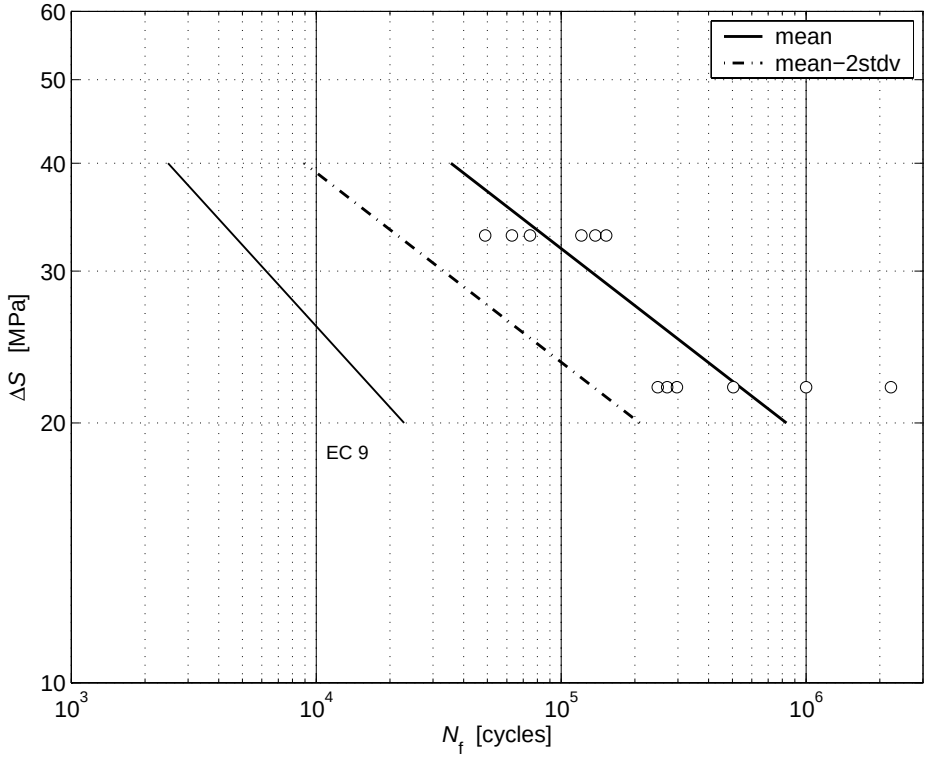

Figure 6.12: Experimental S-N curve compared to the structural hot spot stress design curve from Eurocode 9 [5] expressed in terms of nominal stress.

the actual joint. The resulting curve is plotted in Fig. 6.12. It is seen that the structural hot spot stress approach provides a conservative prediction. The conservatism is of the same magnitude as in the 4-point bending case, i.e., a factor 4-10 in life. Note that if the parametric equation (Eq. 6.6) for the derivation of the structural hot spot stress is used, the predictions are even more conservative.

Table 6.4: Hot spot stresses and stress concentration factors.

Line	$S_{0.4t}/P$ [MPa/N]	$S_{1.0t}/P$ [MPa/N]	σ_{hs}/P [MPa/N]	S/P [MPa/N]	K_{hs} (FEA)	K_{hs} (Eqs. 6.6 - 6.8)
C†	0.152	0.086	0.196	0.022	8.9	11.6
D	0.117	0.096	0.135	0.022	6.1	6.5
E	0.040	0.020	0.053	0.034	1.6	6.5

† Line C at angle $\varphi = 45^{\circ}$

6.4 Effective notch stress

A three dimensional finite element model has been created to find the most severely stressed point in the joint. To minimise the required computing resources

and computing time, the same sub-model strategy as for the 4-point bending case has been followed. The mesh densities of the global and the sub-models were similar to those given in Table 5.6. Linear elements (C3D8R) were used for the global model, whereas both sub-models were idealised using quadratic elements (C3D20R). Since the most highly stressed area is farther away from the axis of the chord than under 4-point bending, see Fig. 6.13b, the geometry of the second sub-model differs slightly to the 4-point bending analysis, cf. Figs. 5.11 and 6.13a.

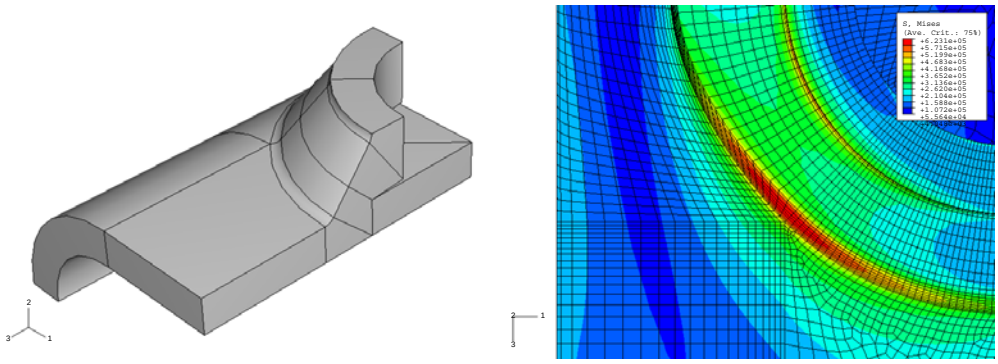

a) b)

Figure 6.13: (a) Geometry of the second sub-model, (b) von Mises equivalent stress near the weld.

The highest stressed point at the weld toe is situated where the the tangent to the weld toe forms an approximately 45° angle to the axis of the chord, see Fig. 6.14.

To get a detailed overview of the stress state at this point, all stress components have been extracted from the finite element analysis and Mohr's stress circle has been constructed. Both the stress values and Mohr's stress circle are given in Fig. 6.14. It is seen that the principal axes 1 and 2 are almost perpendicular and tangential to the weld toe, respectively. The third principal stress is practically zero as it should be, because of the free surface. Since $\sigma_2/\sigma_1 = 0.4$ and both stresses are positive, this stress state is found in quadrant I of Fig. 2.6 and the difference between Tresca and von Mises equivalent stress is close to the maximum value of 15 %.

As in Chapter 5, Peterson's, Neuber's and the gradient method to estimate the notch sensitivity are compared. The stress concentration factor is calculated to

$$K_\mathrm{t} = \frac{\sigma}{S} = \frac{0.232\ \mathrm{MPa/N}}{0.022\ \mathrm{MPa/N}} = 10.5\,. \tag{6.9}$$

The von Mises stress distribution in thickness direction at the highest stressed point is plotted in Fig. 6.15. The normalised stress gradient, χ, is found from this stress distribution to be

$$\chi = \left|\frac{1}{\sigma_\mathrm{max}}\frac{\mathrm{d}\sigma}{\mathrm{d}x}\right|_{x=0} = \frac{1}{10.5}\,\frac{10.5-9.3}{0.1\ \mathrm{mm}} = 1.14\ \mathrm{mm}^{-1}\,. \tag{6.10}$$

stress/nominal stress	
$\sigma_x/S_{\max}$	8.04
$\sigma_y/S_{\max}$	8.86
$\sigma_z/S_{\max}$	0.09
$\tau_{xy}/S_{\max}$	-3.64
$\tau_{xz}/S_{\max}$	-0.32
$\tau_{yz}/S_{\max}$	0.36
$\sigma_1/S_{\max}$	12.14
$\sigma_2/S_{\max}$	4.82
$\sigma_3/S_{\max}$	0.05
$\sigma_{\text{Mises}}/S_{\max}$	10.54

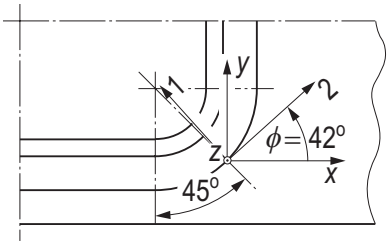

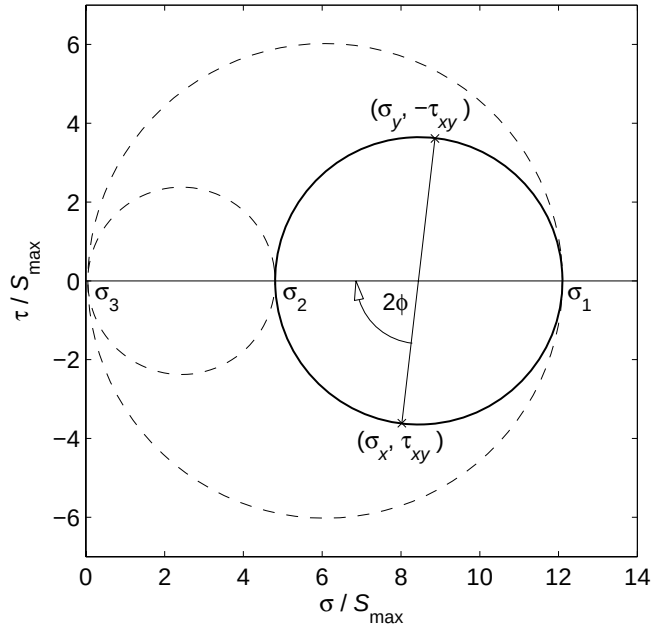

Figure 6.14: Stress components, principal stresses and von Mises equivalent stress at the point with maximal von Mises stress at the weld toe and Mohr's stress circle.

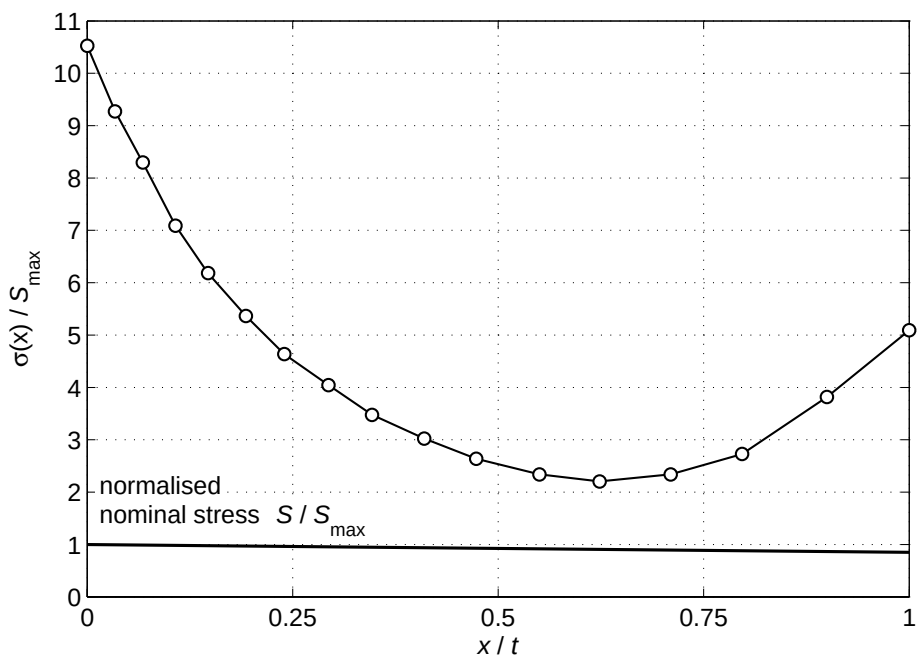

Figure 6.15: Von Mises stress distribution in thickness direction at the highest stressed point at the weld toe.

The required material constants for the three notch sensitivity approaches are listed in Table 6.5 together with the obtained fatigue notch factors. It is seen that reasonable agreement between the fatigue notch factors calculated with the different approaches is obtained.

Table 6.5: Fatigue notch factors calculated from $K_t = 10.5$ employing different approaches.

Approach	Eqs.	material parameter [mm]	geometric parameter	K_f
Peterson	2.9, 2.10	$\rho_0 = 0.64$ [42]	$\rho = 1$ mm	6.8
Neuber	2.9, 2.12	$\rho^* = 0.2$ [11]	$\rho = 1$ mm	6.8
Gradient	2.18, 2.20	$\rho^o = 0.075$ [11]	$\chi = 1.14$ mm^{-1}	8.1

Using Eq. 5.9 together with $K_f = 6.8$ to convert the effective notch stress S-N curve to nominal stress, with the Basquin parameters given in Table 5.7, the respectively marked S-N curve in Fig. 6.16 is obtained. It is seen that the predicted S-N curve is somewhat non-conservative.

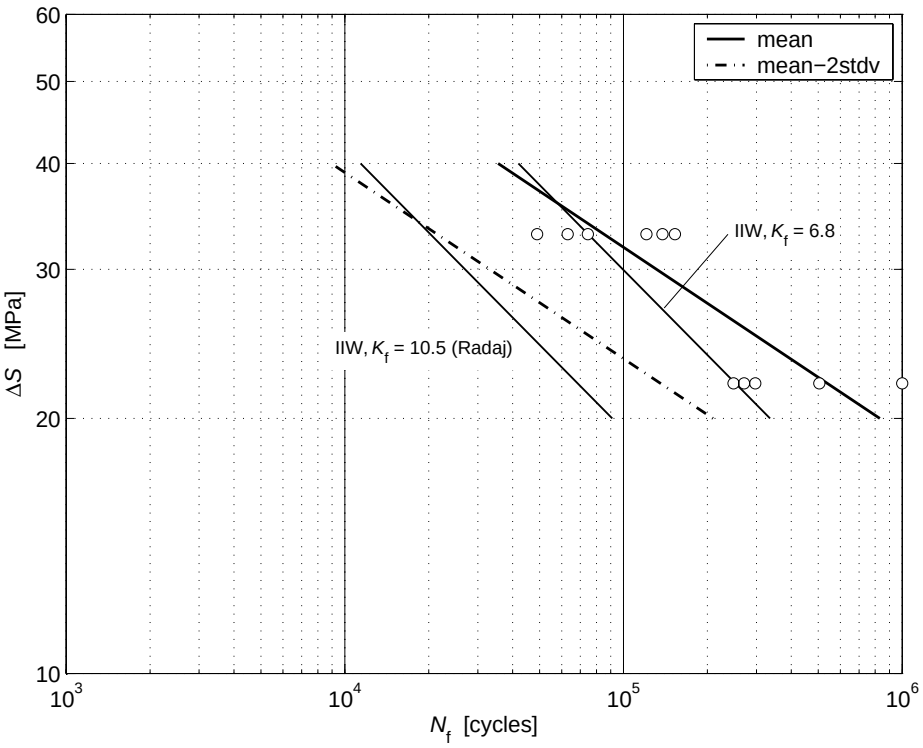

Figure 6.16: Experimental S-N curve compared to effective notch stress design curve from Eurocode 9 [5] expressed in terms of nominal stress.

6.4.1 The effective notch stress according to Radaj

Assuming $K_f = K_t(\rho_f = 1 \text{ mm}) = 10.5$ results in the second predicted S-N curve shown in Fig. 6.16. As for the 4-point bending load case, Radaj's effective

notch stress approach yields almost perfect agreement. The reason for Radaj's method being superior to the other effective notch stress approaches is certainly because the design S-N curve is proposed for the assumption of a 1 mm notch radius. Again, although not recommended for joints with wall thickness less than 5 mm [6, 28], the results indicate the applicability of the method down to 3 mm wall thickness.

6.5 Crack propagation analysis

Finally, after having applied the nominal, the structural hot spot and the effective notch stress approaches to the T-joint subjected to transverse bending, the fatigue life will be predicted using a crack growth analysis. Unfortunately, no M_{k} solution was found that is suitable to the current load case. Simply assuming the M_{k} factor given by Eq. B.4 is applicable to the transverse bending too would lead to the same S-N curves as in the 4-point bending load case, thus much too long lives would be predicted. Therefore, the method suggested by Carpinteri et al. [70] and described in Section 2.6.5 is applied here.

The stress gradient at the weld toe is available from the finite element analyses carried out to find the local stress. Figure 6.17 shows the through-thickness distribution of the maximum principal stress, as well as the approximation by the following 5th order polynomial

$$\frac{\sigma_1}{S_{\max}} = -18.66\xi^5 + 64.12\xi^4 - 84.64\xi^3 + 64.38\xi^2 - 37.40\xi + 12.16\,. \tag{6.11}$$

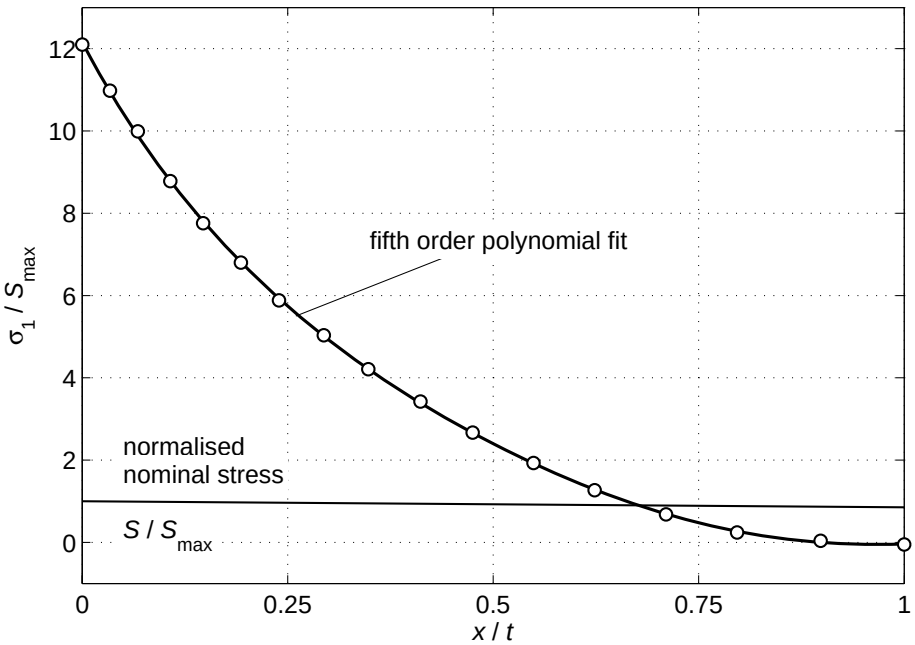

Figure 6.17: Through-thickness distribution of the maximum principal stress at the weld toe.

The geometry factor, F, is calculated from:

$$F = \sum_{n=0}^{5} F_n B_n \,, \tag{6.12}$$

where the coefficients B_n are found by applying Eq. 2.45:

$$\begin{aligned}
B_0 &= -18.66\alpha^5 + 64.12\alpha^4 - 84.64\alpha^3 + 64.38\alpha^2 - 37.40\alpha + 12.16 \\
B_1 &= 93.30\alpha^5 - 256.48\alpha^4 + 253.92\alpha^3 - 128.76\alpha^2 + 37.40\alpha \\
B_2 &= -186.60\alpha^5 + 384.72\alpha^4 - 253.92\alpha^3 + 64.38\alpha^2 \\
B_3 &= 186.60\alpha^5 - 256.48\alpha^4 + 84.64\alpha^3 \\
B_4 &= -93.30\alpha^5 + 64.12\alpha^4 \\
B_5 &= 18.66\alpha^5 \,.
\end{aligned}$$

Letting a semi-elliptical surface crack at the weld toe propagate from $a_\mathrm{i} = 0.05$ mm to $a_\mathrm{f} = 2.1$ mm ($\alpha = 0.017 \ldots 0.7$), the S-N curve in Fig. 6.18 is obtained. Similar to the 4-point bending analysis, the assumed final crack depth has been reduced to 2.1 mm to stay within the validity limit ($\alpha \leq 0.7$) of the method. As long as the crack was shorter then $\alpha = 0.1$ the F_n values for $\alpha = 0.1$ were used. The characteristic crack depth was set to $a^* = 0.11$ mm. The crack propagation data given at $R = 0.1$, see Table 5.3, were transformed to $R = 0.5$, which, according to Table 5.2, is realistic for untreated T-joints, using Walker's equation with $\gamma = 0.6$.

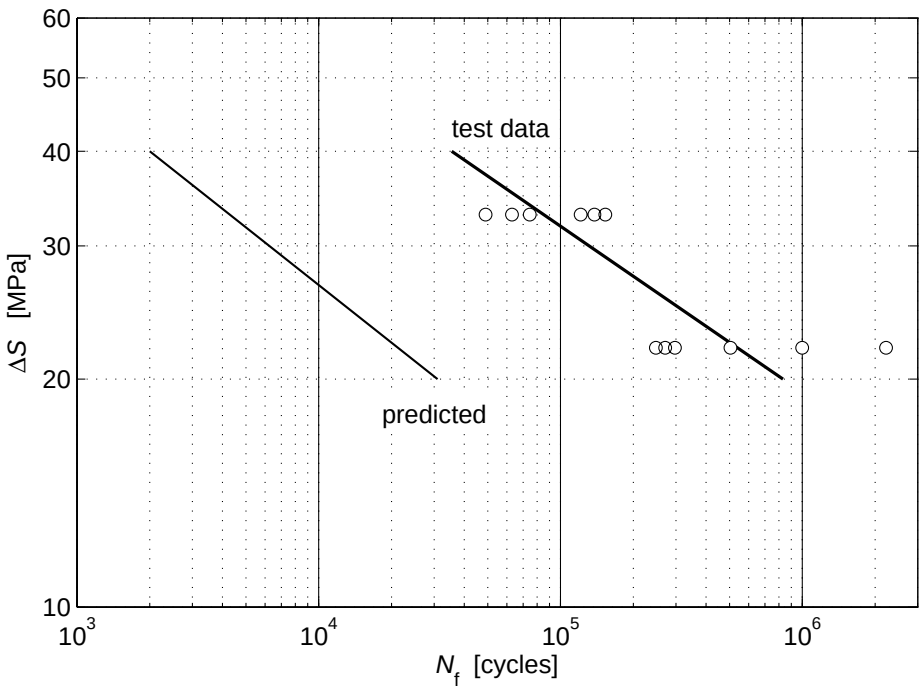

Figure 6.18: S-N curves for a semi-elliptical crack growing at the weld toe compared to experimental data.

Figure 6.18 shows the resultant prediction. It is seen that it is conservative by approximately a factor 40 in life. One explanation for this conservatism is

the fact that the highest stress is used throughout the propagation along the surface, even though the crack, as it propagates along the surface, grows along a decreasing stress field.

6.6 A comparison

As was done in the previous chapter, all the fatigue life predictions obtained are compared to each other. Figure 6.19 gives the S-N curves obtained with the different approaches and the experimental curves.

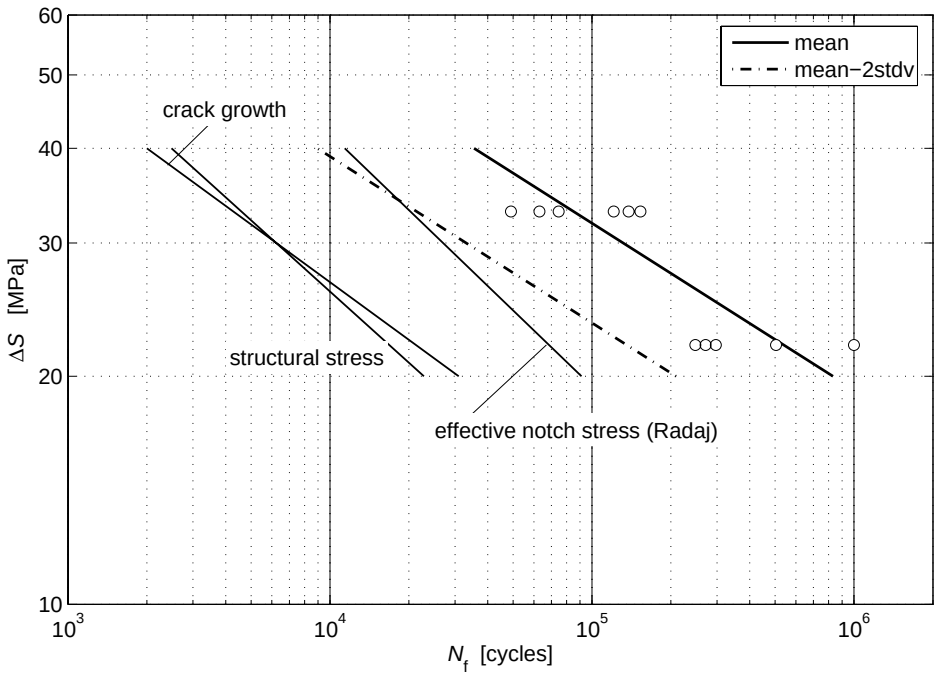

Figure 6.19: S-N curves obtained with the different approaches and the experimental curve.

It is seen that all predicted curves have a steeper slope than the experimental curves. The crack propagation approach and the structural hot spot stress approach yield very similar S-N curves. Both predictions are conservative. However, since the prediction from the crack propagation analysis must be compared to the mean curve and the structural hot spot stress prediction refers to the mean-2stdv curve, the curve from the crack propagation analysis is further from the experimental results.

In the standards referred to in this work, no suitable nominal stress detail category could be found, hence no prediction could be made using the nominal stress approach. The S-N curve from the effective notch stress approach according to Radaj is in excellent agreement with the mean-2stdv curve obtained from the fatigue tests. As for the 4-point bending load case, the S-N curve predicted using the notch sensitivity, cf. Fig. 6.16, gives slightly non-conservative results. An explanation for this conservatism is given in Section 5.6.

CHAPTER 7

Conclusions

7.1 Summary

If the effect of the mean stress is to be incorporated in a crack propagation analysis, Walker's equation with $\gamma = 0$ at $R \leq 0$ and $\gamma = 0.6$ at $R \geq 0$ is a good approximation for both the 7075-T6 and 2024-T3 aluminium alloys. An interesting alternative to Walker's mean stress equation is the equation proposed in Section 3.5. This equation represents an elegant means of incorporating the mean stress effect from $-1 \leq R < 1$ into one simple equation.

The crack propagation tests carried out on short cracks confirmed the crack propagation data based on long cracks found in the literature are applicable to shorter cracks too. The crack propagation rate was successfully measured using a special DC potential drop method. It was not obvious to apply this measurement technique to aluminium specimens with short cracks, because of the very good conductivity of aluminium. Two specimens showed some accelerated crack propagation at low stress intensity factor ranges, which is said to be typical for short cracks. Probably, the cracks in the other specimens were already too deep to show these effects. The scatter, especially at low ΔK, is partly due to differences in the crack growth behaviour as the crack propagates through the regions with the different grain structures. Based on the test results obtained at different stress ratios and literature data, a Walker exponent of $\gamma = 0.78$ for the 6082-T6 aluminium alloy was calculated. This value which is somewhat higher than $\gamma = 0.6$, which was found suitable for the 7075-T6 and 2024-T3 aluminium alloys, indicates a less pronounced mean stress dependency of crack growth in the 6082-T6 aluminium alloy.

The fatigue life of a welded aluminium T-joint has been estimated and compared with test results from both 4-point bending of the chord and transverse bending of the brace. For the 4-point bending load case all predictions are within a factor 10 in life. Similar deviations between the predictions from the differ-

ent models, on the one hand, and between the predictions and the experimental results, on the other hand were obtained for the transverse bending load case.

The nominal stress method may be assumed to be the most robust, however, due to the lack of an adequate detail category in current design codes and recommendations, no prediction for the transverse bending load case could be made. Instead, a new suitable detail category has been suggested. The prediction for the T-joint subjected to 4-point bending loading was conservative with a factor 2-5 in life.

The structural hot spot stress approach gave conservative results (factor 4-10 in life) for both load cases.

The effective notch stress approach according to Radaj resulted in excellent agreement with the mean-2stdv curves of the test data for both 4-point bending and transverse bending.

Finally, the crack propagation approach using the M_{k} factor gave excellent agreement in the case of the 4-point bending loading. For the transverse bending load case the available M_{k} equations were not suitable. Employing the local stress distribution gave conservative predictions for both load cases.

A reason for the different results obtained employing either M_{k} or the local stress distribution, is found in the actual stress used and the stress gradient along the weld toe. Shorter fatigue lives are predicted using the local stress distribution because the highest stress all along the surface is used throughout the crack propagation. However, a crack starting at the most highly stressed point will grow into a less stressed region, i.e., it will grow more slowly than assumed in the analysis. On the other hand, the equation used to calculate M_{k} does not account for the shear lag and the inhomogeneous stress distribution due to the hollow sections. Therefore, the method based on the local stress distribution and the one based on the M_{k} factor represent some sort of lower and upper bound fatigue life estimates, respectively. The fact that the initial defect size is usually unknown turms out to be rather unimportant, as long as the defects are about the same size as a^*.

7.2 Discussion and further work

When a suitable detail category is available, the nominal stress approach is a safe method. Incorporating the local effects in the detail category, i.e., in the S-N curve, the many uncertainties related to the local geometry are avoided, which in many cases are not possible to determine. The dependency on a nominal stress represents the main drawback of this method. On the other hand, its obvious attractiveness results from the simplicity and the minimum requirement on the stress analysis.

Including the global (structural) stress concentration in the stress analysis the structural hot spot stress approach eliminates the need of a nominal stress. However, the fact that the structural hot spot stress is a fictitious value that can be found only indirectly is not comforting, especially since there are a variety of approaches to calculate the structural hot spot stress. In addition, the result of these methods usually depend on the finite element mesh. A major drawback of

the structural hot spot stress approach is its restriction to failures starting from the weld toe.

The method that gave the best results, is the effective notch stress approach according to Radaj. This method circumvents the uncertainties related to the local weld geometry by assuming that the weld toe radius is 1 mm. Although recommended for wall thicknesses larger than 5 mm only [6, 28], the results indicate that the method is suitable for welded structures with a wall thickness as low as 3 mm. Both failure from the weld toe and the weld root can be treated. Only the very detailed stress analysis required is a drawback. However, precalculated notch stress concentration factors can be used together with a more global finite element analysis capturing only the global geometrical features of the structure (as implemented in the fatigue prediction software FEMFAT [109]). This drastically simplifies the practical use of the method.

According to the thesis stated in Chapter 1, the fatigue life of a welded component must be most accurately predicted using a crack propagation analysis, since the fatigue life is dominated by crack propagation. However, the crack propagation approaches investigated in this work are not reliable and flexible enough to be regarded as the best approach for welded structures.

Nevertheless, crack propagation remains a tempting approach, because of its physical basis, flexibility and since it is theoretically not limited to certain structures. The effect of mean stress can be accounted for in a straightforward manner, which has been successfully shown in Chapter 5. However, the crack propagation analysis is rather complex and more difficult to apply than the S-N curve based approaches. To accurately incorporate the effect of the local stress field appears to be the most important and widely unsolved problem. Under many practical circumstances, cracks will be subjected to stress gradients in both the depth and surface directions. Today, the M_{k} factor does not account for stress gradients in surface direction and the methods using the local stress distribution are only able to take care of the stress gradient in the surface direction to a certain extent. Therefore, developing equations to calculate M_{k} for more structural details, including those that have stress gradients in two directions, would be required. Using M_{k} has the strong benefit that no FE analysis is required. On the other hand, a nominal stress and an equation to calculate M_{k} for a given structural detail are needed, which returns to the drawbacks of the nominal stress approach. Therefore, despite the somewhat discouraging results, employing the local stress distribution is the more promising solution since no nominal stress is required, only a very detailed FE analysis. To improve the method it must be extended to treat stress gradients in both the depth and surface directions.

A third method is to use a computer program (finite or boundary element) that can model crack propagation, i.e., that directly calculates the stress intensity factor. Especially the boundary element method seems to be suitable, since the re-meshing effort upon crack extension is relatively low. The effort to apply the Franc3D program to the analysis of a crack at the weld toe of the T-joint was not successful. It is believed that this was due to the extremely small initial crack and the even smaller elements on the crack surfaces compared with the overall dimensions of the model, a limitation that certainly will be removed by more sophisticated software.

Treating short cracks by the approach suggested by El Haddad et al. [61], results in an increased crack propagation rate as long as the crack is short. Its simplicity makes it attractive for engineering applications. In addition, provided the model is correct, a very welcome feature is the relative insensitivity to the choice of the initial crack depth as long as the latter is smaller than a^*. It is of course tempting to learn more about the real mechanisms that affect the growth of a short crack. However, from a practical point of view taking care of the microstructural effects will complicate the analysis to a large degree, not the least because of the additionally required material parameters, which are practically impossible to acquire. At this level the statistical nature of the fatigue process is revealed. The probabilistic approaches to fatigue, however, have not been within the scope of this work.

Returning to the thesis stated in Chapter 1 it must be concluded that the fatigue life of a welded component can be predicted using a crack propagation analysis. However, the results are not generally superior to those from the other approaches and improvements in treating the local stress gradients are required.

Bibliography

[1] T. Mann, B. W. Tveiten, and G. Härkegård. Fatigue of welded aluminium T-joints. In *Proceedings of the 15th European Conference on Fracture*, KTH, Stockholm, 2004.

[2] T. Mann, B. W. Tveiten, and G. Härkegård. Fatigue crack growth analysis of welded aluminium RHS T-joints with manipulated residual stress level. *Fatigue & Fracture of Engineering Materials & Structures*, 29(2):113–122, 2006. ISSN 8756-758X.

[3] T. Mann. The influence of mean stress on fatigue crack propagation in aluminium alloys. *Submitted for publication in the International Journal of Fatigue*, 2005. ISSN 0142-1123.

[4] T. Mann, G. Härkegård, and K. Stärk. Short crack growth measurements in 6082-T6 aluminium alloy specimens. *Accepted for presentation at the International Conference on Fatigue Damage of Structural Materials VI, Hyannis*, 2006.

[5] CEN. *ENV 1999-2: Eurocode 9: Design of aluminium structures – Part 2: Structures susceptible to fatigue.* European Committee for Standardisation, 1998.

[6] IIW. *Recommendations for Fatigue Design of Welded Joints and Components.* A. Hobbacher, editor, International Institute of Welding document XIII-1965-03/XV-1127-03, 2004.

[7] T. A. Barnes and I. R. Pashby. Joining techniques for aluminium spaceframes used in automobiles part I – solid and liquid phase welding. *Journal of Materials Processing Technology*, 99(1–3):62–71, 2000. ISSN 0924-0136.

[8] T. A. Barnes and I. R. Pashby. Joining techniques for aluminium spaceframes used in automobiles part II – adhesive bonding and mechanical fasteners. *Journal of Materials Processing Technology*, 99(1–3):72–79, 2000. ISSN 0924-0136.

[9] E. Schubert, M. Klassen, I. Zerner, C. Walz, and G. Sepold. Light-weight structures produced by laser beam joining for future applications in automobile and aerospace industry. *Journal of Materials Processing Technology*, 115(1):2–8, 2001. ISSN 0924-0136.

[10] P. J. Haagensen and S. J. Maddox. *IIW Recommendations on Post Weld Improvement of Steel and Aluminium Structures.* International Institute of Welding document XIII-1815-00, 2004.

[11] D. Radaj. *Ermüdungsfestigkeit – Grundlagen für Leichtbau, Maschinen- und Stahlbau.* Springer-Verlag, Berlin, 1995. ISBN 3-540-58348-3.

[12] N. E. Dowling. *Mechanical Behaviour of Materials.* Prentice Hall, London, 2nd edition, 1999. ISBN 0-13-905720-X.

[13] S. Suresh. *Fatigue of Materials.* Cambridge University Press, Cambridge, 2nd edition, 2001. ISBN 0-521-57847-7.

[14] BSI. *BS 8118: Structural use of aluminium – Part 1: Code of practice for design.* British Standards Institution, 1991. ISBN 0-580-19209-1.

[15] ECCS. *European Recommendations for Aluminium Alloy Structures Fatigue Design.* European Convention for Constructional Steelwork, 1992.

[16] K. A. Macdonald and P. J. Haagensen. Fatigue design of welded aluminum rectangular hollow section joints. *Engineering Failure Analysis*, 6(2):113–130, 1999. ISSN 1350-6307.

[17] E. Niemi, editor. *Stress Determination for Fatigue Analysis of Welded Components.* Abington Publishing, Cambridge, 1995. ISBN 1-85573-213-0.

[18] D. Radaj. *Design and Analysis of Fatigue Resistant Welded Structures.* Abington Publishing, Cambridge, 1990. ISBN 1-85573-004-9.

[19] A. Berkovits, D. W. Kelly, and S. Di. Considerations of the effect of residual stresses on fatigue of welded aluminium alloy structures. *Fatigue & Fracture of Engineering Materials & Structures*, 21(2):159–170, 1998. ISSN 8756-758X.

[20] O. R. Myhr, S. Klokkehaug, H. G. Fjær, Ø. Grong, and A. O. Kluken. Modelling of microstructure evolution, residual stresses and distortions in 6082-T6 aluminium weldments. *Welding Journal*, 77(7):286–292, 1998.

[21] O. R. Myhr, Ø. Grong, S. Klokkehaug, H. G. Fjær, and A. O. Kluken. Modelling of the microstructure and strength evolution during ageing and welding of Al-Mg-Si alloys. In *6th International Seminar on Nummerical Analysis of Weldability*, Graz-Seggau, Austria, 1-3 October 2001.

[22] H. G. Fjær, O. R. Myhr, S. Klokkehaug, and S. Holm. Advances in aluminium weld simulations applying weldsim. In *11th International Conference om Computer Technology in Welding*, Columbus, Ohio, December 2001.

[23] S. J. Maddox. *Fatigue Strength of Welded Structures.* Abington Publishing, Cambridge, 1991. ISBN 1-85573-013-8.

[24] J. M. Pinho da Cruz, J. M. Ferreira, J. M. Costa, and L. P. Borrego. Fatigue analysis of thin AlMgSi welded joints under constant and variable amplitude block loadings. *Thin-Walled Structures*, 41(5):389–402, 2003. ISSN 0263-8231.

[25] NTS. *NORSOK N-004: Design of steel structures.* Norwegian Technology Standards Institution, Oslo, 1998.

[26] O. Doerk, W. Fricke, and C. Weissenborn. Comparison of different calculation methods for structural stresses at welded joints. *International Journal of Fatigue*, 25(5):359–369, 2003. ISSN 0142-1123.

[27] E. Niemi. *Structural Hot-Spot Stress Approach to Fatigue Analysis of Welded Components – Designer's Guide*. International Institute of Welding document XIII-1819-00/XV-1090-01, 2003.

[28] DNV. *Fatigue Design of Offshore Steel Structures*. Det Norske Veritas Recommended Practice DNV-RP-C203, Høvik, Norway, 2005. ISBN 1-85573-533-9.

[29] E. Niemi and P. Tanskanen. *Hot Spot Stress determination for welded edge gussets*. International Institute of Welding document XIII-1781-99/XV-1027-99, 1999.

[30] B. W. Tveiten. *Fatigue Assessment of Welded Aluminum Ship Details*. PhD thesis, Norwegian University of Science and Technology, Trondheim, 1999. ISBN 82-471-0417-2.

[31] B. W. Tveiten and T. Moan. Determination of structural stress for fatigue assessment of welded aluminum ship details. *Marine Structures*, 13(3):189–212, 2000. ISSN 0951-8339.

[32] B. W. Tveiten. *The Fatigue Strength of RHS T-joints*. SINTEF report STF24 A03220, Trondheim, 2003. ISBN 82-14-02655-5.

[33] P. Dong. A structural stress definition and numerical implementation for fatigue analysis of welded joints. *International Journal of Fatigue*, 23(10):865–876, 2001. ISSN 0142-1123.

[34] I. Poutiainen, P. Tanskanen, and G. Marquis. Finite element methods for structural hot spot stress determination - a comparison of procedures. *International Journal of Fatigue*, 26(11):1147–1157, 2004. ISSN 0142-1123.

[35] Z.-G. Xiao and K. Yamada. A method of determining geometric stress for fatigue strength evaluation of steel welded joints. *International Journal of Fatigue*, 26(12):1277–1293, 2004. ISSN 0142-1123.

[36] H. Kyuba and P. Dong. Equilibrium-equivalent structural stress approach to fatigue analysis of a rectangular hollow section joint. *International Journal of Fatigue*, 27(1):85–94, 2005. ISSN 0142-1123.

[37] P. Dong. A structural stress definition and numerical implementation for fatigue analysis of welded joints. *Journal of Offshore Mechanics and Arctic Engineering*, 127(1):68–74, 2005. ISSN 0892-7219.

[38] B. E. Healy. Hot spot stress analysis of a side shell connection using surface extrapolation and the battelle structural stress method. In M. M. Salama, P. K. Gorf, C. F. Mastrangelo, and S. Balint, editors, *Proceeding of OMAE Specialty Symposium on Integrity of Floating Production, Storage & Offloading (FPSO) Systems*, Houston, 2004. ASME.

[39] I. Poutiainen and G. Marquis. *A single-point structural stress assessment procedure for load-carrying fillet welds*. International Institute of Welding document XIII-2012-04/XV1174-04, 2004.

[40] I. Poutiainen and G. Marquis. *A modified hot spot stress method based on weld stresses.* International Institute of Welding document XIII-2087-05/XV-1205-05, 2005.

[41] W. D. Pilkey. *Peterson's stress concentration factors.* John Wiley & Sons, New York, 2nd edition, 1997.

[42] R. E. Peterson. Notch-sensitivity. In G. Sines and J. L. Waisman, editors, *Metal Fatigue*, pages 293–306. McGraw-Hill, New York, 1959.

[43] A. Thum and W. Buchmann. *Dauerfestigkeit und Konstruktion*, volume 1 of *Mitteilungen der Materialprüfungsanstalt an der Technischen Hochschule Darmstadt.* VDI-Verlag, Berlin, 1932.

[44] W. Beitz and K.-H. Grothe, editors. *Dubbel - Taschenbuch für den Maschinenbau.* Springer-Verlag, Berlin, 20th edition, 2001. ISBN 3-540-67777-1.

[45] H. Neuber. *Kerbspannungslehre. Grundlagen für genaue Spannungsrechnung.* Springer, Berlin, 1937.

[46] H. Neuber. Über die Berücksichtigung der Spannungskonzentration bei Festigkeitsberechnungen. *Konstruktion*, 20(7):345–351, 1968. ISSN 0720-595.

[47] E. Siebel and M. Pfender. Weiterentwicklung der Festigkeitsberechnung bei wechselnder Beanspruchung. *Stahl und Eisen*, 67:318–, 1947. ISSN 0340-4803.

[48] E. Siebel and H. Meuth. Die Wirkung von Kerben bei schwingender Beanspruchung. *VDI–Zeitschrift*, 91(13):319–323, 1949. ISSN 0042-1766.

[49] E. Siebel and M. Stieler. Ungleichförmige Spannungsverteilung bei schwingender Beanspruchung. *VDI–Zeitschrift*, 97(5):121–126, 1955. ISSN 0042-1766.

[50] DIN. *DIN743-2: Tragfähigkeitsberechnung von Wellen und Achsen – Teil 2: Formzahlen und Kerbwirkungszahlen.* Deutsches Institut für Normung e.V., Berlin, 2000.

[51] C. Petersen. Die Vorgänge im zügig und wechselnd beanspruchten Metallgefüge. *Zeitschrift für Metallkunde*, 42:319–323, 1951, 43:429–433, 1952. ISSN 0044-3093.

[52] C. M. Sonsino, D. Radaj, U. Brandt, and H. P. Lehrke. Fatigue assessment of welded joints in AlMg 4.5Mn aluminium alloy (AA5083) by local approaches. *International Journal of Fatigue*, 21(9):985–999, 1999. ISSN 0142-1123.

[53] K. J. Miller and E. R. de los Rios, editors. *The Behaviour of Short Fatigue Cracks.* Mechanical Engineering Publications, London, 1986. ISBN 0-85298-615-7.

[54] P. C. Paris and F. Erdogan. A critical analysis of crack propagation laws. *Journal of Basic Engineering*, 85:528–534, December 1963. ISSN 0021-9223.

[55] O. D. Dijkstra, F. Soetens, and I. J. J. van Straalen. *Inventory of fatigue crack growth models and their data for aluminium alloy structures.* TNO-report B-89-677, TNO Building and Construction Research, Delft, 1990.

[56] M. S. Miller and J. P. Gallagher. An analysis of several fatigue crack growth rate (FCGR) descriptions. In S. J. Hudak and R. J. Bucci, editors, *Fatigue crack growth measurements and data analysis*, pages 205–251. ASTM STP 738, Philadelphia, 1981.

[57] F. Bergner and G. Zouhar. New approach to the correlation between the coefficient and the exponent in the power law equation of fatigue crack growth. *International Journal of Fatigue*, 22(3):229–239, March 2000. ISSN 0142-1123.

[58] M. Klesnil and P. Lukáš. Influence of strength and stress history on growth and stabilisation of fatigue cracks. *Engineering Fracture Mechanics*, 4:77–92, 1972. ISSN 0013-7944.

[59] R. G. Forman, V. E. Kearney, and R. M. Engle. Numerical analysis of crack propagation in cyclic-loaded structures. *Journal of Basic Engineering*, 89:459–464, September 1967. ISSN 0021-9223.

[60] F. Erdogan and M. Ratwani. Fatigue and fracture of cylindrical shells containing a circumferential crack. *International Journal of Fracture Mechanics*, 6(4):379–392, December 1970. ISSN 0020-7268.

[61] M. H. El Haddad, K. N. Smith, and T. H. Topper. Fatigue crack propagation of short cracks. *Journal of Engineering Materials Technology*, 101:42–46, 1979. ISSN 0094-4289.

[62] G. Härkegård. An effective stress intensity factor and the determination of the notched fatigue limit. In *Proceedings of the International Symposium of Fatigue Thresholds*, pages 867–879, Stockholm, 1981.

[63] H. Kitagawa and S. Takahashi. Applicability of fracture mechanics to very small cracks or the cracks in the early stage. In *2nd International Conference on Mechanical Behaviour of Materials*, pages 627–630, Boston, Ma, 1976.

[64] G. Härkegård, J. Denk, and K. Stärk. Growth of naturally initiated fatigue cracks in ferritic gas turbine rotor steels. *International Journal of Fatigue*, 27(6):715–726, 2005. ISSN 0142-1123.

[65] D. Bowness and M. M. K. Lee. Weld toe magnification factors for semi-elliptical cracks in T-butt joints – comparison with existing solutions. *International Journal of Fatigue*, 22(5):389–396, 2000. ISSN 0142-1123.

[66] BSI. *BS 7910: Guide on methods for assessing the acceptability of flaws in metallic structures.* British Standards Institution, 1999. ISBN 0-580-33081-8.

[67] D. Bowness and M. M. K. Lee. Prediction of weld toe magnification factors for semi-elliptical cracks in T-butt joints. *International Journal of Fatigue*, 22(5):369–387, 2000. ISSN 0142-1123.

[68] J. C. Newman Jr. and I. S. Raju. Empirical stress-intensity factor equation for the surface crack. *Engineering Fracture Mechanics*, 15(1–2):185–192, 1981. ISSN 0013-7944.

[69] S. Pommier, C. Sakae, and Y. Murakami. An empirical stress intensity factor set of equations for a semi-elliptical crack in a semi-infinite body subjected to a polynomial stress distribution. *International Journal of Fatigue*, 21(3):243–251, 1999. ISSN 0142-1123.

[70] A. Carpinteri, R. Brighenti, H.-J. Huth, and S. Vantadori. Fatigue growth of a surface crack in a welded T-joint. *International Journal of Fatigue*, 27(1):59–69, 2004. ISSN 0142-1123.

[71] H.-J. Huth. *Fatigue Design of Hydraulic Turbine Runners*. PhD thesis, Norwegian University of Science and Technology, Trondheim, 2005. ISBN 82-471-6900-2.

[72] H. Å. Jergéus. A simple formula for the stress intensity factors of cracks in side notches. *International Journal of Fracture*, 14:R113–R116, 1975. ISSN 0376-9429.

[73] A. Wormsen, A. Fjeldstad, and G. Härkegård. The application of asymptotic solutions to a semi-elliptical crack at the root of a notch. *Engineering Fracture Mechanics*, 2006. ISSN 0013-7944.

[74] D. Kujawski. A new $(\Delta K^{+} K_{\max})^{0.5}$ driving force parameter for crack growth in aluminium alloys. *International Journal of Fatigue*, 23:733–740, 2001. ISSN 0142-1123.

[75] D. Kujawski and S. Stoychev. Parametric study on the variability of opening load determination. *International Journal of Fatigue*, 25:1181–1187, 2003. ISSN 0142-1123.

[76] D. Kujawski. On assumptions associated with ΔK_{eff} and their implications on FCG predictions. *International Journal of Fatigue*, 27:1267–1276, 2005. ISSN 0142-1123.

[77] B. W. Tveiten, A. Fjeldstad, G. Härkegård, O. R. Myhr, and B. Bjørneklett. Fatigue life enhancement of aluminium joints through mechanical and thermal prestressing. *International Journal of Fatigue*, 2006. ISSN 0142-1123, In Press.

[78] O. R. Myhr, B. W. Tveiten, H. G. Fjær, and B. Bjørneklett. Through process modelling in manufacturing of aluminium structures for automotive applications. In *TMS Global Innovations Symposium*. USA, 2005.

[79] J. A. Graham, editor. *Fatigue Design Handbook*, volume 4. Society of Automotive Engineers, Warrendale, 1968. ISBN 0-89883-004-4.

[80] K. N. Smith, P. Watson, and T. H. Topper. Stress-strain function for the fatigue of metals. *Journal of Materials*, 5(4):767–78, December 1970. ISSN 0022-2453.

[81] K. Walker. The effect of stress ratio during crack propagation and fatigue for 2024-T3 and 7075-T6 aluminum. In *Effects of Environment and Complex Load History on Fatigue Life*, pages 1–14. ASTM STP 462, Philadelphia, 1970. ISBN 8031-0050-7.

[82] W. Elber. The significance of fatigue crack closure. In *Damage Tolerance in Aircraft Structures*, pages 230–242. ASTM STP 486, Philadelphia, 1971. ISBN 0-8031-0072-8.

[83] J. Schijve. Some formulas for the crack opening stress level. *Engineering Fracture Mechanics*, 14(3):461–465, 1981. ISSN 0013-7944.

[84] D. Broek and J. Schijve. The influence of the mean stress on the propagation of fatigue cracks in aluminium alloy sheet. *NLR-TR M2111*, 1963.

[85] R. Bu and R. I. Stephens. Comparison of short and long fatigue crack growth in 7075-T6 aluminum. *Fatigue & Fracture of Engineering Materials & Structures*, 9(1):35–48, 1986. ISSN 8756-758X.

[86] K. Donald and P. C. Paris. An evaluation of ΔK_{eff} estimation procedures on 6061-T6 and 2024-T3 aluminum alloys. *International Journal of Fatigue*, 21(supplement 1):S47–S57, 1999. ISSN 0142-1123.

[87] MCIC. *Damage Tolerant Design Handbook.* Metals and Ceramics Information Center, Battelle, 1972.

[88] J. A. R. Durán, J. T. P. Castro, and J. C. P. Filho. Fatigue crack propagation prediction by cyclic plasticity damage accumulation models. *Fatigue & Fracture of Engineering Materials & Structures*, 26(2):137–150, February 2003. ISSN 8756-758X.

[89] W. G. Fleck and R. B. Anderson. A mechanical model of fatigue crack propagation. In P. L. Pratt, editor, *Proceedings of the second International Conference on Fracture, Brighton*, London, 1969. Chapman & Hall. ISBN 0-412-09470-3.

[90] C. M. Hudson. Effect of stress ratio on fatigue-crack growth in 7075-T6 and 2024-T3 aluminum-alloy specimens. *NASA TN D-5390*, 1969.

[91] X. R. Wu, J. C. Newman, W. Zhao, M. H. Swain, C. F. Ding, and E. P. Phillips. Small crack growth and fatigue life predictions for high-strength aluminium alloys: Part I – experimental and fracture mechanics analysis. *Fatigue & Fracture of Engineering Materials & Structures*, 21(11):1289–1306, 1998. ISSN 8756-758X.

[92] C. van Kranenburg, W. He, J. Zuidema, and F. Veer. Influence of measurement method on fatigue crack growth threshold. In *Proceedings of the 15th European Conference on Fracture*, KTH, Stockholm, 2004.

[93] K. Stärk. Entwicklung einer rechnergesteuerten Potentialsonde für Rißwachstumsmessungen. *VDI Berichte*, 631:331–342, 1987.

[94] K. Stärk, J. Denk, and G. Kiesling. Messgitter zur optischen Risslängenbestimmung. *Material und Technik*, 2:43–47, 1983.

[95] G. Dobmann, K.-D. Becker, and P. Höller. Numerische und experimentelle Untersuchungen zum Gleichstrom-Potentialsondenverfahren im Fall der Teildurchströmung. *Materialprüfung*, 18(9):342–344, 1976. ISSN 0025-5300.

[96] H. H. Johnson. Calibrating the electric potential method for studying slow crack growth. *Materials Research & Standards*, 5:442–445, 1965.

[97] T. L. Anderson. *Fracture Mechanics – Fundamentals and Applications.* CRC Press, Boca Raton, 2nd edition, 1995. ISBN 0-8493-4260-0.

[98] L. P. Borrego, J. M. Ferreira, and J. M. Costa. Fatigue crack growth and crack closure in an AlMgSi alloy. *Fatigue & Fracture of Engineering Materials & Structures*, 24(4):255–265, 2001. ISSN 1460-2695.

[99] J. Samuelsson. Cold laps and weld quality acceptance limits. In J. Samuelsson, editor, *Design and analysis of welded high strength steel structures*, pages 151–161. EMAS LTD, Stockholm, Sweden, 2002.

[100] J. Martinsson. Fatigue strength of welded cruciform joint with cold laps. In J. Samuelsson, editor, *Design and analysis of welded high strength steel structures*, pages 163–184. EMAS LTD, Stockholm, Sweden, 2002.

[101] IIW. *Fatigue Design Procedure for Welded Hollow Section Joints.* X.-L. Zhao and J. A. Packer, editors, International Institute of Welding document XIII-1804-99/XV-1035-99, Abington Publishing, Cambridge, 2000. ISBN 1-85573-533-9.

[102] T. Haavi. Fatigue of welded joints in extruded aluminium hollow section profiles (in Norwegian). Master's thesis, Norwegian University of Science and Technology, Trondheim, Norway, 1999.

[103] A. Beste, P. Heuler, and O. Birk. Betriebsfestigkeit von Werkstoffproben und Fahrzeugbauteilen aus Aluminium. In T. Seeger and S. Klee, editors, *25 Jahre Fachgebiet Werkstoffmechanik an der TU Darmstadt, Vorträge des Festkolloquiums am 28.09.2001*, pages 148–168. TU Darmstadt, Institut für Stahlbau und Werkstoffmechanik, 2001. Heft 65.

[104] Cornell Fracture Group. *FRANC3D Menu & Dialog Reference, Version 2.6.* Cornell University, Ithaca, NY, 2003. http://www.cfg.cornell.edu.

[105] Cornell Fracture Group. *FRANC3D Concepts & Users Guide, Version 2.6.* Cornell University, Ithaca, NY, 2003. http://www.cfg.cornell.edu.

[106] C. M. Hudson and S. K. Seward. A compendium of sources of fracture toughness and fatigue-crack growth data for metallic alloys – Part I-III. *International Journal of Fracture*, 14(4):R151–R184, 1978, 20(3):R59–R117, 1982, 39(4):R43–R63, 1989. ISSN 0376-9429.

[107] C. M. Hudson and J. J. Ferrainolo. A compendium of sources of fracture toughness and fatigue-crack growth data for metallic alloys – Part IV. *International Journal of Fracture*, 48(2):R19–R43, 1991. ISSN 0376-9429.

[108] A. M. van Wingerde. *The Fatigue Behaviour of T- and X-Joints Made of Square Hollow Sections.* PhD thesis, TU Delft, 1992.

[109] Magna Powertrain, Engineering Center Steyr GmbH & Co KG, http://www.fem fat.com.

[110] H. Tada, P. C. Paris, and G. R. Irwin. *The stress analysis of cracks handbook.* Professional Engineering Publishing, New York, 3rd edition, 2000. ISBN 1-86058-304-0.

[111] L. P. Pook. Some implications of corner point singularities. *Engineering Fracture Mechanics*, 48(3):367–378, 1994. ISSN 0013-7944.

APPENDIX A

Walker's equation

A.1 Fatigue limit

If the fatigue limit is know at R_1 and the structure to be analysed is loaded at R, both can be related using Walker's equation. Equation 3.8 gives for R_1

$$\Delta\sigma_{\mathrm{A}}(R_1) = \Delta\sigma_{\mathrm{A,Walker}}\,(1 - R_1)^{1-\gamma_{\mathrm{A}}} \tag{A.1}$$

Combining Eqs. 3.8 and A.1 an equation follows that relates the fatigue limit at two arbitrary mean stress levels

$$\Delta\sigma_{\mathrm{A}}(R) = \Delta\sigma_{\mathrm{A}}(R_1)\left(\frac{1-R}{1-R_1}\right)^{1-\gamma_{\mathrm{A}}} . \tag{A.2}$$

If the fatigue limit is known at at least two different mean stresses, γ_{A} can be calculated. The dependency of the threshold stress intensity range, ΔK_{th}, on mean stress may also be described using Walker's equation, using the exponent γ_{th}. Both exponents, γ_{A} and γ_{th} do not necessarily have the same value, since they describe the dependence on R of the fatigue limit of a polished specimen and of a cracked specimen, respectively. γ_{th} may be roughly estimated from

$$\gamma_{\mathrm{th}} = 1 - \frac{1}{m}\,, \tag{A.3}$$

given in [18], where m is the exponent in Paris' law. Expressing the dependency of the stress intensity factor range, ΔK, on mean stress with Walker's equation, the exponent may be called γ. Dowling [12] states that in general $\gamma > \gamma_{\mathrm{th}}$. The dependency on R is more pronounced at low ΔK.

A.2 Crack propagation rate

If the crack propagation data (C_1 and m) have been obtained at R_1, but the structure is loaded at R, the constant C must be modified to match the actual

loading. The Paris exponent m is approximately independent of R. Rewriting Eq. A.2 in terms of stress intensity range and inserting in Paris' law leads to

$$\frac{\mathrm{d}a}{\mathrm{d}N} = C_1 \left[\left(\frac{1-R_1}{1-R} \right)^{1-\gamma} \Delta K(R) \right]^m . \tag{A.4}$$

Rearranging gives

$$\frac{\mathrm{d}a}{\mathrm{d}N} = C \Delta K^m , \tag{A.5}$$

with

$$C = \begin{cases} C_1 \left(\frac{1-R_1}{1-R}\right)^{(1-\gamma)m} & \text{if} \quad R_1 > 0 \text{ and } R > 0 \\ C_1 \left(\frac{(1-R_1)^{1-\gamma}}{1-R}\right)^m & \text{if} \quad R_1 > 0 \text{ and } R < 0 \\ C_1 \left(\frac{1-R_1}{(1-R)^{1-\gamma}}\right)^m & \text{if} \quad R_1 < 0 \text{ and } R > 0 \\ C_1 \left(\frac{1-R_1}{1-R}\right)^m & \text{if} \quad R_1 < 0 \text{ and } R < 0 \end{cases} . \tag{A.6}$$

A.3 Linear regression to find Walker exponent

Taking the logarithm of Eq. 3.13 gives the following linear relationship:

$$y(x) = a + bx , \tag{A.7}$$

with $y = \log \Delta K(R)$, $x = \log(1-R)$, $a = \log \Delta K_{\text{Walker}}$ and $b = (1-\gamma)$. If data at $R \geq 0$ or $R \leq 0$ are only given, the standard least mean squares method can be used to find a γ valid for $R \geq 0$ or $R \leq 0$, respectively. However, having data at both, positive and negative R ratios, the standard least mean squares method is not appropriate.

Since the dependency of ΔK on R changes when R becomes negative, the Walker exponent must change also. Therefore the least mean squares method must be modified to obtain a continuous curve. To be more precise, two interpolation curves, one for $R \geq 0$ and one for $R \leq 0$, must be found that intersect at $R = 0$. This may be achieved by fulfilling the following condition,

$$\sum_i^n \left[y_i - y_1(x_i) \right]^2 + \sum_j^m \left[y_j - y_2(x_j) \right]^2 \stackrel{!}{=} \min , \tag{A.8}$$

with $y_1(x) = a + bx$ and $y_2(x) = a + cx$. If the index i applies to data points for $R \leq 0$, then j applies at $R \geq 0$. Partial differentiation with respect to a, b and c gives a system of linear equations to calculate a, b and c and hence ΔK_{Walker}, $\gamma(R \leq 0)$ and $\gamma(R \geq 0)$.

$$\begin{bmatrix} n+m & \sum_i^n x_i & \sum_j^m x_j \\ \sum_i^n x_i & \sum_i^n x_i^2 & 0 \\ \sum_j^m x_j & 0 & \sum_j^m x_j^2 \end{bmatrix} \begin{bmatrix} a \\ b \\ c \end{bmatrix} = \begin{bmatrix} \sum_i^n y_i + \sum_j^m y_j \\ \sum_i^n x_i y_i \\ \sum_j^m x_j y_j \end{bmatrix} . \tag{A.9}$$

APPENDIX B

Geometry functions for some crack configurations

B.1 Edge crack in a finite plate

Empirical geometry functions for an edge crack in a finite plate (width w) subjected to a membrane load can be found in [110], for example

$$F = 0.265\left(1-\frac{a}{w}\right)^4 + \frac{0.857+0.265\dfrac{a}{w}}{\left(1-\dfrac{a}{w}\right)^{1.5}} \tag{B.1}$$

B.2 Semi-elliptical surface crack in a finite plate

Newman and Raju [68] proposed a geometry function for a semi-elliptical surface crack, see Fig. B.1, in a finite plate subjected to membrane and bending load. For a membrane load the following equation applies:

$$F = \frac{1}{\sqrt{Q}}\left[M_1 + M_2\left(\frac{a}{t}\right)^2 + M_3\left(\frac{a}{t}\right)^4\right] f_\phi f_w g\,, \tag{B.2}$$

for $0 < a/c \leq 1$, $0 \leq a/t \leq 1$, $c/w < 0.5$ and $0 \leq \phi \leq \pi$, with

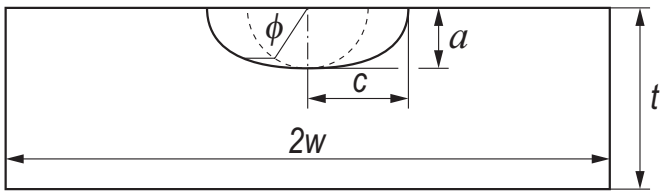

Figure B.1: Semi-elliptical surface crack in a plate with finite width and finite thickness.

$$\sqrt{Q} = \int_0^{\pi/2} \sqrt{1 - \left[1 - \left(\frac{a}{c}\right)^2\right]^2 \sin^2\beta \, \mathrm{d}\beta} \approx \sqrt{1 + 1.464 \left(\frac{a}{c}\right)^{1.65}} \qquad \left(\frac{a}{c} \leq 1\right) ,$$

$$M_1 = 1.13 - 0.09 \left(\frac{a}{c}\right) , \qquad M_2 = -0.54 + \frac{0.89}{0.2 + \frac{a}{c}} ,$$

$$M_3 = 0.5 - \frac{1}{0.65 + \frac{a}{c}} + 14 \left(1 - \frac{a}{c}\right)^{24} , \quad f_\phi = \left[\left(\frac{a}{c}\right)^2 \cos^2\phi + \sin^2\phi\right]^{0.25} ,$$

$$f_w = \left[1/\cos\left(\frac{\pi c}{2w}\sqrt{\frac{a}{t}}\right)\right]^{0.5} , \qquad g = 1 + \left[0.1 + 0.35\left(\frac{a}{t}\right)^2\right](1 - \sin\phi)^2 .$$

For a shallow crack ($a/t \ll 1$), Eq. B.2 simplifies to

$$F = \frac{1}{\sqrt{Q}} M_1 f_\phi g . \tag{B.3}$$

B.3 Semi-elliptical surface crack at a weld toe in a finite plate

If a weld toe is the starting point of a crack, it will not grow through a constant stress field, but through a decreasing one. The stress gradient is caused by a stress concentration introduced by the weld toe radius (notch) and the attachment. Bowness and Lee [65,67] proposed and verified a set of equations to calculate the correction factor, M_k, to the stress intensity factor solution for a semi-elliptical edge crack in a plate, see Appendix B.2. This factor includes the effect of the attachment and the weld toe radius. The proposed equations are based on finite element analyses of a T-joint made from plates (see Fig. B.2). British Standard BS 7910 [66] refers to the work from Bowness and Lee.

Deepest point

The M_k factor at the deepest point of the crack for "as welded" conditions (weld toe radius $\rho \leq 0.1\times$ plate thickness t) and membrane load is given as

$$M_\mathrm{k} = f_1(\alpha, \beta) + f_2(\alpha, \theta) + f_3(\alpha, \theta, \gamma) , \tag{B.4}$$

with $\alpha = a/t$, $\beta = a/c$, $\gamma = l/t$. The factors f_1, f_2 and f_3 are defined as follows:

$$f_1 = 0.43358\alpha^{\left(A_1+(A_2\alpha)^{A_3}\right)} + 0.93163\,\mathrm{e}^{\alpha^{-0.050966}} + A_4\,,$$

$$f_2 = A_5\,(1-\alpha)^{A_6} + A_7\alpha^{-0.1074\alpha}\,,$$

$$f_3 = A_8\alpha^{\left(A_9\theta^2+A_{10}\theta+A_{11}\right)} + A_{12}\alpha^{A_{13}} + A_{14}\alpha^2 + A_{15}\alpha + A_{16}\,,$$

$$\begin{aligned}
A_1 &= -1.0343\beta^2 - 0.15657\beta + 1.3409\,,\\
A_2 &= 1.3218\beta^{(-0.61153)}\,,\\
A_3 &= -0.87238\beta + 1.2788\,,\\
A_4 &= -0.46190\beta^3 + 0.6709\beta^2 - 0.37571\beta + 4.6511\,,\\
A_5 &= -0.00038737\theta^2 + 0.64771\theta - 0.72368\,,\\
A_6 &= 0.24183\theta + 176.23\,,\\
A_7 &= -0.00027743\theta + 2.8143\,,\\
A_8 &= -0.082502\theta^2 + 0.0084862\theta + 0.38417\,,\\
A_9 &= 0.010766\gamma^3 - 0.060159\gamma^2 + 0.13667\gamma - 0.0234\,,\\
A_{10} &= -0.028378\gamma^3 + 0.16489\gamma^2 - 0.35584\gamma - 0.00024554\,,\\
A_{11} &= -0.0015061\gamma^2 + 0.023369\gamma - 0.23124\,,\\
A_{12} &= 0.051554\theta^2 + 0.025447\theta + 1.8975\,,\\
A_{13} &= -0.12914\theta^2 + 0.21863\theta + 0.13798\,,\\
A_{14} &= -0.20136\gamma^2 + 0.93311\gamma - 0.41496\,,\\
A_{15} &= 0.20188\gamma^2 - 0.97857\gamma + 0.068225\,,\\
A_{16} &= -0.027338\gamma^2 + 0.12551\gamma - 11.218\,,
\end{aligned}$$

where t is the wall thickness, l the attachment footprint length and θ the weld angle, see Fig. B.2. The following validity limits are given for M_k

$$\begin{aligned}
0.005 \le &\alpha < 0.9\\
0.5 \le &\gamma \le 2.75\\
\frac{\pi}{6} \le &\theta \le \frac{\pi}{3}\\
\frac{\pi}{6} \le &\theta \le 0.42\pi \;\text{ if }\; 0.5 \le \gamma \le 1.25\,.
\end{aligned} \tag{B.5}$$

Surface point

The M_k factor at the points where the crack front intersects the components surface, for "as welded" conditions (weld toe radius $\rho \le 0.1\times$ plate thickness t) and membrane load, is given as

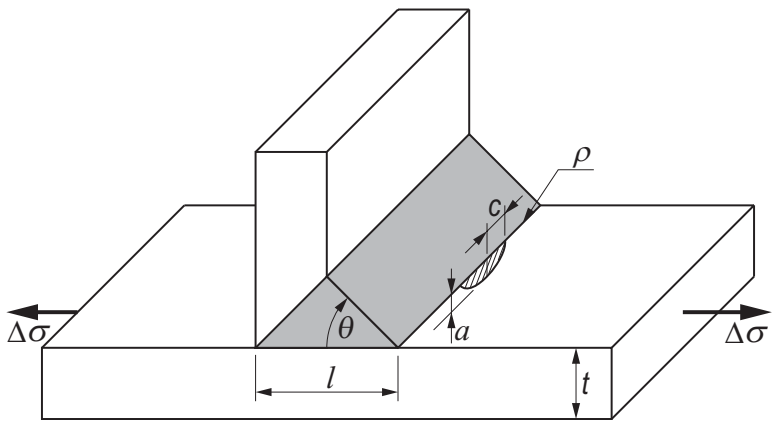

Figure B.2: Geometry of the joint analysed to derive the M_k factor equations [67].

$$M_\mathrm{k} = f_1\left(\alpha, 1/\beta, \gamma\right)\, f_2\left(\alpha, \beta, \theta\right)\, f_3\left(\alpha, \beta, \theta, \gamma\right)\,, \tag{B.6}$$

with

$$f_1 = A_1 \alpha^{\left(A_2(1/\beta)^2 + A_3(1/\beta) + A_4\right)} + A_5\left(1-\alpha\right)^{\left(A_6(1/\beta)^2 + A_7(1/\beta) + A_8\right)}\,,$$

$$f_2 = \left(A_9\beta^2 + A_{10}\beta + A_{11}\right)\alpha^{A_{12}} + A_{13}\left(1-\alpha\right)^{A_{14}}\,,$$

$$f_3 = \left(A_{15}\theta^2 + A_{16}\theta + A_{17}\right)\alpha^{A_{18}} + \left(A_{19}\theta^2 + A_{20}\theta + A_{21}\right)\mathrm{e}^{\alpha^{\left(A_{22}\theta^2 + A_{23}\theta + A_{24}\right)}}\,,$$

$$A_1 = 0.0078157\left(1/\beta\right)^2 - 0.070664\left(1/\beta\right) + 1.8508\,,$$

$$A_2 = -0.000054546\gamma^2 + 0.00013651\gamma - 0.00047844\,,$$

$$A_3 = 0.00049192\gamma^2 - 0.0013595\gamma + 0.011400\,,$$

$$A_4 = 0.0071654\gamma^2 - 0.033399\gamma - 0.25064\,,$$

$$A_5 = -0.018640\left(1/\beta\right)^2 + 0.24311\left(1/\beta\right) - 1.7644\,,$$

$$A_6 = -0.0016713\gamma^2 + 0.0090620\gamma - 0.016479\,,$$

$$A_7 = -0.0031615\gamma^2 - 0.010944\gamma + 0.13967\,,$$

$$A_8 = -0.045206\gamma^3 + 0.32380\gamma^2 - 0.68935\gamma + 1.4954\,,$$

$$A_9 = 0.15209\theta^2 + 0.0029155\theta - 0.38250\,,$$

$$A_{10} = -0.24523\theta^2 + 0.0013244\theta + 0.50434\,,$$

$$A_{11} = -0.64023\theta^2 + 2.2642\theta + 0.25959\,,$$

$$A_{12} = -0.25473\beta^2 + 0.40928\beta + 0.0021892\,,$$

$$A_{13} = -0.11458\theta^2 + 0.72927\theta - 0.22760\,,$$

$$A_{14} = 37.423\beta^2 - 15.741\beta + 64.903\,,$$

$$A_{15} = -0.14475\gamma^2 + 0.51648\gamma - 0.18189\,,$$
$$A_{16} = 0.34950\gamma^2 - 1.3069\gamma + 1.0641\,,$$
$$A_{17} = -0.10553\gamma^3 + 0.41373\gamma^2 - 0.38632\gamma - 1.9885\,,$$
$$A_{18} = 1.82250\theta^2 - 4.5008\theta + 3.1650\,,$$
$$A_{19} = 0.041574\gamma^2 - 0.16138\gamma + 0.14184\,,$$
$$A_{20} = -0.098912\gamma^2 + 0.39688\gamma - 0.58821\,,$$
$$A_{21} = 0.043891\gamma^3 - 0.19694\gamma^2 + 0.23516\gamma + 0.97585\,,$$
$$A_{22} = -0.046138\beta^2 - 0.12171\beta + 1.6277\,,$$
$$A_{23} = 0.088591\beta^2 + 0.27816\beta - 4.0124\,,$$
$$A_{24} = -0.052530\beta^2 - 0.13902\beta + 2.6646\,.$$

The validity limits are the same as for the deepest point.

B.4 Crack propagation with variable a/c ratio

In general, having a semi-elliptical surface crack, the stress intensity factor will vary along the crack front. This leads to a change in crack shape as the crack propagates. If Paris' law is valid in depth direction (a-direction) and along the surface (c-direction), the rates of crack propagation in both directions are related as

$$\frac{\mathrm{d}a}{\mathrm{d}c} = \frac{C\Delta K_{\mathrm{a}}^m}{C\Delta K_{\mathrm{c}}^m} = \left(\frac{F_{\mathrm{a}}}{F_{\mathrm{c}}}\right)^m\,, \tag{B.7}$$

where F_{a} and F_{c} are the geometry functions in a and c-direction, respectively. From the relation above follows that the crack extension increment Δc, corresponding to an increment Δa is found from

$$\Delta c = \left(\frac{F_{\mathrm{c}}}{F_{\mathrm{a}}}\right)^m \Delta a\,. \tag{B.8}$$

Hence, when a numerical integration is carried out, Δc is directly obtained from the given Δa.

Using the equations to calculate F, suggested by Newman and Raju [68], Eq. B.7 becomes:

$$\frac{\mathrm{d}a}{\mathrm{d}c} = \frac{1}{\left[\sqrt{a/c}\left(1.1 + 0.35\,(a/t)^2\right)\right]^m}\,. \tag{B.9}$$

As long as $a \ll t$, the crack asymptotically approaches a form where $a/c = \mathrm{d}a/\mathrm{d}c$. Assuming $m = 3$ the asymptotic a/c ratio according to Eq. B.9 is 0.89. However, as Newman and Raju [68] point out, experiments have shown that a semi-elliptical surface crack tends to become semi-circular in a thick plate subjected to membrane loading. They explain this discrepancy with different Paris constants, C, in the a and c-directions, due to the transition from plane strain in the material

to plane stress at the surface. Another reason for the deviation between experimental and predicted crack aspect ratio is that the crack does not obey a $1/\sqrt{r}$ singularity at the surface, see for example Pook [111], hence K loses its validity. However, especially in mode I loading this effect has a rather minor impact on fatigue life prediction [111]. To predict the correct aspect ratio, Newman and Raju [68] suggest using $C_\mathrm{c} = 0.9^m C_\mathrm{a}$, which leads to

$$\Delta c = \left(\frac{0.9 F_\mathrm{c}}{F_\mathrm{a}}\right)^m \Delta a\,. \tag{B.10}$$

Using $C_\mathrm{c} = 0.9^m C_\mathrm{a}$ predicts an asymptotic aspect ratio of approximately 1, if $a \ll t$, see Fig B.3a. If the crack approaches the opposite plate surface, a/c decreases, see Fig B.3b, since $F_\mathrm{a}/F_\mathrm{c}$ decreases.

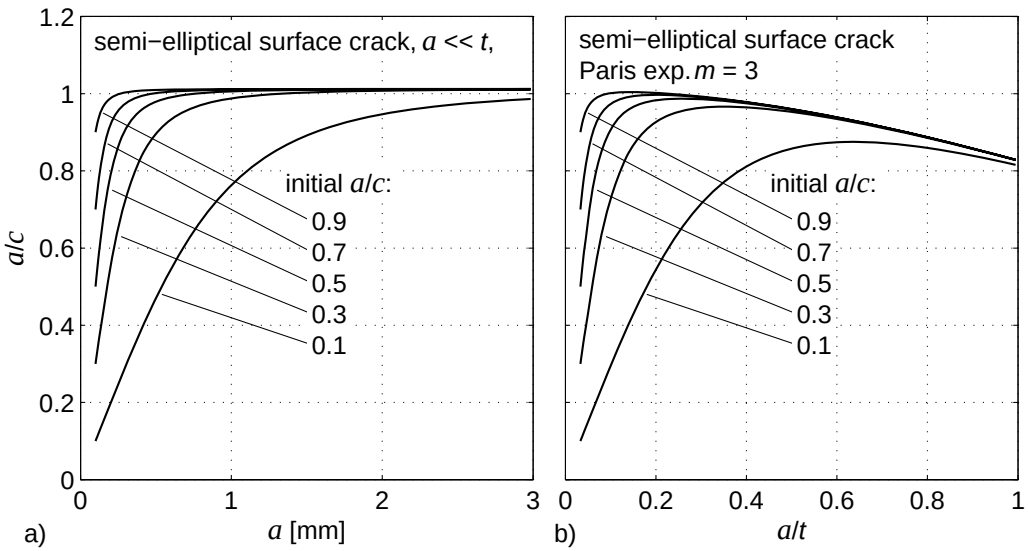

Figure B.3: Development of crack aspect ratio, a/c, as a semi-elliptical surface crack propagates: (a) a shallow crack and (b) a crack growing through the thickness. $C_\mathrm{c} = 0.9^m C_\mathrm{a}$ [68] was assumed in both cases.

APPENDIX C

Second moment of area of the cross section of the T-joint

To find the second moment of area relative to the x-axis

$$I_x = \int y^2 \mathrm{d}A \tag{C.1}$$

of the cross section of the T-joint, one quarter of the cross section area is divided into three parts A_1, A_2 and A_3, see Fig. C.1. Because of the symmetry in x and y the total second moment of area will be four times that of the quarter, which in turn will be the sum of the second moment of area of each part.

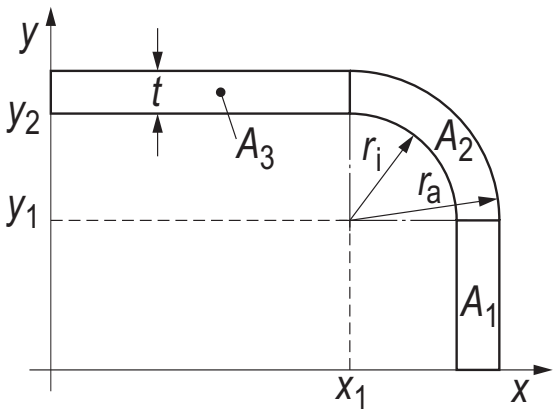

Figure C.1: One quarter of the cross section of the T-joint.

Using Steiner's theorem, the second moment of area corresponding to A_1, I_{x1} can be written as

$$I_{x1} = \frac{ty_1^3}{12} + \left(\frac{y_1}{2}\right)^2 y_1 t = \frac{ty_1^3}{3}\,. \tag{C.2}$$

To obtain I_{x2} integration is required:

$$\begin{aligned}
I_{x2} &= \int_{A_2} y^2 \mathrm{d}A = \int_r \int_\varphi (r\sin\varphi + y_1)^2 r \mathrm{d}\varphi\,\mathrm{d}r \\
&= \int_{r=r_\mathrm{i}}^{r=r_\mathrm{a}} \int_{\varphi=0}^{\varphi=\pi/2} (r^3\sin^2\varphi + 2r^2 y_1 \sin\varphi + r y_1^2)\mathrm{d}\varphi\,\mathrm{d}r \\
&= \int_{r=r_\mathrm{i}}^{r=r_\mathrm{a}} \left[r^3\left(\frac{\varphi}{2} - \frac{1}{4}\sin 2\varphi\right) - 2r^2 y_1 \cos\varphi + r y_1^2 \varphi \right]_0^{\pi/2} \mathrm{d}r \\
&= \int_{r=r_\mathrm{i}}^{r=r_\mathrm{a}} \left(\frac{\pi}{4} r^3 + 2y_1 r^2 + \frac{\pi y_1^2}{2} r \right) \mathrm{d}r \\
&= \left[\frac{\pi}{16} r^4 + \frac{2y_1}{3} r^3 + \frac{\pi y_1^2}{4} r^2 \right]_{r_\mathrm{i}}^{r_\mathrm{a}} \\
&= \frac{\pi}{16}\left(r_\mathrm{a}^4 - r_\mathrm{i}^4\right) + \frac{2y_1}{3}\left(r_\mathrm{a}^3 - r_\mathrm{i}^3\right) + \frac{\pi y_1^2}{4}\left(r_\mathrm{a}^2 - r_\mathrm{i}^2\right) .
\end{aligned} \tag{C.3}$$

The derived equation can be checked partly by setting $y_1 = 0$ and multiplying I_{x2} with four: $4I_{x2}(y_1 = 0) = \pi(r_\mathrm{a}^4 - r_\mathrm{i}^4)/4$, which corresponds to the second moment of area around a symmetry axis of a circular ring, as it should. Another control can be performed as follows. Mirroring A_2 at y_1 the second moment of area relative to $y = 0$ of the mirrored area becomes

$$I_{x2}^* = \frac{\pi}{16}\left(r_\mathrm{a}^4 - r_\mathrm{i}^4\right) - \frac{2y_1}{3}\left(r_\mathrm{a}^3 - r_\mathrm{i}^3\right) + \frac{\pi y_1^2}{4}\left(r_\mathrm{a}^2 - r_\mathrm{i}^2\right) . \tag{C.4}$$

I_{x2} and I_{x2}^* can be combined such that the second moment of area of a circular ring, $I_{x,\mathrm{cr}}$, with a distance y_1 to the bending axis is obtained:

$$\begin{aligned}
I_{x,\mathrm{cr}} &= 2I_{x2} + 2I_{x2}^* \\
&= \frac{\pi}{4}\left(r_\mathrm{a}^4 - r_\mathrm{i}^4\right) + y_1^2 \pi \left(r_\mathrm{a}^2 - r_\mathrm{i}^2\right) .
\end{aligned} \tag{C.5}$$

It is easily seen that the same result could be obtained by employing Steiner's theorem.

I_{x3} could be found using Steiner's theorem, however, integration gives the result in a more compact form:

$$I_{x3} = \int_{A_3} y^2 \mathrm{d}A = x_1 \int_{y_2}^{y_2+t} y^2 \mathrm{d}y = \frac{x_1}{3}\left((y_2+t)^3 - y_2^3\right) . \tag{C.6}$$

The second moment of area of the complete hollow section is calculated from:

$$I_x = 4(I_{x1} + I_{x2} + I_{x3}) . \tag{C.7}$$

APPENDIX D

Welding Procedure Specification for robotic welding of aluminum T-joints

Welding sequence

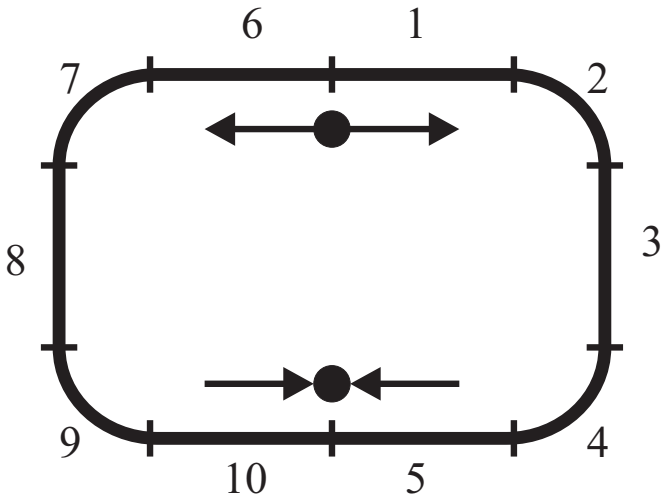

Welding parameters

Material: Aluminum RHS profiles (40 x 60 x 3), AA 6082-T6,
Robot: ABB IRB 2400 (S4C+)
Power source: ABB LRC 430
Filler wire: ER 5183, ø1.2 mm, Esab OK Autrod 18.16
Shielding gas: Ar 4.6, 25 l/min

Sequence	Wire speed [m/min]	Welding voltage [V]	Welding speed [mm/s]
1	8.0	25.0	9
2	8.0	23.0	-
3	8.0	22.0	10
4	7.0	21.5	-
5	8.0	22.0	12
6	8.0	23.0	9
7	8.0	23.0	-
8	8.0	23.0	9
9	8.0	23.0	-
10	8.0	22.0	12

Welding current

Wire speed:	8 m/min	7 m/min
Pulse current	288 A	276 A
Pulse time	1.9 ms	1.9 ms
Base current	68 A, 148 Hz	56 A, 128 Hz

Cleaning:
1. Degreasing with alcohol
2. Wire brushing